NMR Studies of Flowing and Segregating Granular Materials

by

Lori L. Sanfratello

B.A., State University of New York, Geneseo, 1995
M.S., Physics, University of New Mexico, 2003

DISSERTATION

Submitted in Partial Fulfillment of the
Requirements for the Degree of

Doctor of Philosophy
Physics

The University of New Mexico

Albuquerque, New Mexico

July, 2007

Acknowledgments

NMR Studies of Flowing and Segregating Granular Materials

by

Lori L. Sanfratello

ABSTRACT OF DISSERTATION

Submitted in Partial Fulfillment of the
Requirements for the Degree of

Doctor of Philosophy
Physics

The University of New Mexico

Albuquerque, New Mexico

July, 2007

NMR Studies of Flowing and Segregating Granular Materials

by

Lori L. Sanfratello

B.A., State University of New York, Geneseo, 1995
M.S., Physics, University of New Mexico, 2003

Ph.D., Physics, University of New Mexico, 2007

Abstract

The goal of this work is an improved understanding of 3D flows of both mono- and biparticulate granular systems. Magnetic resonance imaging (MRI) is used for these studies because of its unique ability to non-invasively measure both surface and subsurface flow behavior. The rotating cylinder geometry is employed for its simplicity, its wide applicability, and its distinctive axial banding segregation.

The velocity depth profile of monoparticulate systems is measured using MRI velocimetry. Deviations from the quadratic profile, derived from an energy dissipation minimization, were eliminated by reducing inertial effects. The results indicate that the quadratic profile is a fundamental characteristic of granular flow in the rotating drum.

Biparticulate granular systems segregate (unmix) under a variety of flow conditions and particle parameters. A 3D cellular automaton was developed to simulate

such a biparticulate system of two differently sized particles. It qualitatively mimics aspects of both radial and axial segregation, as well as the band coarsening observed experimentally in the rotating cylinder. Using MRI we experimentally demonstrate that the radially segregated core, of a system of two differently sized particles, has a flow pattern that is similar to the overall flow and that the bottom of the flowing layer is always well within the core region in the rolling regime. Furthermore, we demonstrate that the amount of small particles, the initial conditions and the length of the cylinder all play a role in the formation of axial banding segregation. Perhaps most importantly, we observe marked differences between the velocity depth profiles of monoparticulate systems, radially segregating systems, and axially segregating systems. The implications that these differences have for the formation, perpetuation, and band coarsening of the axial segregation phenomenon are discussed in reference to theories of axial segregation.

We conclude that subsurface flow behavior is vital to the understanding of both monoparticulate systems as well as to the axial segregation phenomenon, and that differences in velocity depth profiles along the axis of a 3D rotating drum may preferentially drive particle transport in biparticulate systems.

Contents

List of Figures

Glossary

$Fr = R\Omega^2/g$	Froude number, ratio of inertial to gravitational forces.
$Pe = r^2\dot{\gamma}/D_T$	Peclet number, A dimensionless group used to compare the effect of applied shear with the effect of thermal (Brownian) motion; Where r is the particle radius, $\dot{\gamma}$ is the shear rate, and D_T is the translational diffusion coefficient. For Pe << 1, particle behavior is dominated by diffusional relaxation, whereas for Pe >> 1, hydrodynamic effects dominate. Measures the importance of convection versus diffusion.

Chapter 1

Introduction

Granular materials are found in numerous and varied settings. Natural phenomena such as avalanches and landslides are made up of flowing granular matter. The rings of Saturn contain particles of ice and rock along with dust. Nearly 80 percent of everything manufactured or grown in the US exists in at least one stage of its development as a granular material [1]. Even traffic jams have been successfully modeled as a type of granular flow [2]. (See Fig. 1.1)

In spite of their ubiquitousness, a thorough understanding of granular materials, and granular flows in particular, remains elusive and many ways of dealing with their effects in daily life are *ad hoc*, i.e. each manufacturing plant having an empirical and not always optimal way of dealing with the unique challenges presented when trying to process and contain granular matter. Despite their apparent simplicity, granular materials are difficult to handle and transport, resulting in costly production delays, waste, and inefficiency. According to a National Research Council study, factories that process liquids achieve an efficiency rate of 80-90 percent, compared with only 40-60 percent for factories that process powders [3]. This is in part due to the fact that the problems arising when handling granular materials are still not well-

Figure 1.1: Examples of granular materials.

understood.

Of particular importance in processing is the manufacture of pharmaceuticals with appropriate amounts of active ingredients on a length scale the size of a pill. Highlighting the impact that poor mixing can have on this industry, a recent court decision (USA vs. Barr Labs) ruled that incomplete mixing and mixing characterization are adequate causes to halt production of pharmaceutical materials [4]. Complete mixing is challenging due to the fact that particles having only slightly different properties, such as size or density, tend to segregate (unmix) when they flow.

Even the storage of stationary granular assemblies is a non-trivial task. These configurations exhibit force chains, which cause nonlinear pressures on the sides of containers (Fig. 1.2).

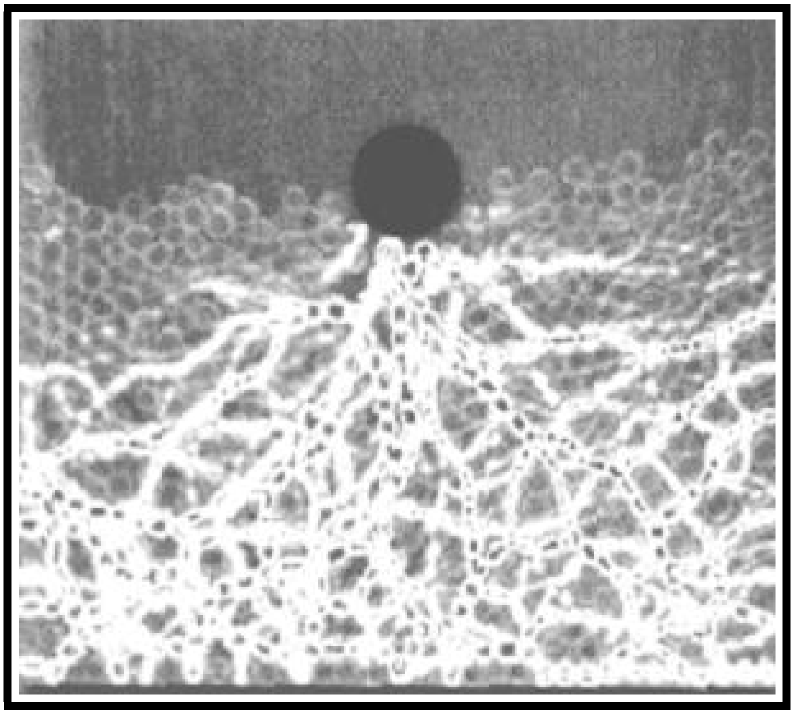

Figure 1.2: Nonlinear force distribution in 2D.

The collapse of poorly designed silos is one outcome of misunderstanding the way force is transmitted in something as seemingly simplistic as a stationary granular pile (Fig. 1.3). In addition, vibrations caused by, for example, the transportation of granular materials can have undesirable consequences such as the largest particles migrating to the top of a container (the so-called "Brazil nut effect" [5]) as well as the settling of material into a significantly smaller volume than when packaged.

The topic of this thesis is the steady flow of granular materials. Both mono- and biparticulate systems are considered. When investigating granular flows there is no accepted set of fundamental equations, such as the Navier-Stokes equations in fluid

Figure 1.3: Silo collapse.

dynamics. The phenomenology of these processes is fundamentally different from fluid flow, exhibiting a number of unique physical properties including energy dissipation, dilatancy, segregation, and nonlinear stress distributions. Mechanical properties of granular flows are only controlled by the momentum transfer during collisions and frictional contacts between grains [6]. Local forces on granular materials exhibit both strong nonuniformity and history dependence [4]. A consequence of the highly inelastic collisions between grains is that fluid-like behavior can only be observed when the system is continuously driven [1]. All these properties make a derivation of the underlying equations difficult. Furthermore, some of the assumptions made when describing a fluid may no longer be applicable (e.g., incompressibility). In addition, there is no convenient large separation of scales as between liquids and solids. Finally, in some instances, such as in the mixing and segregation (unmixing) of multiparticulate systems, it is not even clear that a continuum formulation is a proper description [7].

Engineers traditionally carried out research on granular materials. It has only been in the last 15 years that physicists began taking a renewed interest in the varied phenomena that result from the properties peculiar to granular matter. The original flurry of activity by physicists is accredited to the, now generally dismissed, idea of Self-Organized Criticality (SOC) in sandpiles reported by Bak, Tang, and Weisenfeld [8]. However, today physicists are active members in all aspects of the study of granular matter, recognizing granular materials and flow as a paradigm for driven dissipative systems far from equilibrium, as well as segregating systems as a simple example of pattern formation in dynamically driven systems [4].

There is, therefore, both a fundamental interest in and a practical need to understand granular flows. Experiments, theory and numerical simulations all attempt to accomplish this. Naturally these approaches are not independent, and each has its advantages when studying granular flows. Theorists are attempting to develop constitutive equations, sometimes beginning from a fluid mechanics and/or a statistical mechanics description [9–12]. Assumptions may be made to simplify the equations. Experiments can help this process by providing information on what is occurring within real systems, and therefore if or when particular assumptions are valid. However, experiments are often simplified versions of actual systems, scaled down in both size and complexity. Whether or not it is practical to conduct an experiment, numerical simulations can provide valuable insight. But many granular simulations are prohibitively calculation intensive. Furthermore, although exact in principle, simulations frequently rely on precise measurements and interaction models, which are not necessarily well understood [13]. Cellular automata simulations use simple phenomenological versions of actual systems [14, 15].

This thesis will focus on the experimental study using MRI, and briefly on a simple numerical simulation (a cellular automaton) of granular flows. The relationship that our results have to theories of granular flow and segregation, which will be presented in Chapter 5, will also be discussed. The system studied was a 3-dimensional horizontal rotating cylinder, generally half-filled with either mono- or biparticulate mixtures of spherical grains.

For granular materials to flow, it is first necessary that the material be at an angle, with respect to the direction of gravity, greater than a critical angle. This angle is termed the "angle of repose" and depends upon the material. Additionally, the material must dilate to some extent for flow to occur. Once the flow begins and becomes steady the angle at which it flows at will be slightly lower than the "angle of repose" and is termed the "dynamic angle of repose". Granular flows in horizontal rotating cylinders consist of two regions, a solid body region, which rotates along with the cylinder, and a lens-shaped flowing region whose surface flows at the dynamic angle of repose. These characteristics can be seen in Figure 1.4.

Six modes of solids motion are identified in the transverse plane of the rotating drum with increasing rotation speed. These are *slipping, slumping, rolling, cascading, cateracting,* and *centrifuging* [16]. All our experiments were carried out in the rolling/cascading regime, at Froude numbers ranging from $Fr = 3.75 \text{ x } 10^{-3}$ to $Fr = 2.99 \text{ x } 10^{-2}$ (5rpm to 40rpm).

Experiments were carried out using MRI to determine subsurface structure and dynamics. MRI velocimetry was used to determine the velocity field within the system when flow information was required [17, 18]. Traditionally, experiments of granular flows in rotating cylinders have been carried out in 2D drums. When longer

3D cylinders are of interest, the behavior of the grains has usually been viewed on the surface or through an endcap [19–22]. However, these observations are often insufficient to determine or interpret bulk behavior. Additionally, it has been shown that the flow profile at the endwall of a 3D cylinder is significantly different from both that away from the endwall and in 2D [23]. Nor can dynamical variables within the bulk be measured by surface studies. A probe may be inserted into the flow to determine such variables [24], but this is invasive and can disturb the behavior of the flow. Positron emission particle tracking (PEPT) has been used to determine subsurface information [25,26], but this method tracks a single particle and therefore bulk behavior is deduced from innumerable experiments with no assurance that every point in the 3D assembly has been sampled. MRI is therefore an invaluable tool, able to non-invasively determine the bulk behavior of surface and subsurface granular flows as well as being able to spatially resolve dynamic variables (e.g. velocity, diffusion) at any location within a 3D system.

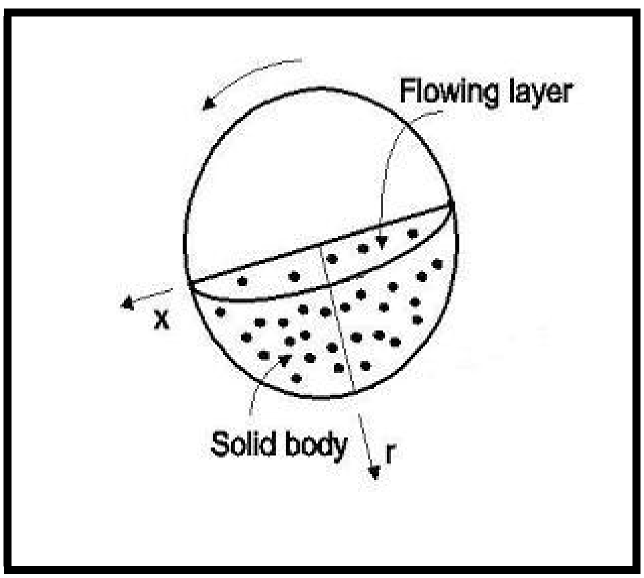

Figure 1.4: Granular flow in a rotating cylinder

Observing granular flow in the rotating drum a relationship is found between the velocity on the free surface of the flow, the depth of the flowing layer, the angle of repose, and the rotation rate of the cylinder. As the rotation rate is increased the particles at the free surface flow faster and the flowing layer becomes deeper [27]. The initially flat free-surface becomes "S-shaped" [28]. Furthermore, the velocity along the free surface which is symmetric about the center of the downhill flow at low rotation rates becomes skewed toward the bottom of the flow at higher rotation rates [19, 29]. We observed similar relationships between these variables using MRI at the axial center of a 3D cylinder. (Figs. 1.6, 1.5, and 1.7)

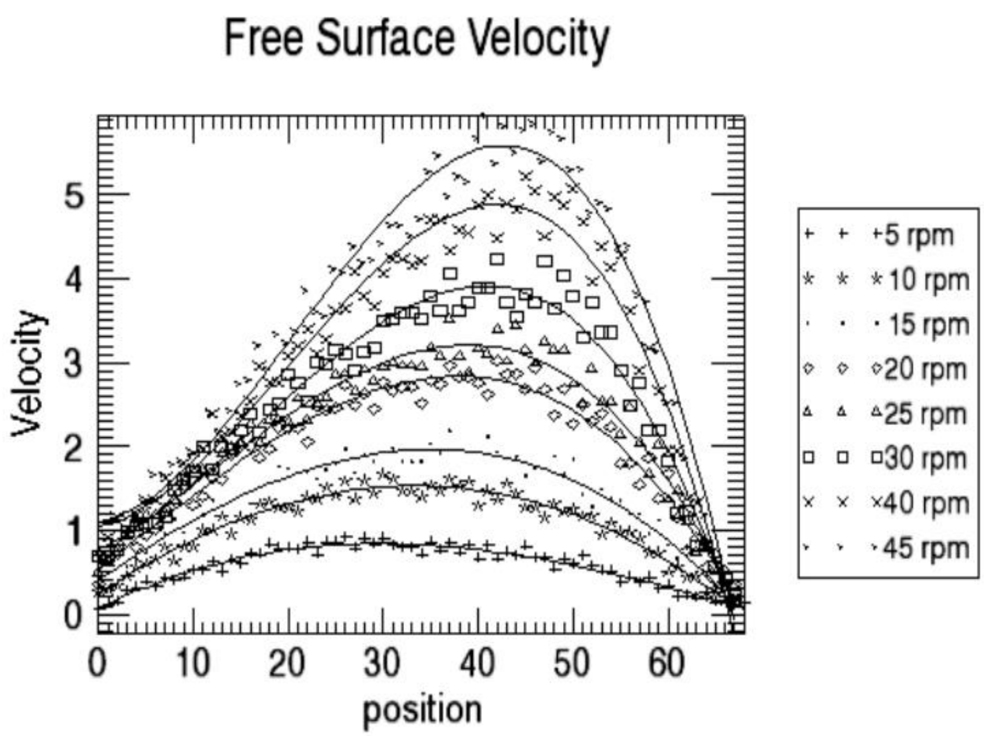

Figure 1.5: Velocity along the free surface increases with increased rotation rate and profile becomes less symmetric and skewed towards the bottom of the flow at higher rotation rates.

Furthermore, the depth of the flowing layer increases monotonically at an ever-decreasing rate with increase of rotation rate ([27] and our results presented in Fig. 1.7). It has been proposed that the asymptote is dependent on the ratio of particle

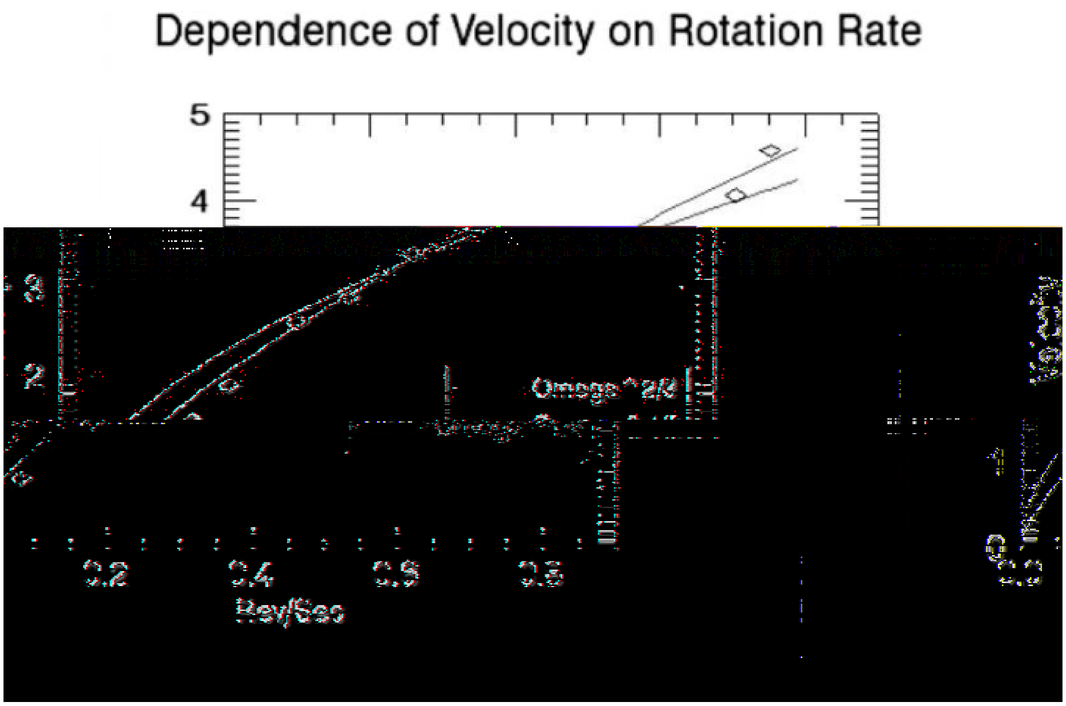

Figure 1.6: Velocity along the free surface increases with increasing rotation rate.

to drum diameter, and experimental evidence supports this [22, 30].

Some experimental data [31], using mustard seeds as the granular material, indicate a linear dependence of the dynamic angle of repose on the rotation speed which differs from the square-root dependence found by Rajchenbach [32], who used glass spheres. Yamane et al. [27] also found a linear relationship between the dynamic angle of repose and rotation rate. Klein and White [33] found the dynamic angle of repose to vary with the square-root of acceleration due to gravity, in reduced gravity experiments. Finally, and not surprisingly, it has been shown that the longer the surface layer, the faster and deeper the flow [34], which is necessary for mass conservation.

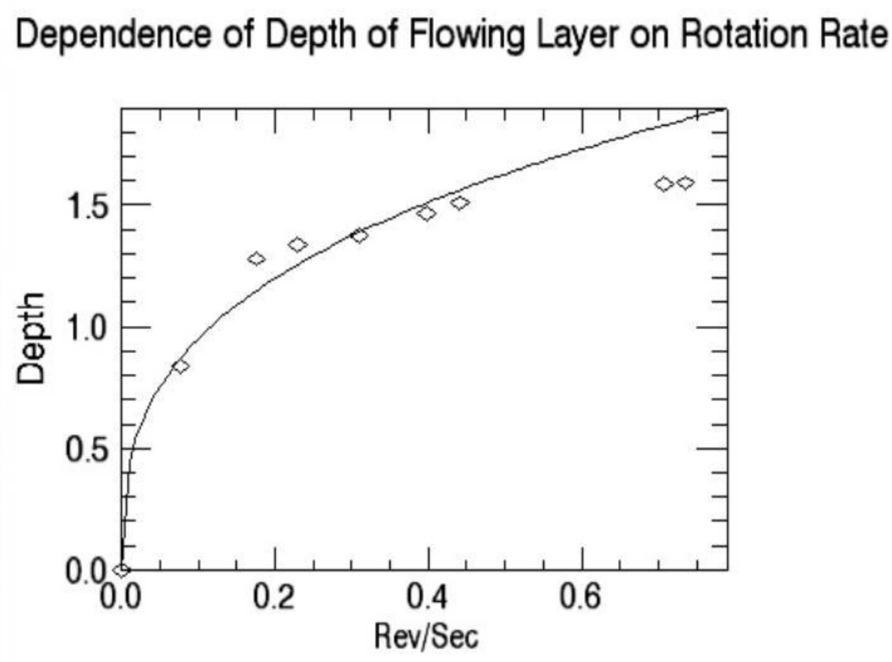

Figure 1.7: Depth of the flowing layer increases monotonically at an ever-decreasing rate with increased rotation rate. Depth is measured in cm.

Another characteristic of importance for understanding granular flow in the horizontal drum geometry, is the form of the velocity depth profile along the central perpendicular bisector to the free surface (i.e. at the midpoint of the downhill flow). This feature of granular flow has been investigated experimentally both in 2D and at the endwall, [19–22] but rarely at the axial center [27, 35], of a long cylinder. Often the velocity depth profile along the perpendicular bisector in the flowing layer has been fit by a line, and this linear fit has been incorporated into some theories of granular flow [36]. Yet, using MRI to study flow at the center of a long cylinder, Nakagawa and coworkers [35] observed that the velocity depth profile (of the dominant component of velocity), along the perpendicular bisector in the shear flow layer of a half-filled cylinder, may be fit by a second order polynomial. The dominant component of velocity is defined as being in the direction of flow (Fig. 1.8). These authors also noted that the quadratic form is consistent with an energy dissipation minimization criterion, assuming uniform particle density in the flowing region.

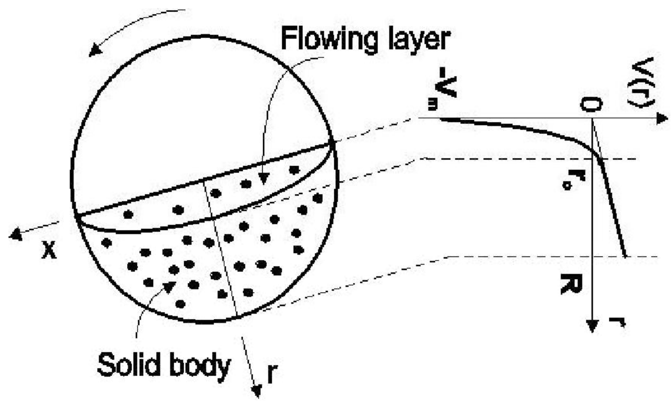

Figure 1.8: Where velocity depth profile is measured. V(r) is the velocity in the direction of flow, r is the radial coordinate, V_m in the free surface velocity, r_0 is the depth of the flowing layer, and R is the radius of the cylinder.

Nakagawa, et al. [35] additionally found that the quadratic fit, which is good at low rotation rates, develops a deviation near the free surface at higher rotation rates, with the velocity close to the free surface falling below the quadratic function. It was theorized that this deviation is due, at least in part, to inertial effects. A striking example of this can be seen in the early MRI tagging experiments reproduced here as Figure 1.9 [35]. Initially, noninvasive parallel tags are placed on the particles of a transverse slice in the axial center of a 3D cylinder. The tags remain straight and rotate with the cylinder except where the particles move with respect to the cylinder and bend the tags. Figure 1.9 shows the tags after a delay of 46 ms, for a fast rotation rate of 9.9 rad/s (95 rpm). The bent tags show that the particles on the free surface have slowed so much that the fastest flowing particles are now well below the free surface.

To test the idea that the deviation from the quadratic seen at moderate to high

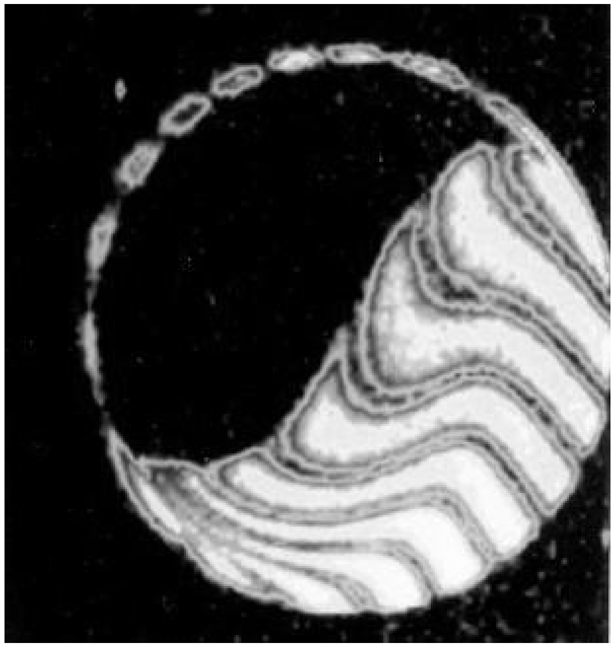

Figure 1.9: Early MRI tagging experiments

rotation rates is due to the unweighting of the particles as they emerge from the solid body layer onto the free surface [35], we placed a paddle along the upper third of the free surface flow at approximately the dynamic angle of repose. This prevented the particles from leaving the surface as they emerged from the solid body layer, thereby reducing inertial effects. Our results, presented in Chapter 3, show that the quadratic fit is better with the paddle than without when the comparison is made at the same solid body rotation rate, at the same free surface velocity, or with the paddle placed at different positions, so long as it makes good contact with the surface. This result strongly suggests that a quadratic velocity depth profile may be a fundamental property of granular shear flows in the horizontal rotating cylinder. Such a profile additionally implies that the velocity distribution of granular flow in this geometry is determined by minimizing collisional losses.

Although the understanding of monoparticulate granular flow is important, some of the greatest practical challenges as well as some of the most intense interest in flowing grains is caused by the behavior of multi-particulate systems. When particles varying in size are combined they have the tendency to segregate (unmix) under a wide variety of flow conditions. In long rotating cylinders the segregation is of two types. First, a quickly developing radial segregation occurs with the smaller particles forming a core along the axis of the cylinder within a few rotations (Fig. 1.10).

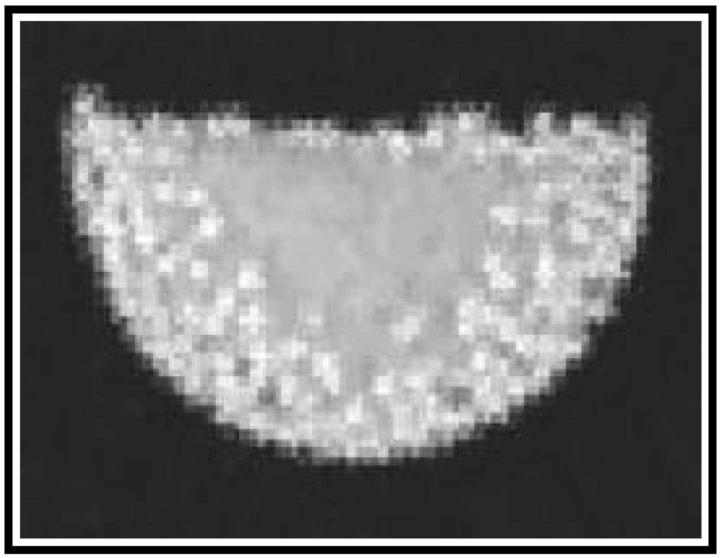

Figure 1.10: Typical radial segregation pattern (static MRI image). Smaller particles have moved into the core of the cylinder, Larger particles form a ring around this core.

Next, sometime after the core forms, axial bands of the different sized particles may develop along the length of the cylinder (Fig. 1.11). Oyama first reported this axial segregation (or banding) phenomenon in 1939 [37].

If the axially segregated system is allowed to evolve further a slow coarsening of the banded structure may also be seen, with the axial bands becoming fewer and thicker. The formation of the radial core has the generally well-accepted explanation of resulting from a dynamic sieving process [38], with the smaller particles finding their way between the spaces left around the larger particles within the flowing layer.

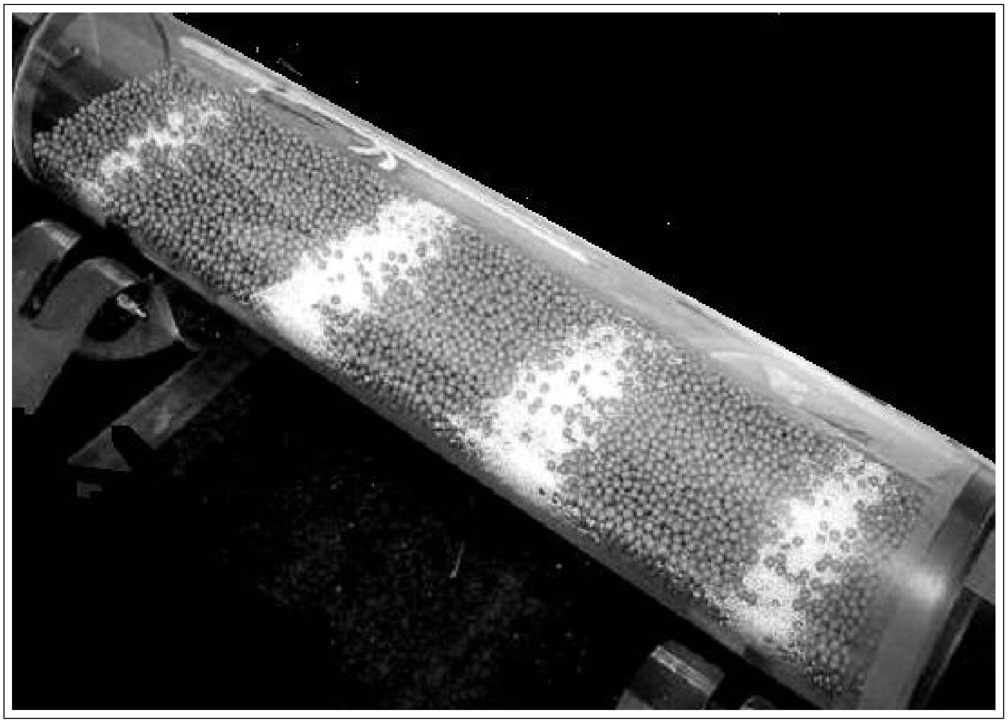

Figure 1.11: Typical axial segregation pattern (static surface picture). Bands of small or large particles form along the axis of the cylinder.

However, due to the fact that radial segregation appears to be an important antecedent for axial segregation, understanding core dynamics and not solely why it forms, may give insight into the necessary precursors for axial banding segregation. Therefore, we investigated the bulk behavior of the radially segregated core in a system which is known and observed to radially segregate and found that the core behaves in a manner similar to that of the overall flow with its own surface (approximately parallel to the free surface), flowing layer depth (the bottom of the flowing layer was always located within the core), and bottom. Furthermore, important differences were observed when a comparison of the velocity depth profiles of segregated and pure particle systems was made. Our experimental results on radial segregation will be presented in Chapter 6.

There is still debate over the cause(s) of axial banding segregation and later band coarsening of biparticulate granular systems in the rotating drum. Many theories cite only surface effects [12, 15, 39] but these cannot account for the experimental observation that the radial core may develop undulations that never reach the surface of the system [40]. Nor do they explain the recent experimental results of Pohlman et al. [41], which show that even large differences in the dynamic angle of repose between the constituents of a biparticulate system, the most often proposed surface mechanism for driving axial segregation, is insufficient to induce segregation. A traveling wave state has also been observed in certain mixtures, which is qualitatively different from the larger, slowly coarsening bands previously observed [42]. These authors point out that most models where surface effects are proposed as the segregating mechanism are first order in time, yet the behavior of the transient traveling wave state makes it "seem unlikely that they are the result of nonlinearity in a one-dimensional PDE model which is merely first order in time" [42]. Aranson and Tsimring [12, 43] have proposed an order-parameter style model which can account for this transient, but later experiments [44] have shown that the coupled fields do not have the correct phase relationship.

Experimentally, it has been found that the ratio of small to large particles within an axial slice, for a biparticulate system that segregates, influences qualitative features of the velocity depth profile along the perpendicular bisector to the free surface of the flow [23]. These differences were not seen for a biparticulate system that does not axially segregate. These results indicate that a sub-surface mechanism is likely to be involved in the phenomenon of axial segregation. Having identified a subsurface feature (the velocity field) that is different between segregating and non-segregating systems, it is important to gain an understanding of how this difference could drive axial transport. The changes seen when different ratios of particles are present indicates that a gradient in the velocity depth profile along the axis could be a source of axial transport influencing segregation.

We took full 3D velocity images of segregated biparticulate systems. In the case of biparticulate systems which radially but not axially segregate the profiles followed that of a pure small particle system until the top of the core. However, important deviations are seen between the pure small particle profile and the areas where small particles are present in steady state axially segregating systems, contrary to our naive expectation. We additionally found variations along the axis due not just to differences in the particle ratio within a particular slice, but also dependent upon the total system composition. Our experimental results will be discussed further and in reference to recent theories of axial segregation in Chapter 7.

Once formed, axial bands must somehow act to prevent being dispersed by the random motions of the grains. Most continuum models of banding segregation have assumed that these random motions are analogous to normal diffusion. Recent experimental evidence is divided as to whether or not this is the case. Experiments by Khan and Morris [45] in 2005 indicate that the axial transport of the radially segregated core along the drum is not well described by normal diffusion. They found that both the motion of the radially segregated core as well as the self-diffusion of monoparticulate systems along the drum is subdiffusive. The technique used in these experiments was somewhat insensitive and they looked only at pre-segregated initial conditions. Taberlet et al [46] have found normal diffusion using a DEM simulation technique and looking at the rate of diffusion by both collapsing the results and also by studying the time evolution of the mean squared deviation, from which they claim that their results are more robust than those of [45]. How quickly bands form and coarsen will depend on this rate of diffusion.

1D MRI projection imaging allowed us to rapidly acquire additional information. We investigated three different initial conditions for three different sets of small to large particle ratios, 1:2, 1:1, and 2:1. The initial conditions used were a mixed system, a small particle axially centered band and a small particle band to one side of the cylinder. There were, therefore nine different experimental runs. An example of a mixed initial condition system and its evolution over 30 min, with 1D MRI projection images taken at a frequency of 1 Hz, can be seen in Fig. 1.12. We found the initial conditions as well as the amount of small particles in the mixture to have an affect on the final banded state. Results will be elaborated in Chapter 7.

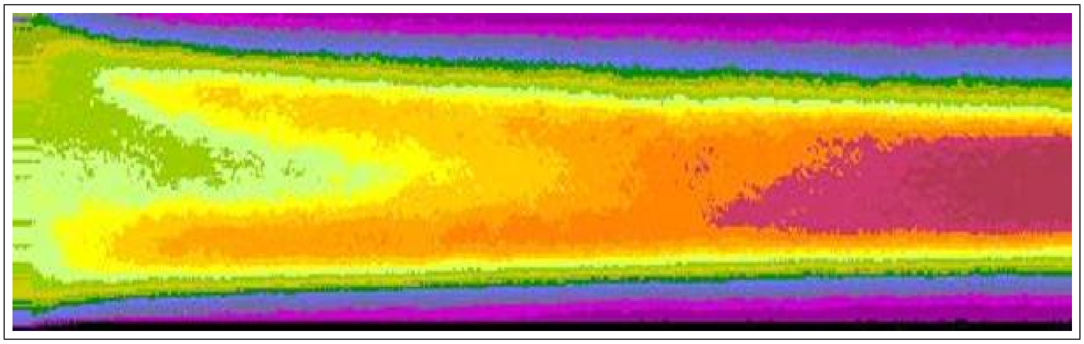

Figure 1.12: Example of 1D MRI projection images of the time evolution of a biparticulate system over 30 min with a mixed initial condition. Time runs along the horizontal axis and axial location along the vertical axis. Initially two subsurface bands form and then merge to become one band at the surface.

When information that is difficult or impossible to obtain experimentally is needed, numerical simulations can be valuable tools. Cellular automata (CA) simulations, such as the one presented in Chapter 4 of this thesis, are a simple phenomenological way to test how varying combinations of particle properties may influence the segregation pattern of large systems of particles over both short and long time scales. The study of such large systems for long times can make other types of simulations, such as the more commonly used particle dynamic (PD) simulations, prohibitively calculation intensive. Furthermore, although PD simulations are exact in principle they rely on precise measurements and interaction models, which are not necessarily well understood [13]. It is also possible that CA simulations, which take into account only surface effects, may yield insight into where purely surface effect theories work and where they fail to accurately describe experimental observations.

We developed a 3D cellular automaton to simulate the time evolution of biparticulate granular material in a horizontal rotating drum. The evolution of the system was based on that of a simulation developed by Yanagita [14], which simulated particles of the same size but different frictional properties. The system we modeled was composed of two different sized particles. By varying the frictional properties of the biparticulate system aspects of both the segregation and mixing behaviors observed experimentally could be reproduced. Further, if the larger particles had a much greater friction coefficient than the smaller particles a reversal of the sense of radial segregation occurred. Coarsening of the banded structure was also observed. To our knowledge this is the first time that a CA model has been used to simulate 3D biparticulate granular systems in a rotating drum geometry whose constituent particles differ in both size and frictional properties.

We believe that this combination of investigations has given valuable insight into the directions that extensions of current theories and new theoretical formulations of granular flow and segregation should take.

Chapter 2

MRI to Study Granular Flow

2.1 MRI Overview

Magnetic resonance imaging (MRI) works because we are able to detect the way that nuclei with a magnetic moment respond to externally applied magnetic fields. "The MRI experiment is really a combination of a two-step process where, in the first stage, the proton spin orientation is manipulated by an assortment of applied magnetic fields. In the second stage, changes in orientation can be measured through the interaction of the protons magnetic field with a coil detector." [47] This allows for the noninvasive subsurface imaging of opaque materials such as tissue in the human body or granular materials. Additionally, MRI has an extensive list of characteristics that may be used to generate image contrast. By variation of these scanning parameters contrast can be altered and enhanced in ways to detect different properties within a sample.

All nuclei that contain an odd number of protons can have an intrinsic magnetic moment and angular momentum. Therefore, when a static magnetic field B_0 is turned on, or such a sample is placed into a static magnetic field, individual nuclear spins within the sample will try to align with the field. Since we will here confine the discussion to the simplest case, that of spin 1/2 nuclei, an individual spin will only have two options, either to align or antialign with the B_0 field, due to quantization of the energy levels. At room temperature, moderate field strength ($\sim$ 1.5 Tesla), and hydrogen-1 nuclei the excess of spins aligned with the magnetic field is a small effect, with only about 1 out of a million more spins aligning with rather then against the field. This is a result of thermal energy greatly exceeding the energy difference between parallel and anti-parallel energy states at room temperatures. However, when looking at a sample that is rich in protons (often hydrogen-1 in the case of MRI applications, due to its being the most receptive isotope at natural abundance) there are on the order Avogadro's number spins affected by the applied field, so the resulting polarization is $\sim 10^{17}$ spins. This large number of nuclei is the main reason a signal can be obtained from a sample.

A macroscopic quantity can be defined which relates the number of spins that try to align with a static magnetic field. This quantity can be derived from linearizing the Boltzman statistics relating the number of spins aligned with the magnetic field to those aligned against it,

$$N_{aligned}/N_{antialigned} = e^{-E/kT} = e^{-\hbar\gamma B_0/kT}. \tag{2.1}$$

The net magnetization is then the difference between the number of spins aligned and anti-aligned with the field,

$$\text{Net Magnetization} \equiv M_0 = N_{aligned} - N_{antialigned}. \tag{2.2}$$

Where E is the transition energy,

$$E = \hbar\gamma B_0 = \hbar\omega_0; \tag{2.3}$$

And

$$\omega_0 = \gamma B_0 \qquad \textit{Larmor precession frequency.} \tag{2.4}$$

The Larmor precession frequency, due to the static magnetic field B_0, is equal to the frequency of a photon which would cause a transition between the two energy levels of the spin 1/2 nuclei. $\hbar$ is Planck's constant, γ is the gyromagnetic ratio, k is Boltzman's constant, and T is the temperature. Since the net magnetization M_0 is a *macroscopic* quantity, it allows us to use a classical picture for a description of the simple types of MRI experiments discussed here (Fig. 2.1).

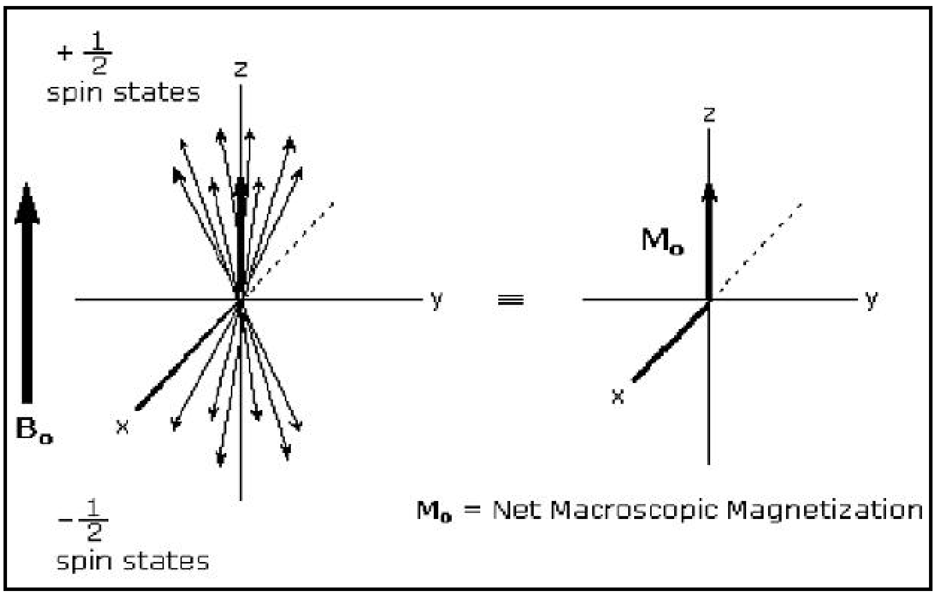

Figure 2.1: Net magnetization

To cause M_0 to precess in the static magnetic field B_0, a radio frequency (rf) pulse, at frequency ω_0 is applied to tip the net magnetization preferably into the x-y plane (Fig. 2.2a), perpendicular to the B_0 field. Note that Fig. 2.2 shows the magnetization vector in a coordinate frame colinear to the z-axis and rotating at the

Larmor precession frequency, the x'-y' frame. This is a 90-degree ($\pi/2$) pulse, although the angle, Θ by which the magnetization is tipped may be varied by changing either the strength B_1, or the duration τ, of the pulsed rf field, with the relationship,

$$\Theta = \gamma B_1 \tau. \tag{2.5}$$

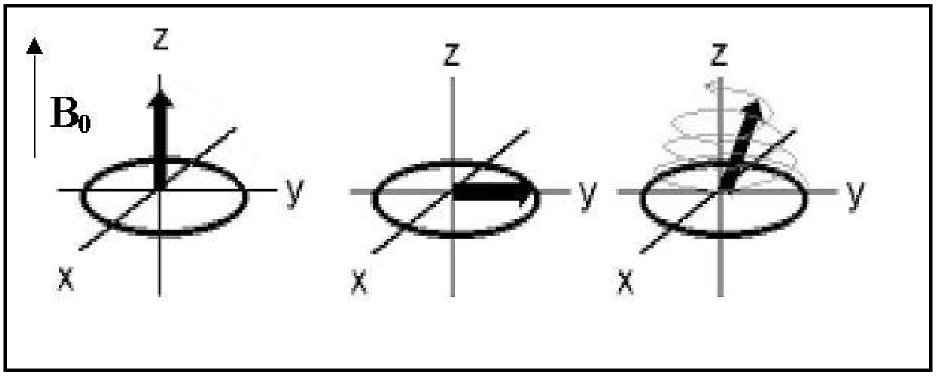

Figure 2.3: Longitudinal magnetization, longitudinal magnetization tipped by rf pulse into transverse plane, and recovery.

(Fig. 2.3c), so long as $T2 \sim T1$. Else, when $T2 \ll T1$, the dephasing occurs so quickly that the longitudinal magnetization is gone before the T1 recovery begins, and there is therefore no precession as the longitudinal magnetization recovers. For most liquids $T1 \sim T2$ is a good approximation. The characteristic time it takes for an individual nucleus to recover to its equilibrium state is termed the spin-lattice relaxation time, T1, and the longitudinal magnetization is given by:

$$M_z(t) = M_0(1 - e^{-t/T1}) \tag{2.7}$$

where $t = 0$ is the time at the center of the $\pi/2$ rf pulse and at which the longitudinal magnetization is $M_z = 0$. Differences in T1 between substances may therefore be used to see contrast in an image, since different T1's imply different recovery times for the longitudinal magnetization. When an image is taken, areas with different recovery times have different intensities dependent on how long after the rf pulse the image is acquired. These types of images are, appropriately, named T1-weighted images. T1 is the spin-lattice relaxation time and is due to the coupling of spins with the "lattice". In this context, "lattice" means available degrees of freedom that can take up the energy that the spins release when they relax. In solids it could be phonon modes, hindered molecular rotation, etc., while in fluids it could be due to rotational or translational motion.

The spin-spin decay factor, T2, is caused by the decorrelation between spins once they are tipped into the transverse plane. Their phases disperse due to variations in the local magnetic field experienced by each spin. This is caused by the interactions between neighboring spins and is an intrinsic property of the sample. The magnetization in the transverse plane is then given by,

$$M_{xy}(t) = M_{xy0}e^{-t/T2}. \tag{2.8}$$

T2 is always less than or equal to T1. T2 weighting offers an alternative contrast mechanism in an image.

In addition to these T2 effects, inhomogeneities in the static magnetic field generated by the magnet cause the spins in the transverse plane to dephase with a characteristic time $T2_{inhomo}$. This dephasing, however, is refocusable using an additional rf pulse, as will be described later. In addition, the density of spins will have an effect on the signal, i.e., where there are more spins there will be a larger signal. Furthermore, a larger field strength will cause more spins to align with it. There is, therefore, an increase in signal to noise (SNR) for larger field strengths. In addition, $\frac{\partial B}{\partial t}$ seen by the readout coil is larger at higher magnetic fields because the spin precession frequency scales with field strength. However, magnetic susceptibility issues can become problematic at very high field strengths, in particular at interfaces between different susceptibilities. The characteristics of different relaxation times and spin densities are taken advantage of when imaging for medical applications. No matter the application, these variables allow images to be weighted to show particular characteristics depending on the desired information.

2.2 Frequency Encoding and Readout

One simple way to accomplish magnetic resonance imaging (MRI) in 1D is by applying a linear magnetic field gradient, called the frequency encode gradient, ($G_x \equiv \frac{\partial B}{\partial x}$), where x is along any direction of interest in the sample. This will cause different areas of the sample to precess at different rates depending linearly on their location within the sample according to the Larmor precession relation,

$$\omega(x) = \gamma B(x) = \gamma(xG_x + B_0), \tag{2.9}$$

where x is the spatial coordinate and G_x is the gradient strength at that location. Thus, this procedure produces a signal with spatially varying frequency components. A receiver coil can then read out this signal and, owing to the fact that the Fourier transform of the readout signal is the "spectrum" in the frequency domain, and the direct correspondence between frequency and spatial location, an image can be formed. The magnetization at readout is,

$$M(t) = \int M_o(\mathbf{x}) e^{-i\gamma \mathbf{x} \int_0^t \mathbf{G}(t')dt'} d\mathbf{x} \equiv \int M_o(\mathbf{x}) e^{-i\mathbf{x}\mathbf{k}(t)} d\mathbf{x} \tag{2.10}$$

where,

$$\mathbf{k}(t) = -\gamma \int_0^t \mathbf{G}(t')dt' \tag{2.11}$$

is the wave vector introduced as the Fourier conjugate variable to the space coordinate, $\mathbf{x}$ [48]. For frequency encoding the wave vector, $\mathbf{k}(t) = -\gamma \mathbf{G} \int dt'$, since the gradient is not time-dependent, and therefore the wave vector $\mathbf{k}$ scales with the acquisition time. The Fourier transform of Eq. 2.10 is the 1D image in frequency space which is directly related to position by the Larmor precession frequency, $\omega(x) = \gamma x G_x + B_0$. Therefore, with the application of a *single* frequency encode gradient at readout a one-dimensional line of data can be acquired.

2.3 Phase Encoding

It is also possible to phase encode the spins, as well as frequency encode. This allows for the flexibility of efficiently acquiring a 2- or 3D image. Furthermore, phase encoding is less susceptible to temporal changes during signal acquisition than frequency encoding. Phase encoding is accomplished in much the same way as frequency encoding, except that instead of reading out the signal while a gradient is applied, the phase encode gradient is applied first and then turned off sometime before readout. Since the application of the phase encode gradient causes the spins to precess at different position-dependent frequencies, they will have different phase angles depending on their position during the time that the phase-encode gradient was applied. Once the phase encode gradient is turned off all the spins will again precess at the same *frequency*, but now have different *phase angles* depending on their location. Each time a new data point is acquired the magnitude of the phase encode gradient is changed. It is changed in equal increments between the maximum amplitude of the phase encode gradient, through zero, to the minimum amplitude (where maximum amplitude = -minimum amplitude). This causes the spins in the phase encode direction to acquire a frequency dependence according to the location of the spins during the applied gradients (Fig. 2.4). The spins in the phase encode direction therefore acquire a frequency which depends on position and the gradient amplitude step size. A Fourier transform may again be used to take data from the time domain (k-space) to the frequency domain and then relate it to the spatial domain. See Fig. 2.4 for the relationship between the applied gradient, the phase angle, and the resulting wave vector. The signal is, again,

$$M(t) = \int M_o(x) e^{-i\mathbf{x}\mathbf{k}(t)} d\mathbf{x} \tag{2.12}$$

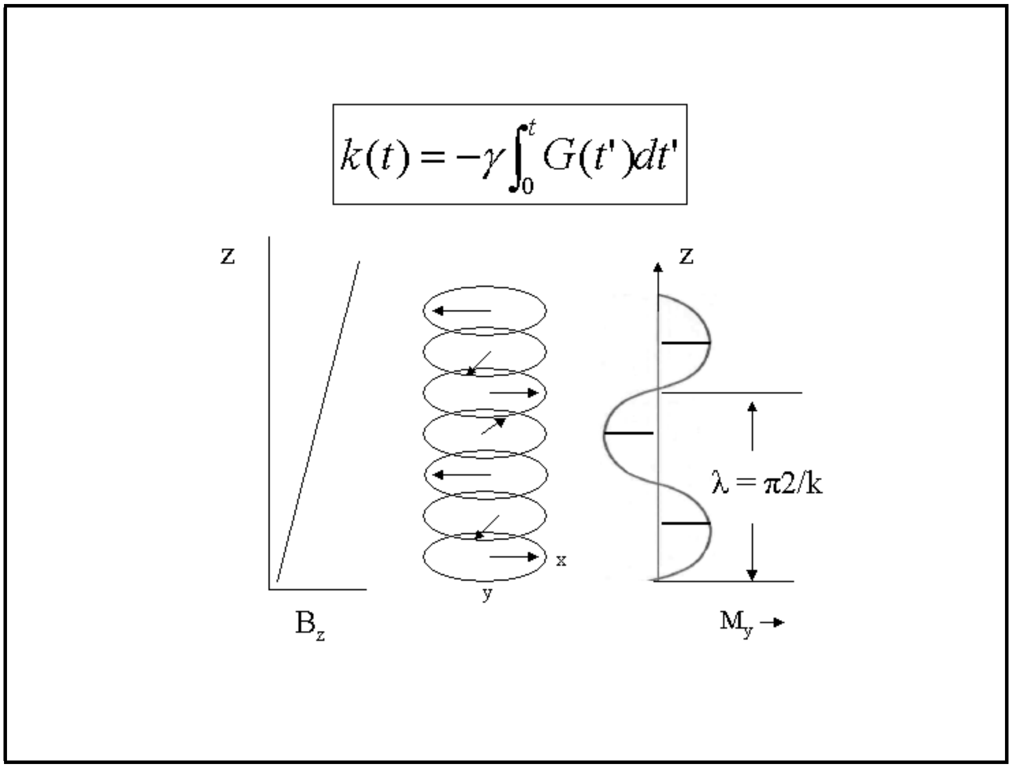

Figure 2.4: Relationship between k-space, applied gradient, and duration of gradient pulse for phase encoding.

with,

$$\mathbf{k}(t) = -\gamma \int_0^t \mathbf{G}(t')dt'. \tag{2.13}$$

Phase encoding can be used to acquire information in a direction perpendicular to the frequency encode direction, and must be stepped though to form a 2D image. Spins may be localized in one direction by the frequency at which they are precessing and in the other direction by changes in phase angle due to different gradient strengths.

2.4 Slice Selection

Slice selection in MRI is the selection of spins in a plane through an object. Slice selection is achieved by applying a linear magnetic field gradient during the period that the rf pulse is applied. A $\pi/2$ rf pulse contains a band of frequencies, on the order of the inverse of the pulse duration, and this would be reflected in the slice profile. A rf pulse envelope shape of $sinc(\omega t)$ ($\equiv \frac{sin(\omega t)}{\omega t}$) is usually used so that the slice profile is rectangular. Such a $\pi/2$ pulse applied *in conjunction* with a magnetic field gradient will only rotate spins which are located in a slice or plane through the object that is perpendicular to the gradient.

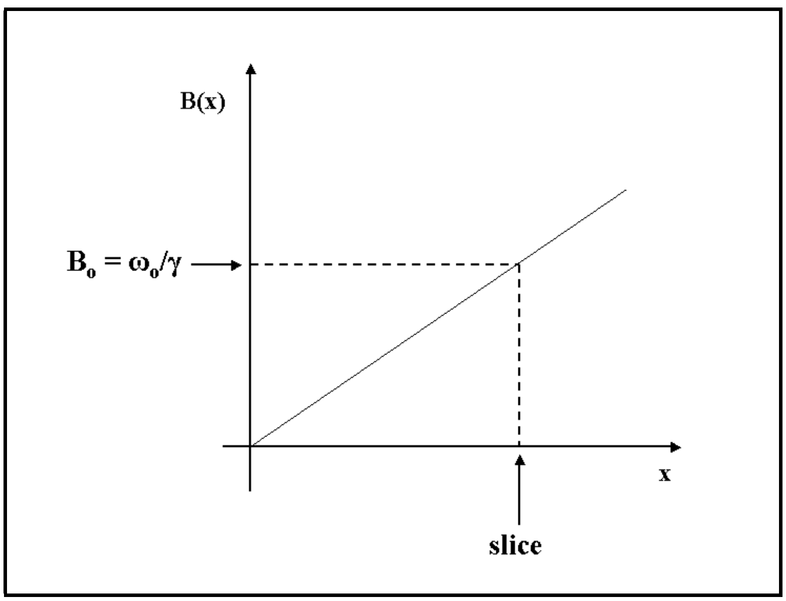

Figure 2.5: Slice selection.

By applying the additional slice select gradient the spins in the 2D slice of the object with the same Larmor precession frequency are selected, with these spins being the ones manipulated throughout the rest of the pulse sequence (Fig. 2.5). The location of the plane along the x-axis with respect to the isocenter is given by,

$$x = \Delta\omega/\gamma G_s, \tag{2.14}$$

where $\Delta\omega$ is the frequency offset from ω_0 (i.e. $\omega - \omega_0$), G_s the magnitude of the slice select gradient. The width of the slice can be controlled by changing either the frequency width of the rf excitation pulse or the value of the gradient. A 2D image can thus be obtained using a slice select gradient in one direction, frequency encoding in a second direction and phase encoding in the third direction.

2.5 The Spin-Echo Pulse Sequence

One way in which an MRI signal can be formed and acquired is by using a spin-echo pulse sequence (Fig. 2.6). A $\pi/2$ rf pulse is turned on in the presence of a slice selective gradient. Therefore a plane within the object has now been ”selected” to have transverse magnetization. Next, a phase encode gradient is turned on in the phase encode direction, one of the two directions in the selected plane. This will cause spins in the gradient direction to process at different frequencies. The phase encode gradient is then turned off and the spins all precess at the same frequency again, but now have different phase angles due to their position during the time of the phase encode gradient pulse. At the same time that the phase encode gradient is turned on a ”dephasing gradient” is applied in the frequency encode direction, so that when the π rf pulse (discussed next) causes an echo to form the maximum signal occurs at the center of the read-out gradient, at a time termed TE, the echo time (see Fig. 2.6). (It is not a necessary condition that the ”dephasing gradient” and the phase encode gradient are temporally concurrent, this is just a particular of the pulse sequence presented here.) Next, at TE/2, the π rf pulse is applied to refocus the spins. This pulse also refocuses unwanted changes in the spins due to inhomogeneities in the static magnetic field, thus minimizing the dephasing of spins in the transverse plane, and ideally eliminating the effect of $T2_{inhomo}$. This works because any unwanted dephasing during the first TE/2 time will be equal and opposite to that which occurs during the time from TE/2 to TE due to the π rf pulse application, so long as the spins are stationary. Finally, a readout gradient in the frequency-encode direction is applied as the signal is digitized at a sampling frequency f_s. The distance across the image is known as the field of view (FOV), and is determined by:

$$FOV = 2\pi f_s/\gamma G, \tag{2.15}$$

where f_s is the sampling frequency at readout and G is the gradient. The signal intensity is,

Spin-Echo Sequence :

$$S = k\rho(1 - exp^{(-TR/T1)})exp^{-TE/T2}, \tag{2.16}$$

where k is Boltzmans constant, ρ is the density of spins and TR is the repeat time of the sequence. Thus, an MRI image contains both the amplitude and phase of the signal.

The spin-echo pulse sequence is repeated for as many phase-encode steps as are necessary, each step taking an amount of time TR (the repeat time). Once the signal is read-out by a receiver coil it is Fourier transformed first in the frequency encode direction and then in the phase encode direction. The MRI image is the Fourier transformed signal localized spatially by the Larmor precession relation.

The 1-, 2-, and 3D image data contained in this thesis were acquired by a combination of methods described here. For our studies the characteristic times T1 and T2 are not utilized for contrast since all of our beads contain the same NMR sensitive

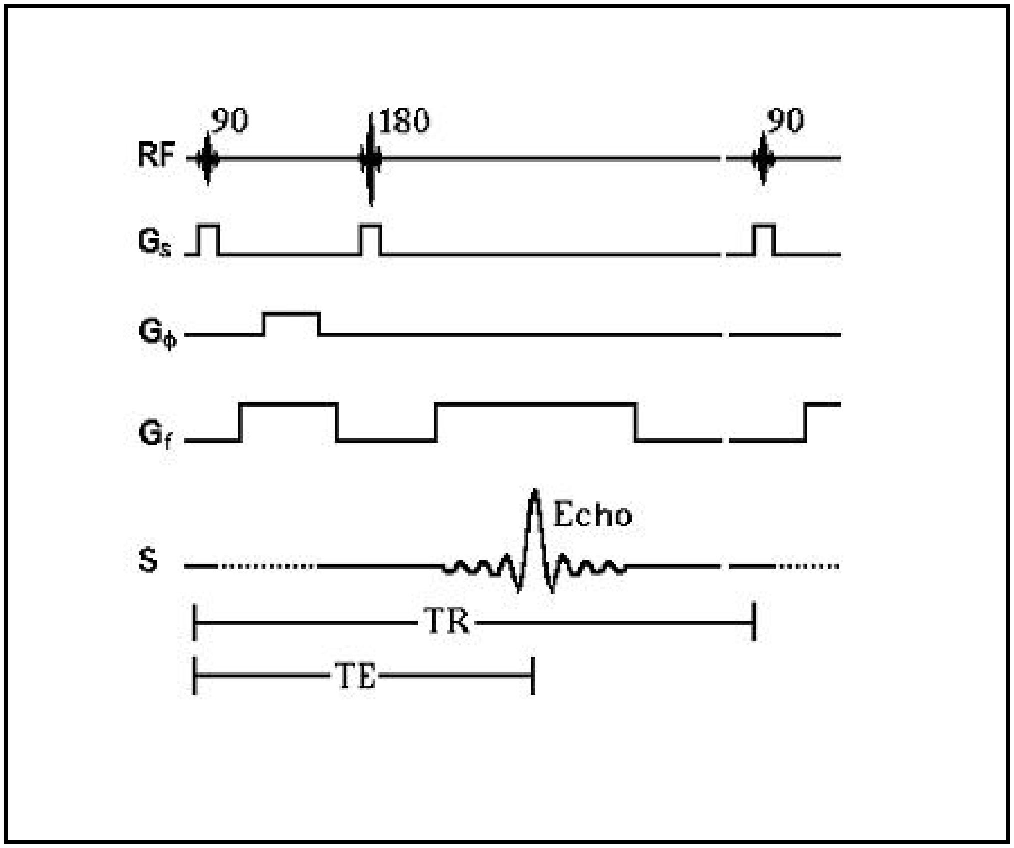

Figure 2.6: A Spin-Echo MRI pulse sequence, showing placement of the rf pulses, slice select gradients (G_s), frequency encode gradients (G_f), phase encode gradient (G_ϕ), spin echo, echo time (TE), and repeat time (TR). Time runs along the horizontal axis.

oil and therefore have the same T1 and T2. We used intensity differences due to spin densities for contrast, in particular by employing NMR sensitive and non-NMR sensitive particles within the same experiment. For example, in some of the biparticulate studies we will discuss one particle species contained NMR sensitive oil while the other was a cellulose acetate which does not show up on the MRI images.

2.6 MRI to Study Granular Flow

Due to its unique capabilities MRI is an extremely useful non-invasive tool to probe the subsurface of opaque systems such as granular flows. It has been used as described in the previous section to probe structure and density information in granular flow [40], and MRI may also be used to measure an array of dynamical variables such as velocity and diffusion [17, 18, 49].

Static MRI images of the bulk structure have also given important and heretofore unknown information about axially segregating biparticulate systems. For example, band formation was shown to begin from undulations of the radially segregated core of material rather than from the surface of the flow [40]. Also, 1D MRI projection imaging allowed us to acquire images at a rate of 1 Hz to probe the time evolution of the formation of axial banding as it is occurring, as will be discussed in Chapter 7. However, for dynamic variables further manipulation of the gradient field is necessary to encode the desired information. For velocity field information, the dynamic variable of interest within this thesis and discussed in Chapters 3, 6, and 7, we can create a velocity dependant phase change of the spins, in the direction of the velocity component of interest, by applying a bipolar magnetic field gradient along that direction.

Recall that an MRI signal is composed of both an amplitude and phase. Thus, any applied linear gradient pulse will give an additional phase to each spin depending upon their current location, according to,

$$\phi = \int \omega(t)dt = \gamma \int B(t)dt = \gamma \int G_x(t)x(t)dt, \tag{2.17}$$

where ω is the Larmor precession frequency, γ the gyromagnetic ratio, and G_x the

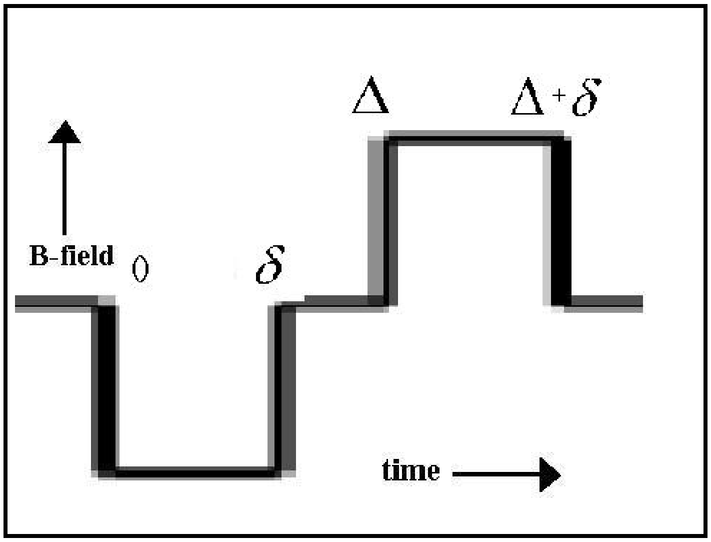

Figure 2.7: Bipolar magnetic field gradient, $G = \frac{dB}{dx}$.

gradient amplitude. The Taylor series expansion of x(t) is,

$$x(t) = x_0 + vt + at^2 + ... \tag{2.18}$$

If we define the n-th moment of the gradient as,

$$m_n \equiv \int t^n G_x(t)dt \tag{2.19}$$

then,

$$\phi = \gamma[x_0 m_0 + v m_1 + \frac{a}{2} m_2 + ...]. \tag{2.20}$$

For the case of smooth, steady, flows x(t) may be truncated,

$$x(t) = x_0 + vt \tag{2.21}$$

and

$$\phi = \gamma[x_0 m_0 + v m_1]. \tag{2.22}$$

If the spins are stationary when an equal and opposite (i.e., bipolar) gradient is applied the two parts will exactly cancel the phase, and the spins will have acquired no additional phase at readout. If, however, the spins moved along the gradient during the time between the application of the first and second gradient pulses, then the phase acquired during the first gradient pulse will not be canceled completely by the second pulse and at readout spins will have an additional phase change dependant on how far they have moved. For a bipolar pulse the first moment is,

$$m_1 = \int_0^{\delta} tGdt + \int_{\delta+\Delta}^{\Delta} tGdt = G[\frac{\delta^2}{2} + \frac{\Delta^2}{2} - \frac{\Delta^2}{2} - \frac{\delta^2}{2} - \delta\Delta] = G\delta\Delta \qquad (2.23)$$

therefore,

$$\phi = \gamma G \delta v \Delta, \qquad (2.24)$$

since the zeroeth moment cancels. Δ is the time from the start of first gradient pulse to start of the second gradient pulse of the bipolar sequence and δ is the gradient duration (Fig. 2.7). Hence, *moving spins experience a linear (in gradient strength) velocity-dependant phase change* when subjected to a bipolar gradient pulse. A velocity image is therefore a phase image. From this the average velocity of the spins during the measurement interval can be determined. The magnitude of the average velocity at each point is proportional to the Fourier transform of the signal at that point in the image. For an example see Fig. 2.8, where the velocity of the flow is shown. The reddest areas are moving fastest to the right and down, the area which matches the background is where the flow crosses zero, and the flow below this is moving to the left at the solid body rotation rate.

When there are velocity distributions within a voxel (= volume element) there will be signal loss because ϕ is proportional to v, the average velocity. This can degrade velocity images, but can be used to measure other variables of interest in

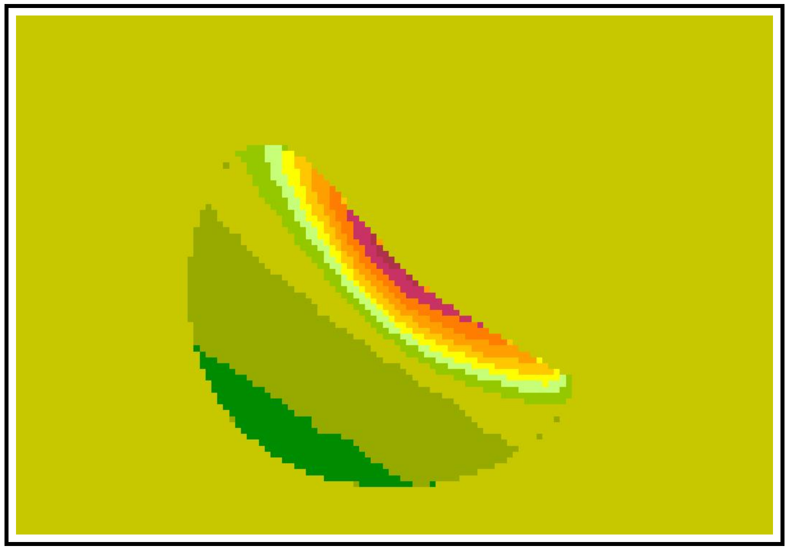

Figure 2.8: Velocity field image of the dominant component of velocity.

granular flow, such as velocity fluctuations which are closely related to the granular temperature. Additionally, if the flow is accelerating the phase change of the signal will no longer be proportional to the velocity, due to having to retain the second, acceleration dependent, moment when calculating Eq. 2.20. Therefore it is smooth steady flows that are best imaged with the bipolar velocity encoding technique described here.

Phase changes due to factors other than the movement of the spins must be eliminated from the velocity images. One way to accomplish this is to take images at more than one gradient amplitude and then plot the change in ϕ within each voxel due to the change in the first moment of G_x. From the slope of this line any extraneous phase contribution may be eliminated. This is done point-by-point and leaves only the contribution due to the velocity of the moving spins.

Once the signal is read out, the Fourier transform taken, the frequencies related to position, and phase changes due to factors other than velocity eliminated, the result is an image of the average velocities of the spins in each voxel in position space. We confine ourselves to the study of this type of smooth, steady, flow throughout this manuscript except where otherwise noted. Once velocities have been determined derived quantities of interest such as shear, may be calculated.

2.7 Flow Compensation

A similar technique to that described above for velocity imaging may be used to *remove* unwanted phase changes due to flow. This technique is termed "flow compensation" and uses a second set of bipolar pulses immediately after, and a mirror image of, the first. This causes the second, velocity dependent, moment of Eq. 2.20 to be zeroed. Therefore, no phase changes due to velocities in a direction which is flow compensated will appear in MRI images. In this way density images can be obtained even when the system is flowing.

2.8 Experimental Setup

Our experimental setup consisted of a 1.9 Tesla superconducting horizontal bore magnet, with the appropriate radio frequency probe and the gradient coils necessary to acquire MRI images of hydrogen-1 nuclei; see Fig. 2.9. The useable bore of the magnet once the rf probe is inserted was 12 cm, and the length of the bore from which we could obtain a good signal was approximately 10 cm long. We used a variable speed motor to rotate the cylinder. The motor was placed 2 meters away from the magnet in order to keep it away from the strong fringe field of the magnet. The motor was attached to the cylinder by a long non-magnetic shaft. The cylinder was then placed inside the rf coil on rollers which allowed it to rotate freely. All cylinders used were made of acrylic with smooth walls and smooth endcaps were made of the same material. Depending on the experiment the diameters and lengths of the cylinders varied.

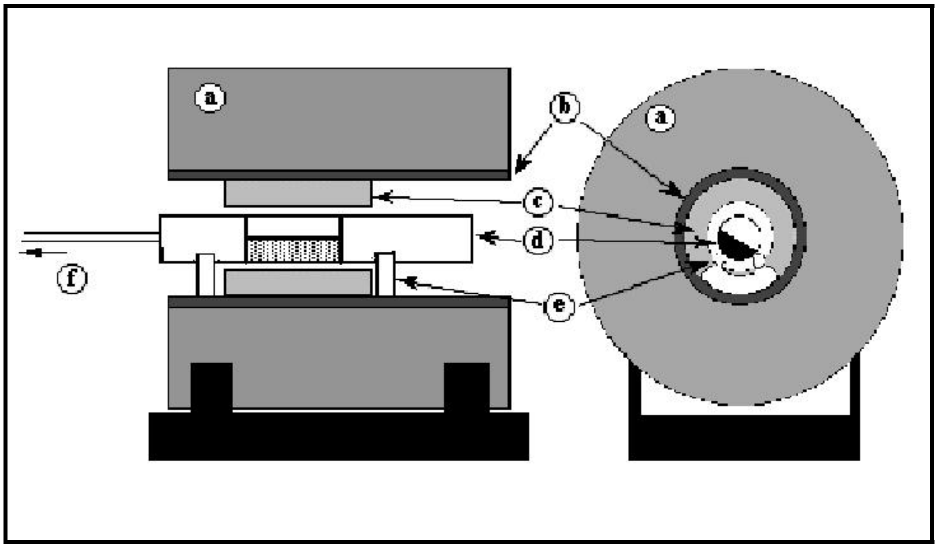

Figure 2.9: Illustration of the experimental set-up for the MRI experiments, showing the placement of the cylinder(d) on supportive rollers (e) within the superconducting magnet (a). Also included in the picture are the radio frequency (rf) probe (c) and the gradient coils needed for spatially resolved location and velocity information (b). For those measurements taken while the cylinder was rotated within the magnet, the motor was kept out of the way of the strong magnetic field with a long driving shaft (f), as illustrated in the picture.

The particles used were smooth spherical beads of two types and one type of smooth, approximately spherical, mustard seed. The first type of beads were NMR sensitive pharmaceutical beads, containing hydrogen-rich oil that can be easily imaged using MRI. Solid-state NMR is difficult due to the lack of translational motion of the atom containing the spins. In liquids, the translational motion of the atoms averages the magnetic dipole interaction between the spins to nearly zero. In contrast, the dipole interaction in solids renders the conventional MRI techniques nearly useless. Using liquid-filled particles, as we do here, alleviates this problem. The density of the pharmaceutical beads is 1.1 $\frac{g}{cm^3}$. We used various diameters of these beads ranging from 1mm to 4mm. The second type of particle used were cellulose acetate and do not appear in the MRI images. These have a $\rho = 1.6\ \frac{g}{cm^3}$. The densities of the two types of beads are similar enough so that when particles of the same size are rotate together they become well mixed. The mustard seeds naturally contain an NMR sensitive oil and have a density of $\rho = 1.3\ \frac{g}{cm^3}$.

Chapter 3

Velocity Depth Profile

As mentioned in the Introduction, granular flows in horizontal rotating cylinders are often studied as representative systems important for both theoretical work and in practical applications such as calcination, mixing, and drying. Yet there remain a number of unanswered questions about the behavior of these flows. One characteristic of interest is the form of the velocity depth profile in the lens-shaped flowing region.

Understanding the reason for the shape of the velocity depth profile for this system, that is, why it has a particular form, may give insight into not only the dynamics of systems of identical particles, but may also play a role in understanding the segregation of systems containing particles with differing characteristics such as size or density [50]. The form of this variable can give insight into other aspects of the flow as well, such as stress and strain relations. Often it has been taken to be linear in the flowing region with a slow deformation or exponentially decaying area introduced between the flowing and solid body regions in both theories and experimental fits [19,20,29,36,51,52]. However, momentum balance implies that the shear stress increase linearly with depth, and for a linear velocity profile the shear would be a constant. It is also noted that if the velocity profile is linear, this in

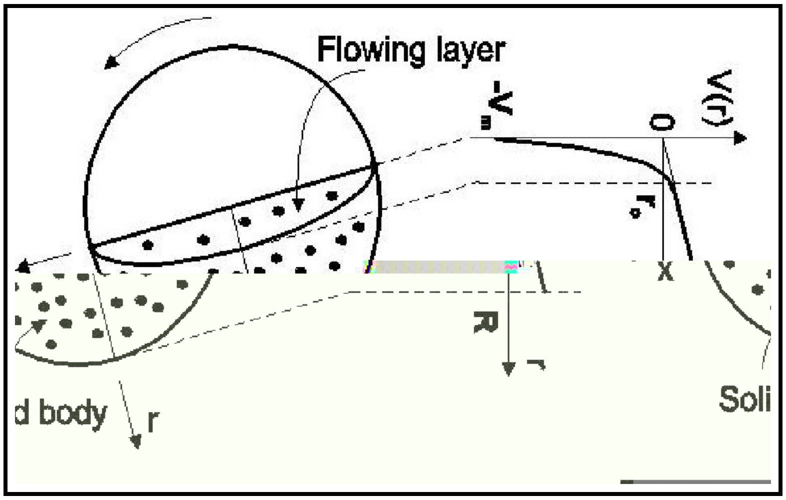

Figure 3.1: Velocity depth profile is measured along the perpendicular bisector to the free surface of the flow.

incompatible with any local and one-to-one stress/strain constitutive relations.

The velocity depth profile in this geometry has been investigated experimentally in 2D and at the endwall [19–22], but rarely at the axial center of a long cylinder. One notable exception was in 1997 when, using MRI to study flow at the center of a long cylinder, Nakagawa and coworkers [35] observed that the velocity depth profile along the perpendicular bisector in the shear flow layer of a half-filled cylinder may be fit by a quadratic polynomial,

$$v(r) = V_m(1 - r/r_0)^2 - \Omega r, \qquad 0 < r < r_0 \tag{3.1}$$

and, as expected, in the solid body layer by a line,

$$v(r) = -\Omega r, \qquad r < r_0 < R. \tag{3.2}$$

Here V_m is the velocity at the free surface, r is the position along the perpendicular bisector of the flow with the origin at the cylinder center, r_0 is the depth of the flowing layer, and Ω is the rotation rate of the cylinder. This fit pertains to the dominant component of velocity in the direction of flow, as a function of depth in the flowing layer (Fig. 3.3). These authors also noted that the quadratic form is consistent with an energy dissipation minimization criterion, postulating uniform particle density (which is a good approximation at low rotation rates) in the flowing region. They began with the assumption that a dissipation minimization condition applies along the radius perpendicular to the flowing surface, and therefore only a 1D integral needs to be minimized,

$$\frac{dE}{dt} \propto \int (\frac{dv}{dr})^2 \cdot dr. \tag{3.3}$$

They carried out the minimization using the Euler-Lagrange variational method, with the conditions that the total flux across the radius be zero, yielding,

$$v(r) = ar^2 + br + c. \tag{3.4}$$

Inserting the appropriate boundaries for a 50 percent filled cylinder with no slip at the wall, rotation rate Ω, flowing layer thickness r_0, and free surface velocity V_m,

$$v(0) = V_m, \tag{3.5}$$

$$v(r_0) = -\Omega r_0 = ar_0^2 + br_0 + V_m, \tag{3.6}$$

and for continuity of the derivative across the boundary,

$$\frac{dv}{dr}|_{(r \to r_0^+)} = -\Omega, \tag{3.7}$$

$$\frac{dv}{dr}|_{(r \to r_0^-)} = 2ar_0 + b. \tag{3.8}$$

Therefore,

$$c = V_m, \tag{3.9}$$

$$b = \frac{2V_m}{r_0} - \Omega, \tag{3.10}$$

$$a = -\frac{V_m}{r_0^2}, \tag{3.11}$$

leading to Eq. 3.1.

Nakagawa, et al. [35] additionally found that the quadratic fit of Eq. 3.1, that is good at low rotation rates, develops a deviation near the free surface at higher rotation rates, with the velocity close to the free surface falling below the quadratic function. We also observed this deviation with increased rotation rate as can be seen in Fig. 3.2, where we have plotted the $\sqrt{v + \Omega r}$ against $1 - r/r_0$, so that according to Eq. 3.1 the slope is $\sqrt{V_m}$. This figure shows six different rotation rates and the departure from Eq. 3.1 at the higher velocities for the higher rotation rates is clear. The deviation in the lower left is due to particles in the solid body region and, therefore, not expected to fit Eq. 3.1, but rather Eq. 3.2.

It was theorized that the deviation from the quadratic is due, at least in part, to inertial effects. At high rotation rates particles emerging from the solid body layer into the flowing layer can have a large component of velocity perpendicular to the free surface that causes them to unweight from the surface. These particles also have less overburden than those below, which reinforces the unweighting and causes the shape of the free surface, which is flat at slow rotation rates, to become S-shaped as the rotation rate is increased (going from the rolling regime into the cascading regime). When particles unweight two things happen. First, the particles will experience increased air resistance. Second, the particles will experience large

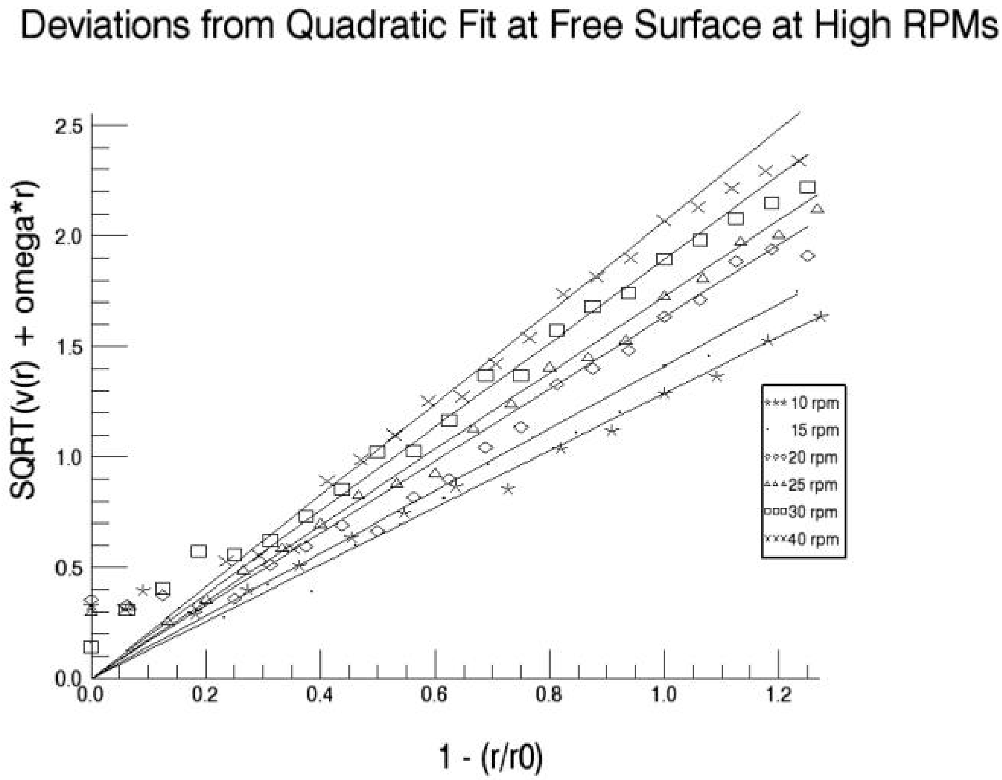

Figure 3.2: Velocity depth profiles are well fit by a quadratic at low rotations rates. At high rotation rates a deviation from the fit develops near the free surface.

collisional losses when they return to the free surface. Therefore, they will not efficiently convert their kinetic energies into velocities in the flow direction and have no way to catch up to otherwise identical particles that did not leave the surface. Thus, the unweighting slows the particles in analogy to ski racers who attain the fastest speeds by staying on the slope rather than becoming airborne. A striking example of this can be seen in the early MRI tagging experiments reproduced as Figure 1.9 of the Introduction [35]. Initially, noninvasive parallel tags are placed on the particles of a transverse slice in the axial center of a 3D cylinder. The tags remain straight and rotate with the cylinder except where the particles move with respect to the cylinder and bend the tags. Fig. 1.9 shows the tags after a delay of 46 ms, for a fast rotation rate of 9.9 rad/s (95 rpm). The bent tags show that the unweighted particles have slowed so much that the fastest flowing particles are now well below the free surface. These results suggest that we might achieve velocity profiles that better agree with the quadratic form if we identify and suppress the mechanism(s) responsible for the deviation seen at the higher rotation rates. To test this we placed a paddle on the top 3 cm of the flow at approximately the dynamic angle of repose to prevent the particles from unweighting and to force them to remain on the flowing layer as they emerged onto the free surface (Fig. 3.3).

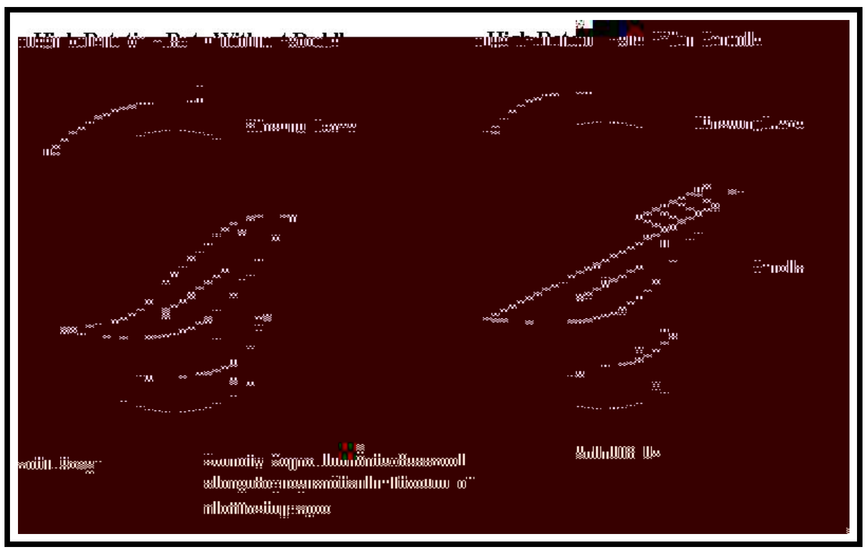

Figure 3.3: Schematic of granular flow in rotating cylinder with and without a paddle at same rotation rate.

We measured the velocity profiles using MRI and compared cylinders rotated with and without the paddle at many different rotation rates. Our results show that the quadratic fit is better with the paddle than without when the comparison is made at the same solid body rotation rate, at the same free surface velocity, and with the paddle placed at different positions, so long as it makes good contact with the surface.

We used an 8.8 cm inner diameter, 10.3 cm long acrylic cylinder half-filled with either 2 mm diameter mustard seeds or 3 mm diameter pharmaceutical beads, both of which contained MRI sensitive liquids. The cylinder was then placed inside the birdcage coil on rollers and rotated with a variable speed motor. We used MRI velocimetry as described in Chapter 2 to obtain velocity profiles from a slice orthogonal to the axis and 0.5 cm wide at the axial center of the cylinder, far from the endcaps.

Bulk flow at this location occurred along the free surface without any net axial velocity component. Any axial components of velocity due to random movements were flow compensated. Data, which were taken in the x- and y-directions in the lab frame, were combined to form the component of velocity parallel to the free surface of the flow. We fit the experimental velocity depth profile along the perpendicular bisector of the free surface, i.e. the midpoint of the downhill flow, to Eq. 3.1 with V_m, r_0, and Ω as parameters to be determined by the fit. First, Ω was fixed from the slope of the straight section of the profile corresponding to the solid body rotation layer. We used this measured rotation rate, as opposed to the rotation rate the cylinder was rotated at to eliminate any uncertainty caused by possible slippage at the cylinder wall. The quadratic function was then fit to the remaining points, excluding points very near the free surface, thereby fixing the value for r_0. Finally, we determined if and where the data points deviated from the quadratic as the free surface is approached. This was done by sight and confirmed by the fit having the smallest chi-square deviation, compared with fits that included points closer to the free surface of the flow. Fits which excluded additional points did not improve the chi-square value to two significant figures.

The same experiment was repeated with and without a paddle placed over the uppermost 3 cm of the free surface at approximately the dynamic angle of repose of the flow (Fig. 3.3) at many different rotation rates. The acrylic paddle spanned the axial length of the cylinder and its ends were attached to two acrylic disks that fit concentrically inside the cylinder. The paddle could easily be rotated to different orientations, or fixed, from outside the cylinder by rotating a rod which was attached to one of the acrylic disks that held the paddle and exited the cylinder through an opening at the center of its endcap. The other disk also had a rod attached to its center that exited the cylinder through the center of the other end cap. This rod was not attached to anything but only served the function of an idler to support the end of the paddle. Once in place the paddle apparatus remained still while the cylinder rotated around it.

In order to have the same solid body rotation rate with and without the paddle, the cylinder needed to be rotated faster when the paddle was present in order to overcome the slippage of the solid body of particles at the cylinder wall due to the paddle's friction. The rotation rates Ω quoted here are the values measured by MRI in the solid body layer of particles.

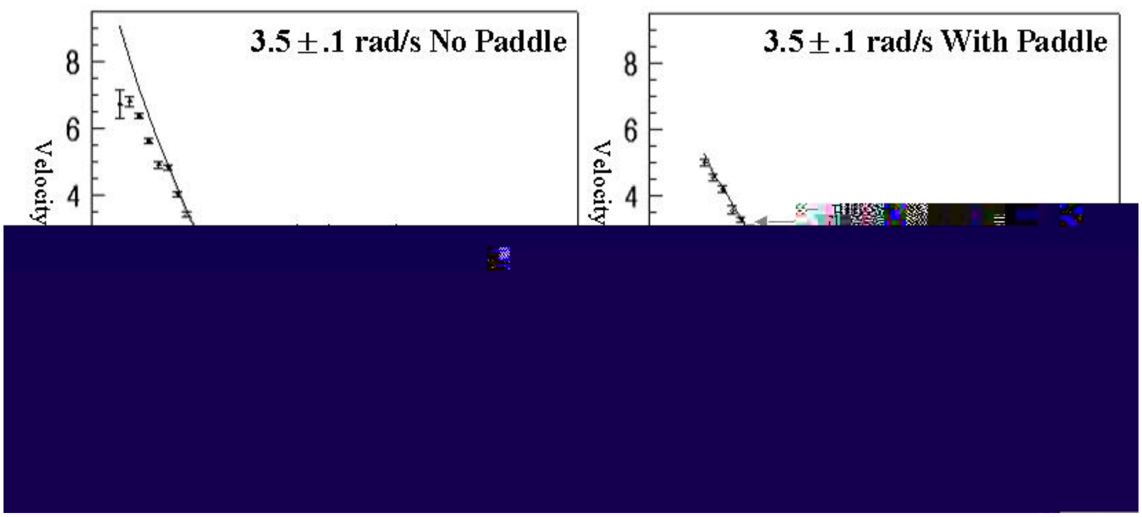

Figure 3.4: Comparison of velocity depth profiles with and without paddle at a rotation rate of 3.5 ± .1 rad/sec

We compared flows at the same solid body rotation rate with and without the paddle. In the approximately 30 cases studied, the velocity profile taken with the paddle was an equal or better fit to a quadratic velocity depth profile than data without the paddle. Preliminary experiments by Heine, et al. [53] showed the same results. The deviation from the quadratic form of Eq. 3.1 when no paddle was present was most pronounced at high rotation rates for both pharmaceutical beads and mustard seeds. This is expected if the deviation from the quadratic profile is caused by the unweighting of the particles arriving at the free surface as we have proposed. To make our results quantitative, and to be assured that the results were robust, we ran repeated runs at the same rotation rate. Figure 3.4 shows data with a solid body rotation rate of $3.5 \pm .1$ rad/s (33 ± 1 rpm) with and without a paddle and averaged over 5 experimental runs. The fit to the quadratic function of Eq. 3.1 in the flowing layer with the paddle is excellent and the deviation from the quadratic function without the paddle is unambiguous.

We also investigated the importance of properly locating the paddle. To do this we placed the paddle at different positions and observed how this affected the quadratic fit. We found that when the paddle was brought down far enough so the resulting free surface was flat, the flow velocity profile fits the quadratic form of Eq. 3.1. When the paddle was lowered further, the velocity profile remained quadratic but both the flow and the solid body regions slowed until the particles eventually jammed. Thus, the placement of the paddle is not critical to the quadratic fit, provided the paddle makes good contact with the free surface and the system doesn't jam.

Finally, since the paddle slows down the surface flow due to the particles experiencing additional friction when sliding under it, we compared data with the same free surface velocity but different solid body rotation rates (Fig. 3.5). (It was not possible to get both the same solid body rotation rate and maximum free surface velocity with and without the paddle.) We found the results to be the same, that is, the fit to the quadratic is better with the paddle than without.

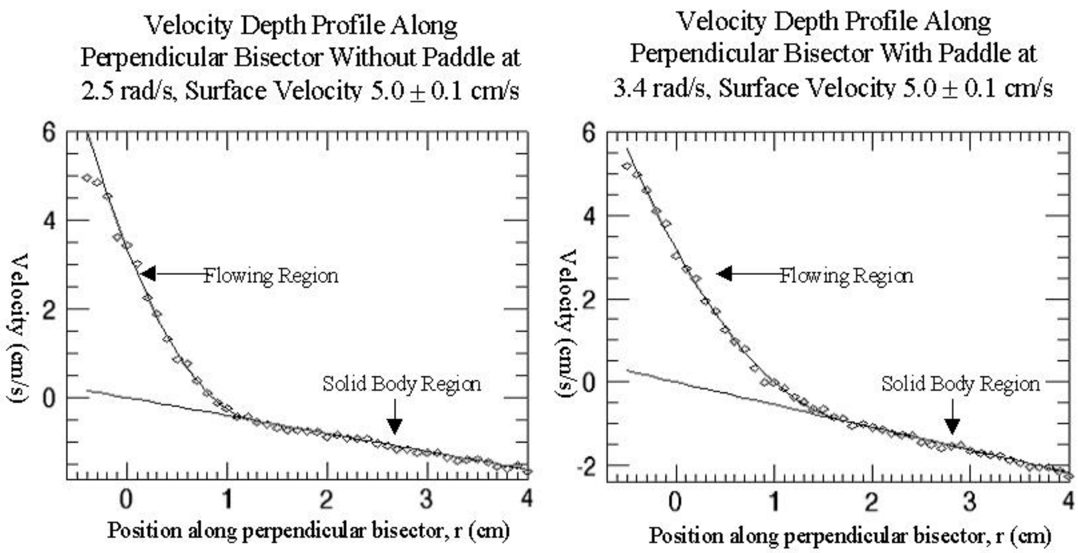

Figure 3.5: Comparison of velocity depth profiles with and without a paddle at the same free surface velocity.

We found that using a paddle to null the azimuthal velocity of particles being brought up to the free surface in a half-filled horizontal rotating cylinder causes the velocity depth profile along the perpendicular bisector of the flowing layer (which already obeys a quadratic dependence except near the free surface) to agree with the quadratic profile even very close to the free surface. It is important to note that it is only close to the free surface that a deviation is ever seen, the point of deviation moving deeper into the flowing layer at higher rotation rates. Every experimental run showed either a better fit to a quadratic velocity depth profile with the paddle, or at least as good a fit, than without the paddle.

This result strongly suggests that a quadratic velocity depth profile may be a fundamental property of granular shear flows in horizontal rotating cylinders when the effect of the cylinder rotation is to transport the particles from the end of the flow to the beginning without imparting velocity perpendicular to the free surface flow. The small deviations from the quadratic form seen even with the paddle are not surprising. The particles on the free surface do not have the overburden felt by particles deeper in the flowing layer so they can more easily become airborne due to collisions, albeit to a small degree compared to the particles that experience unweighting due to the rotation of the cylinder when they do not encounter a paddle upon emerging at the free surface.

The quadratic function observed in this work offers an attractive alternative to the hybrid of two straight lines joined by a transition region [19, 20, 29, 36, 51, 52]. Such a hybrid, we believe, works for flows at moderate rotation rates without a paddle because in such cases the particles near the free surface slow down due to unweighting, accidentally making the velocity dependence more linear. However, as the rotation rate is increased the velocity profile continues to deviate further from the quadratic function, eventually bending over as the highest particles begin to flow slower than those beneath as seen in the early MRI tagging experiment of Fig. 1.9.

Comparing the two fits at low rotation rates where the comparison may be meaningful, we find no statistically significant difference in the goodness of fit using a t-test. Thus the quadratic dependence of Eq. 3.1 fits the experiments as well as, if not better than, even a hybrid fit of two straight lines plus a transition region, further supporting the idea that a *single* mechanism determines the velocity depth profile in the flowing region of the horizontal rotating cylinder geometry. If our supposition is correct, this has implications for the development of theories of granular flow, which have almost invariably assumed a linear velocity depth profile.

Even when theories are not critically dependent on the exact form of the velocity depth profile, i.e. approximating a quadratic profile as linear would work equally well, the difference between the two forms has implications as to how the flow is thought about. If the velocity profile is quadratic this implies a linear shear rate in the flowing region. If on the other hand, the velocity profile is linear this implies that there cannot be any local and 1-to-1 constitutive relations and that the shear rate is constant in the active layer.

Chapter 4

3D Cellular Automata Modeling of Granular Segregation

As previously introduced, granular materials of differing properties, such as size or density, tend to segregate (unmix) when rotated in a three-dimensional horizontal cylinder. The segregation is of two types, a quickly occurring radial segregation and a more slowly evolving axial (banding) segregation. If the rotation is continued, a coarsening of the banded structure is sometimes seen. These phenomenon have been observed experimentally both on the surface [54] and below the surface [40] of the flow. Yet, current theoretical understanding of axial segregation and later band coarsening is incomplete.

Cellular automata (CA) simulations are a simple phenomenological way to test how varying combinations of particle properties may affect the segregation pattern of large systems of particles over both short and long time scales. The study of such large systems for long times can make other types of simulations, such as the more commonly used particle dynamic (PD) simulations, prohibitively calculation intensive. Furthermore, although PD simulations are exact in principle they rely on precise physical properties and interaction models [55], which are not necessarily well understood for granular materials. Monte Carlo (MC) simulations, another commonly used simulation type to study granular flows, are often too idealized to mimic specific materials [56] and are also calculation intensive. We have chosen here to use CA computations, both because they can often yield insight, even though some specificity is sacrificed when compared with other types of simulations, and because they can easily be run on a PC, as were all the simulations discussed below. A 10000 time-step simulation took approximately 24 hours to complete on the lab PC.

In this Chapter we present the results of our 3D cellular automaton, which simulates the qualitative features of the time evolution of granular flow in a rotating drum. The system being modeled is composed of equal amounts, by volume, of two differently sized particles. By varying the frictional properties of the biparticulate system both the segregation and mixing behaviors observed experimentally could be reproduced [57, 58]. Further, if the larger particles were given a much greater friction coefficient than the smaller particles a reversal of the sense of radial segregation occurs. To our knowledge this is the first time that a CA model has been used to simulate 3D biparticulate granular systems in a rotating drum geometry whose constituent particles differ in both size and frictional properties. Finally, we investigated the effect of allowing a biparticulate system of the same size particles with different frictional properties to exchange particles between layers. It was found that allowing layers to exchange particles may accelerate axial band formation and band coarsening.

The linear dimensions of the simulated particles were a 2:1 ratio in the x-y, i.e. transverse, plane but had the same axial extent, the larger particles did not extend any further in the axial direction than the smaller ones. The larger particles were, therefore, square disks rather than cubes (Fig. 4.2, Inset). The relative frictional properties of the particles were systematically varied, but the sizes of the particles remained constant in all of our simulations, unless otherwise noted. A matrix (N_x=16, N_y=60, N_z=80) was alternately populated with one layer of larger particles and then two layers of smaller particles until it was half full (Fig. 4.1, (a)). There were, therefore, equal volumes of the differently sized particles. Periodic boundary conditions were imposed at the bottom of the cylinder, while the walls of the cylinder were simulated by immobile particles with the same frictional properties as the smaller mobile particles.

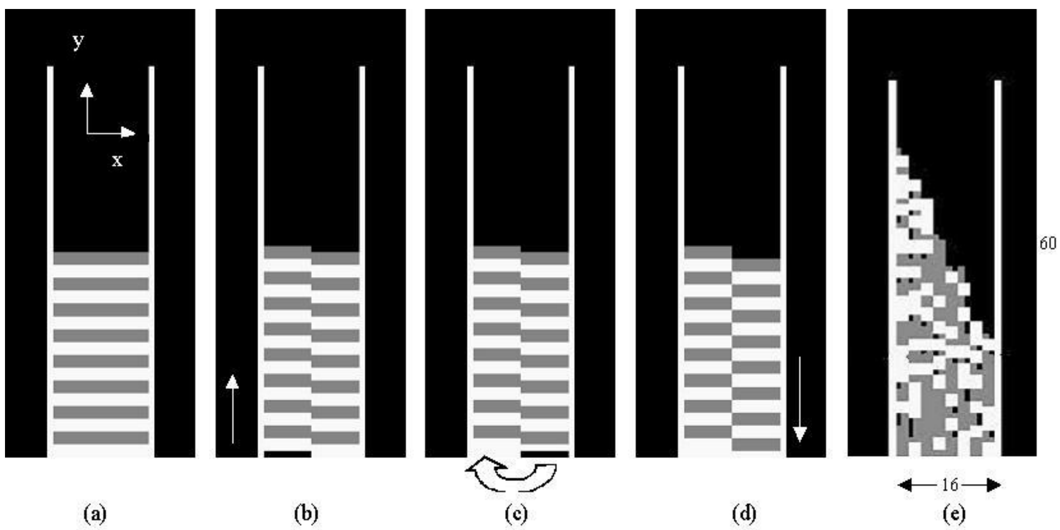

Figure 4.1: Simulation of the rotation of the cylinder. The smaller particles are gray and the larger particles white. a) Initial condition of cylinder; b) LHS of cylinder moved up; c) bottom of RHS of cylinder flipped over to bottom of LHS of cylinder; d) RHS of cylinder moved down; One time step completed. e) Long-term evolution (1000 time steps) of a system of particles that mixes.

The evolution of the system was based on that of a CA simulation developed by Yanagita [14], which used particles of the same size but different frictional properties. There are two steps in the evolution of the system. First, the cylinder must be rotated. Second, the particles may move to a lower position on the surface based on the criteria described below.

The rotation of the cylinder at each time step is accomplished by moving the left half of the cylinder up by one cell, i.e. where x less than $N_x/2$, turning over the bottom-most layer of cells on the right side and placing it in the newly vacated cells on the left side, and then moving the right side down by one cell, i.e. where x greater then or equal to $N_x/2$ (Fig. 4.1, (a)-(d)). This creates a height difference between the left and right sides of the cylinder, which after a number of time steps becomes a smooth dynamic angle of repose (Fig. 4.1 (e)).

Next, a particle is randomly selected from the surface. The frictional coefficient between two small particles is denoted as F_{aa}, between two large particles as F_{bb}, and between a small and a large particle as $F_{ab}(= F_{ba})$. The local friction experienced by the randomly selected surface pixel is calculated by adding up the F_{ij} 's between the particle and the contacts that it makes with neighboring pixels that belong to other particles. The neighboring pixels considered are the one beneath (Δy = -1, for a small particle or -2, for a large particle), and the ones on the sides (Δz = +1 and -1) of the selected pixel; the pixel behind (Δx = -1 or -2) is not considered to contribute to the local friction the particle experiences. The frictional coefficients are chosen so that the resulting dynamic angle of repose is not so high that the particles are pushed out of the simulation at the top and not so low that a flat surface results.

A new position for the particle is then randomly chosen from one of the neighboring positions in front of or next to the particle (Δx = 0 or +1; Δz = +1, 0, or -1). the particles are, therefore, allowed to move axially. The height difference between the particle and its new position is calculated. If the height difference is greater than the local friction felt by the particle, and there is enough space for the new particle (this being relevant only for the larger particles) then the particle is allowed to move to the new position. If not it remains where it is. If any smaller particles are left "floating" due to the movement of a larger particle they are then allowed to fall to

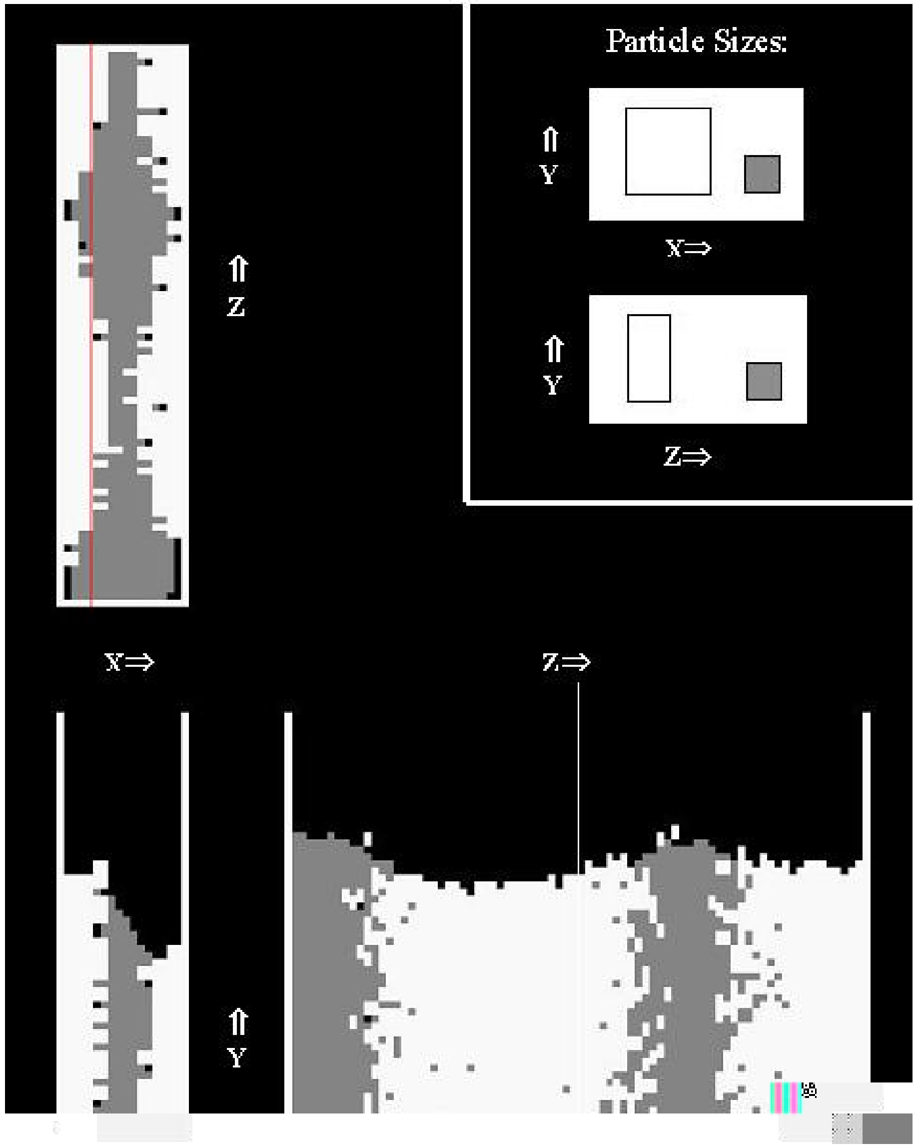

Figure 4.2: Results of simulation after 60,000 time steps. White represents the larger particles and gray the smaller particles. Red line indicates where time evolution is observed, for reference in later Figures. Inset: Relative sizes of particles in each plane.

the surface. This process is repeated many times (r = 18000 or r = 36000 for these simulations) for each time step. Simulating a large number of time steps enables us

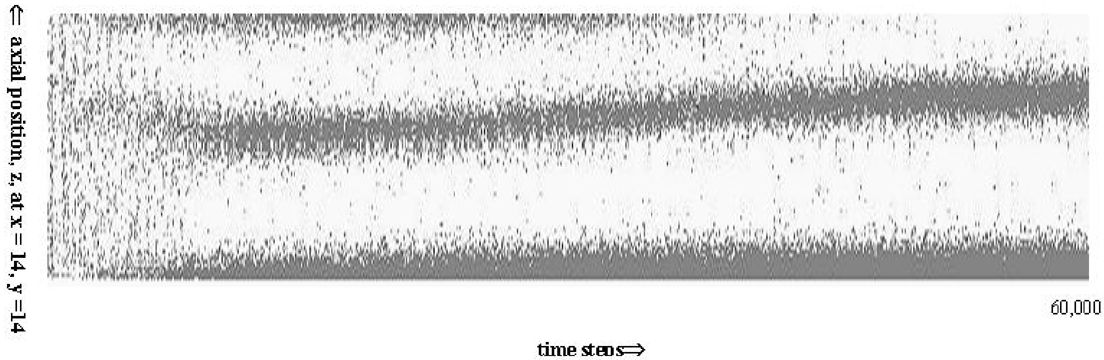

Figure 4.3: Time evolution of a system of two different particle sizes assigned identical frictional properties, at one value in the x-y plane, as shown by the red line in Figure 4.2, and at all axial locations.

to investigate the long-term evolution of the system.

The results of a simulation for which the frictional properties of the large and small particles were chosen to be equal are shown in Figs. 4.2 and 4.3. These figures exhibit both the quickly forming radial segregation and the more slowly evolving axial segregation of two differently sized particles observed in our experiments. In Fig. 4.3 we also see a coarsening of the banded structure, again consistent with experimental results. Thus, at least qualitatively, this CA simulation reflects what occurs in a horizontal rotating cylinder half-filled with particles of two different sizes. This is commensurate with what both Yanagita [14] for biparticulate systems, and Newey et al. [15] for multiparticulate systems, observed in CA simulations using particles differing in frictional properties only.

It was noted that when running the pure systems through the simulation the small particles had a larger dynamic angle of repose than the large particles, when both particle types were given the same frictional properties. For simplicity the simulation was implemented so that when a pixel was randomly selected from the surface only the local friction affecting that particular pixel was summed, regardless of whether it was a large or small particle. This is not very realistic. Therefore, we then adjusted the frictional properties of the two different sized particles so that the dynamic angle of repose was approximately the same for both types of particles (which yielded frictional coefficients of $F_{aa} = 0.6$, $F_{bb} = 0.7$, $F_{ab} = F_{ba} = 0.65$).

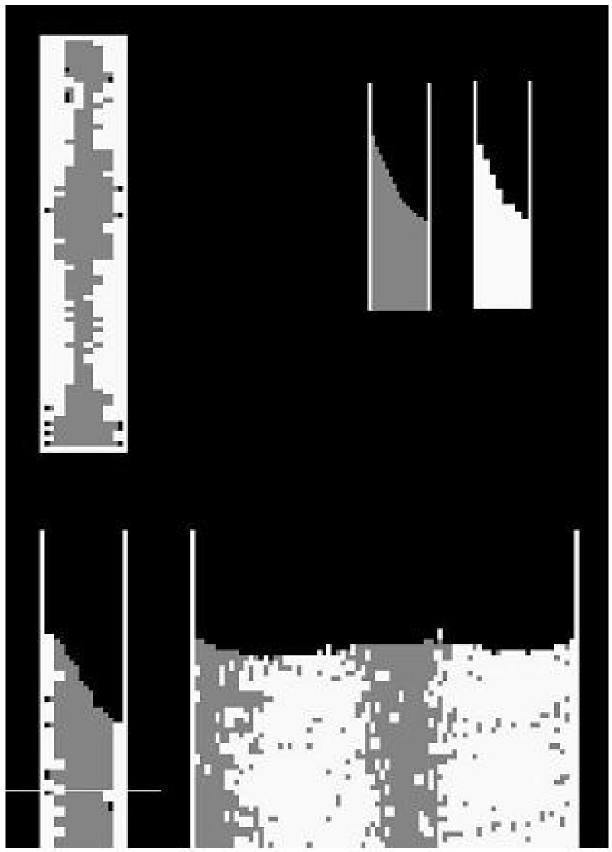

Figure 4.4: System of two different sized particles whose angles of repose are approximately equal. Radial and axial segregation are observed at 2000 time steps. Inset shows each of the pure systems run through the simulation, the dynamic angles of repose are approximately the same.

Experimentally, we find little difference in the dynamic angle of repose of flowing particles of different sizes and the same composition in the 1mm-4mm diameter range (Fig. 4.5). We found that both radial and axial segregation occur in the simulation,

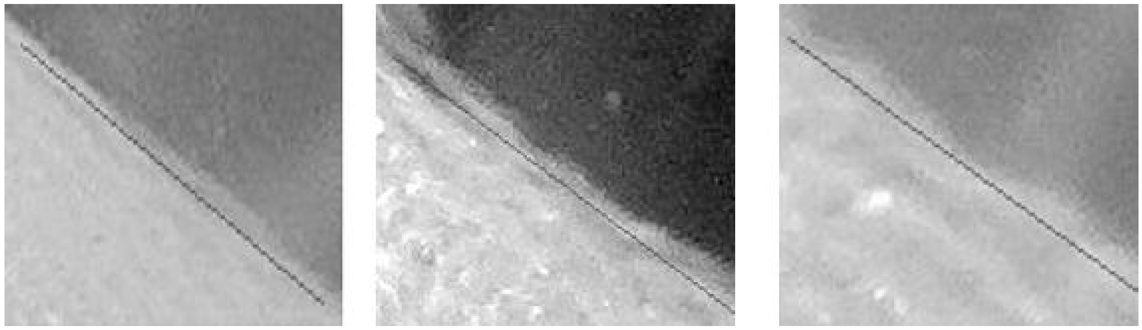

Figure 4.5: Dynamic angle of repose for pure systems of different sized particles, particle sizes from left to right are 2mm, 3mm, and 4mm. All particles are made of the same material and have the same dynamic angles of repose ± 1 degree.

but that the axial banding takes longer to form. Distinct axial bands do not form until approximately 20000 time steps, whereas when the smaller particles have the higher dynamic angle of repose (which implies they are experiencing a greater amount of friction) well formed axial banding segregation is observed at 10000 time steps. (Fig. 4.4)

We next changed where the height difference was measured from for the large particles while keeping the frictional properties of both particle types the same and achieved results in which the large and small particles had approximately the same dynamic angle of repose. For this 60000 time step run we found that it took a very long time for axial banding to develop, it was never particularly distinct and only one band of each particle type developed, see Fig. 4.6.

Next, the frictional properties of the two particle types were allowed to vary in the simulation. Results for 100 and 1000 time steps of systems whose combinations of frictional coefficients yielded interesting results are shown in Figs. 4.7 and 4.8. Fig. 4.7 shows the rapidly occurring radial segregation for those systems that segregate and the mixing which takes place for the system which does not segregate, while Fig. 4.8 shows an axial view of the time evolution of all systems. These systems are

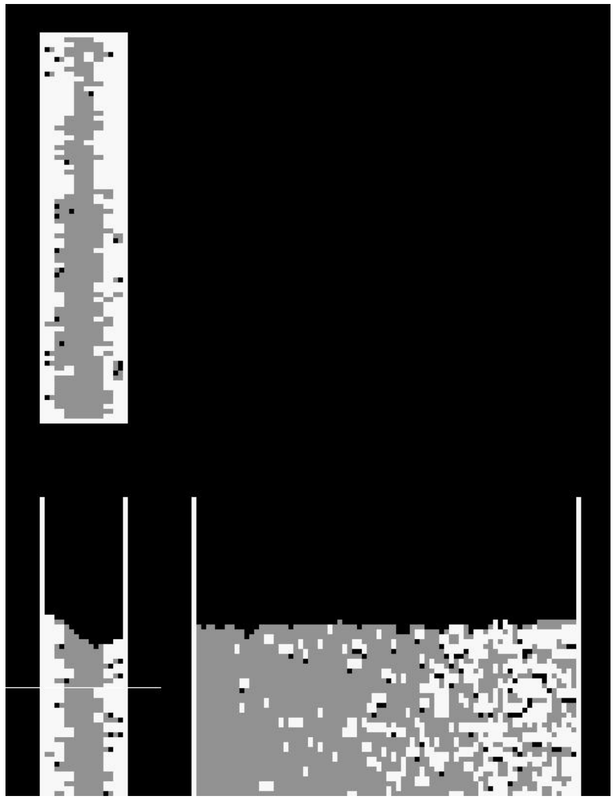

Figure 4.6: CA simulation, results for biparticulate system of different sizes with both same frictional properties and same dynamic angle.

described in detail below.

When the smaller particles have the higher frictional coefficient radial segregation is very rapid and complete, with almost no large particles remaining in the small particle core (Fig. 4.7 (a)). Axial banding also occurs quickly (Fig. 4.8 (a)). Our results for the case of the two differently sized particles with F_{aa}=F_{bb}=F_{ab} frictional properties are repeated for easy comparison in Fig. 4.7 (b) and Fig. 4.8 (b).

When the larger particles are given the greater coefficient of friction three results are observed. First, if the difference in frictional coefficients is small then the smaller particles still migrate to the radial center, just on a slower time scale. Second, if the

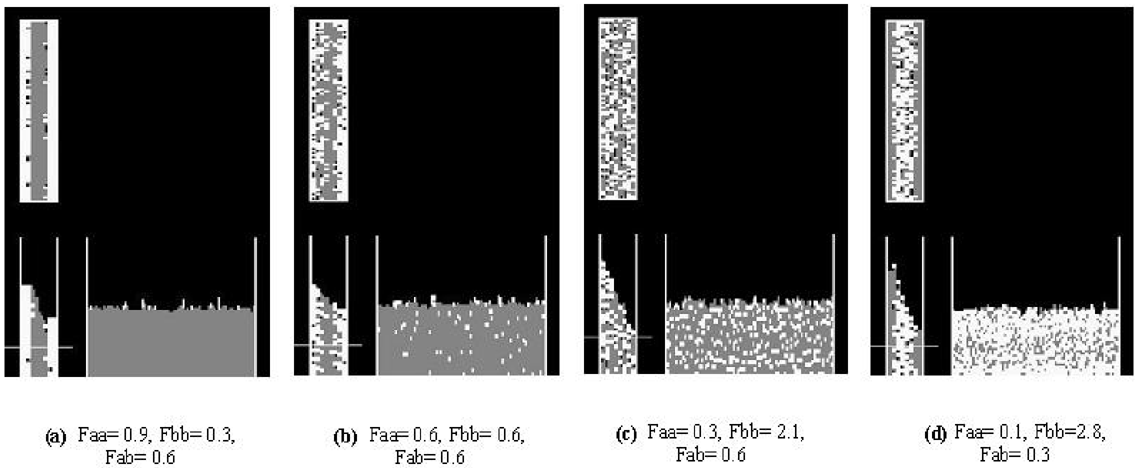

Figure 4.7: CA simulation results for biparticulate systems differing in both size and frictional properties after 2,000 time steps. Frictional properties are listed on figure.

difference is allowed to grow past some critical value, here a ratio of 7, the particles will not segregate but will mix (Fig. 4.7(c) and Fig. 4.8 (c)). Finally, if the ratio is allowed to grow very large, in Fig. 4.7 (d) a ratio of 28 is used, the sense of the radial segregation can be reversed so that the large particles are the ones that form the radial core. It is understood that this ratio of frictional properties is unrealistic, but we believe that useful information is still gained, so long as it is remembered that these are qualitative representations of actual systems. At 10000 time steps no distinct axial banding segregation is seen for this combination of particle properties (Fig. 4.8 (d)). If the system is allowed to evolve to 60000 time steps a distinct axial band of the smaller particles does form, but there is still no distinct axial band of larger denser particles (Fig. 4.9). The large particle radial core remains. Finally, we returned to a configuration where particles are of the same size but have different frictional properties, and which both radially and axially segregates (Fig. 4.10, top). We then allowed different layers to exchange particles, to test how this would affect the segregation pattern, if at all. First, particles between the topmost

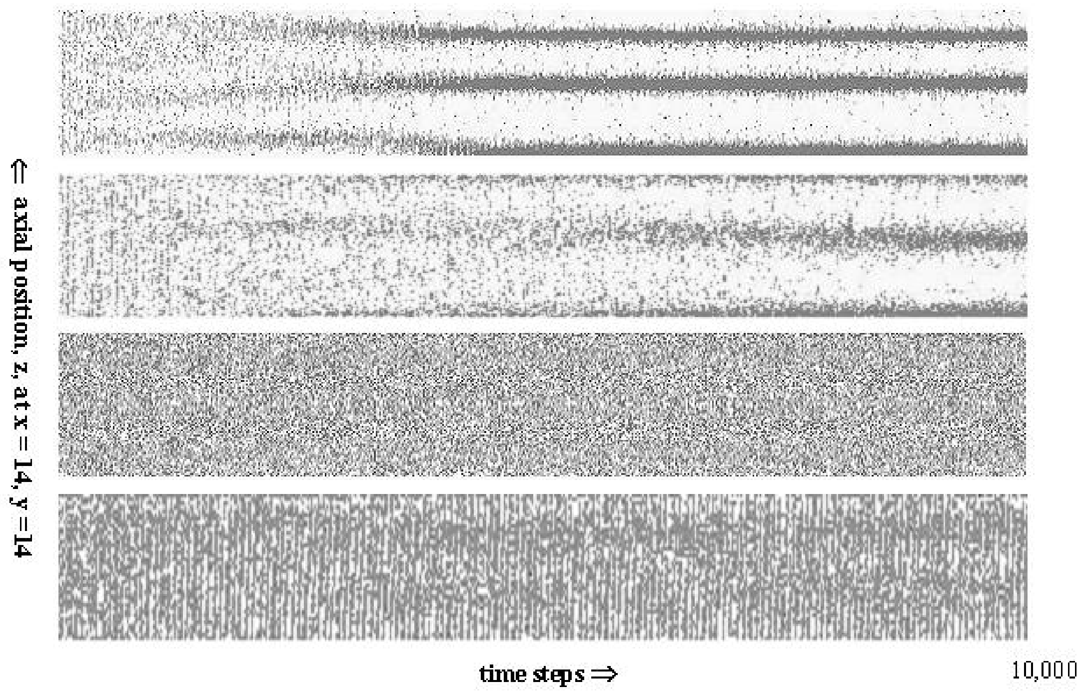

Figure 4.8: Time evolution of four different combinations of particle frictions, as described in text.

3 layers were permitted to exchange particles. 500 particles were randomly selected from the surface layer to switch positions with the particle directly beneath. Next, 300 particles were randomly selected from the layer one below the surface to switch positions with the particle directly beneath. Finally, 200 particles were randomly selected from the layer two below the surface to switch positions with the particle directly beneath.

Results at different time steps are presented in Fig. 4.10, middle. Another system was then run which allowed the 5 topmost layers to randomly exchange particles in the same manner as described above, with the number exchanged between layers being $N_{1\leftrightarrow 2}$=1000, $N_{2\leftrightarrow 3}$=800, $N_{3\leftrightarrow 4}$=500, $N_{4\leftrightarrow 5}$=300, $N_{5\leftrightarrow 6}$=200, with 1 indicating the surface layer. Results at different time steps are presented in Fig. 4.10, bottom.

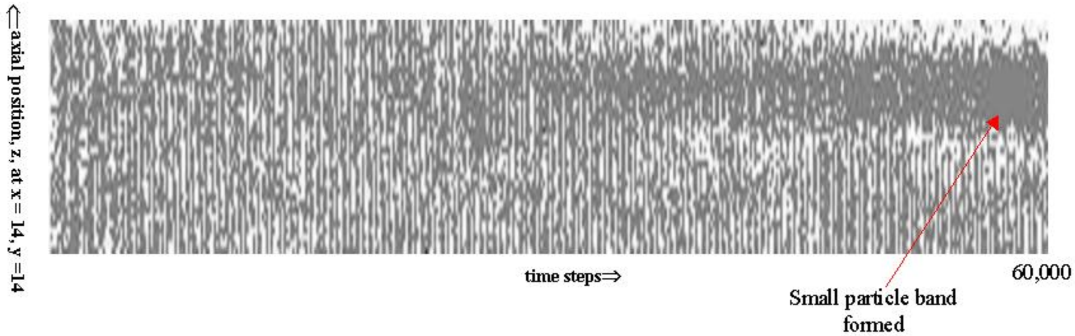

Figure 4.9: CA simulation, larger particles with a much greater friction coefficient than small particles eventually form an axial band.

These results indicate that the exchange of particles between layers may accelerate the process of axial segregation and later band coarsening. At 10000 time steps the original configuration, with no mixing between layers, has two distinct bands and a third and forth which are in the process of merging. When the topmost three layers are allowed to exchange particles and evolved to 10000 time steps there are three distinct bands, any merging which occurred happened before 7000 time steps. When the topmost five layers are allowed to exchange particles and allowed to evolve to 10000 time steps there are only two distinct bands remaining. However, it is not obvious from these data that the three systems formed the same number of bands initially. Still, these results seem to indicate that allowing the layers to mix facilitates band merging in axially segregated systems.

We have shown that a simple CA simulation can produce patterns, mixing and time evolution qualitatively similar to those seen experimentally, when the particles are of two different sizes and their frictional properties are varied. One interesting aspect of our results is that at no time did the radial core of particles disappear. This is consistent with the experimental MRI results of Hill, Caprihan, and Kakalios, [40] as well as with our recent experimental results (see Chapter 7), but other experiments [35, 59] have seen the complete disappearance of the radial core into axial bands. A number of parameters were different between these experiments however, including particle composition, ratio of particle sizes, cylinder sizes, amount of time the system was run for, and rotation rate. One or a combination of these factors could give rise to the difference observed.

It may be interesting to see if allowing particles of different layers near the surface to exchange particles in a system of two different sized particles, as happens in the flowing layer of an experimental system, changes the results of the simulations. Since there is an affect on the rate of band merging in a system of the same size but differing frictional properties, it is probable that allowing the differently sized system to exchange particles will have an affect on how banding develops and proceeds.

In addition, varying particle sizes in the simulation may lead to useful information since experimentally it is only particular size ratios at a given rotation rate that will axially segregate and coarsen. Finally, different ratios of large to small particles could be simulated to see what percentage of small particles is necessary for axial banding to develop. Experimentally, observing and quantifying under what circumstances there is a complete disappearance of the radial core into axial bands, (and if there is any further evolution of the system after this occurs, or if this is the final state of the system) may be important to understanding the phenomenon of axial segregation. Future work will address some of these questions.

Lastly, we note that, in contradiction to *all* experimental findings on radial segregation the authors have been able to find, the radial core was at no time completely below the surface of the top of the flowing layer in these simulations. This raises the question of what is being simulated. Is it really the top of the flowing layer, or is it more accurate to think of it as simulating something below the surface of the flow, which includes the top of the radial core? Or put another way, what is the importance of this simulation shearing part of the radial core at all times with only other small particles, with no layers of larger particles above it as seen in experiments?

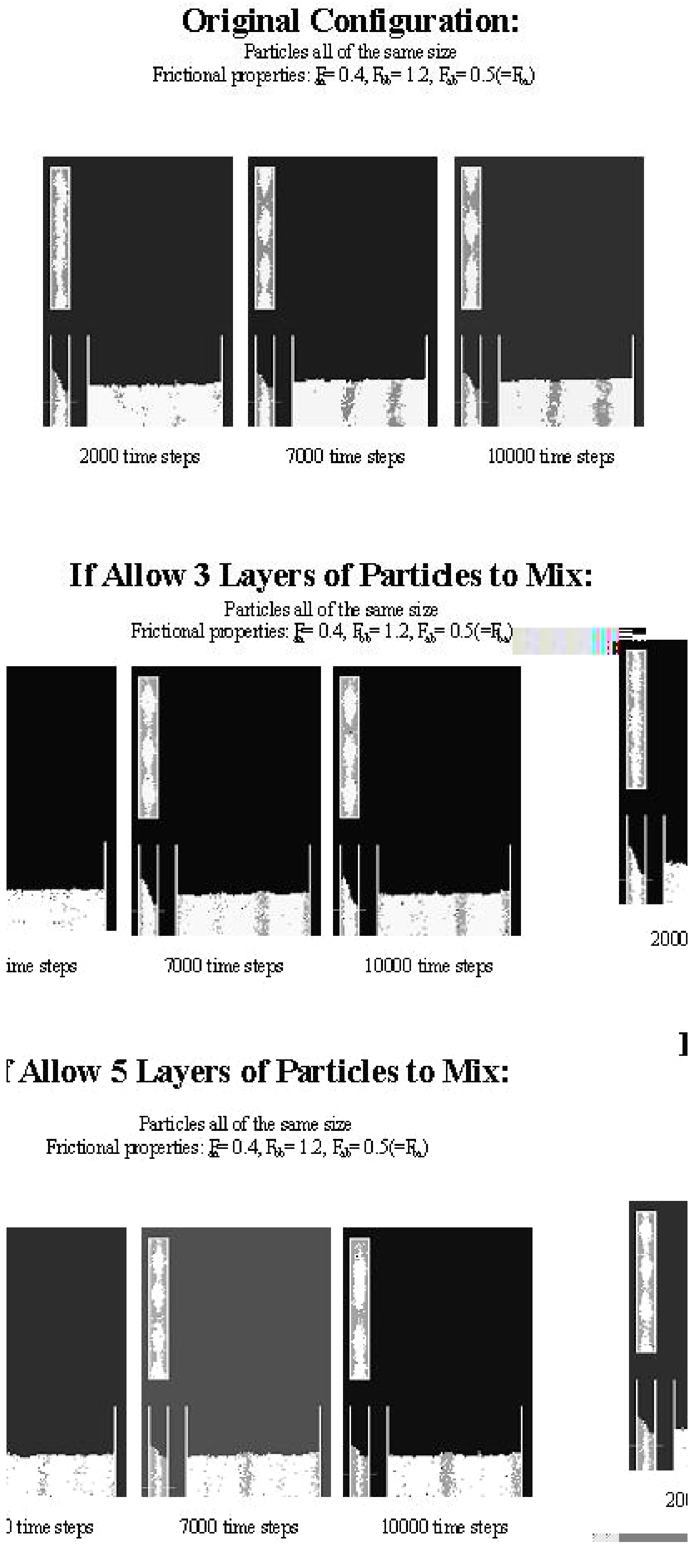

Figure 4.10: Results of CA simulation when layers are permitted to exchange particles.

Chapter 5

Segregation Theories

Theories of granular segregation may be loosely categorized. There are those based on kinetic theory which can in principle be applied to any type of segregation in any geometry. There are those which are applicable to radial segregation in the rotating drum, and also to stratification in inclined plane flows and unmixing in chute flows. And there are those specifically developed to explain axial segregation in the rotating drum geometry. Of particular interest to this thesis are the latter. Perhaps surprisingly, only two types of segregation theories appear in the literature to explain this banding, those that take into account only surface effects, proposed by a number of different researchers, and one which uses a Raleigh-like instability of the core mediated by the inertia of the larger particles. These theories will be discussed below.

The most complete kinetic theory based model for multicomponent mixtures of hard spheres is given in de Haro et al. [9]. Jenkins and Mancini [10] showed that the equations derived by de Haro et al. are valid to first order approximation for slightly inelastic spheres. Using these kinetic theory results (revised Enskog theory) Hsiau and Hunt [11] considered the thermal diffusion of flow of a biparticulate system. They found that a gradient in granular temperature causes smaller particles to concentrate in the region of the flow with a higher granular temperature, which implies larger velocity fluctuations, and which is defined as a quantity proportional to the average kinetic energy of a particle associated with these fluctuations.

However, experiments do not support these results. They show that it is the larger particles which migrate to the top of the layer, where the granular temperature is largest. Analogous behavior is also observed in the rotating drum geometry, with the smaller particles migrating toward the center of the drum, whereas the larger particles migrate to the top of the layer, where again the granular temperature is assumed highest due to the system having the highest velocity at this location. These results are also the reverse of the predictions given by Savage and Lun's [38] phenomenological theory of segregation. Savage and Lun were the first to present a detailed model for size segregation due to a percolation mechanism. They used a statistical analysis to argue that in a dense flow it is more likely for small voids to form thus, the smaller particles drop into the voids more often than the large ones, with the result being a net downward flux of smaller particles and net upward flux of larger particles resulting in segregation. These studies were for chute flow, but again the idea is just as applicable for radial segregation in rotating cylinders, where there is a relatively dense lens-shaped active layer and an approximately impenetrable solid-body layer. The small particles can then percolate through the flowing layer more easily than the larger particles and form a core along the axis of the cylinder.

Gravitational effects were not considered in the Hsiau and Hunt [11] study and these can produce pressure gradients, as described below, that can reverse the segregation flux, which may be the reason for the discrepancy between their predictions and the experimental results of [38,60] and others, as well as our experimental results on radial segregation (discussed in Chapter 6).

Further extending the kinetic theory for granular flows Khakhar et. al [61] looked at the mixing and segregation in chute flows. Their aim was to develop simple continuum models for calculating segregation fluxes, beginning with the transport equations for a binary mixture of nearly elastic spheres as presented in Jenkins and Mancini [10]. These results may be applicable in the flowing layer of the rotating cylinder geometry as well.

When considering a binary mixture of spherical particles of masses m_1 and m_2 with radii R_1 and R_2 the mass balance equation is given by,

$$\partial_t \rho_i + \nabla \cdot (\rho_i \mathbf{u}_i) = 0, \qquad i = 1, 2, \tag{5.1}$$

where $\rho_i = n_i m_i$ is the mass density of species i, n_i is the number density of i and u_i is the average velocity of i. The linear momentum balance equation is given by

$$\rho(\partial_t \mathbf{u} + \mathbf{u} \cdot \nabla \mathbf{u}) = \nabla \cdot \mathbf{P} + \rho \mathbf{g}, \tag{5.2}$$

where $\rho = (\rho_1 + \rho_2)$ is the mixture density, $\mathbf{u} = (\rho_1 \mathbf{u}_1 + \rho_2 \mathbf{u}_2)$ is the mass averaged velocity, $\mathbf{P}$ is the stress and $\mathbf{g}$ the acceleration due to gravity. The stress is written as $\mathbf{P} = -p\mathbf{I} - \tau$, where the granular pressure (p) is the isotropic part, and the deviatoric part, τ, depends on the local velocity gradient. Finally, the energy balance equation in terms of the granular temperature (T) is given by

$$n(\partial_t T + \mathbf{u} \cdot \nabla T) = T\nabla \cdot \mathbf{J}_t - \nabla \cdot \mathbf{q} + \mathbf{P} : \nabla \mathbf{u} + (m_1 + m_2)\mathbf{J}_t \cdot \mathbf{g}\gamma. \tag{5.3}$$

In equation 5.3, the granular temperature is defined as $T = (n_1 T_1 + n_2 T_2)/n$, where $n = (n_1 + n_2)$ is the total number density, and again, $T_i = m_i < C_i^2 > /3$ is the granular temperature of species i, $C_i = |\mathbf{c}_i - \mathbf{u}_i|$ is the magnitude of the fluctuation of the velocity of a particle of species i, $\mathbf{c}_i$ is the velocity of a particle of species i, $\mathbf{u}_i$ is the average velocity of species i, and the brackets $< ... >$ denote a local volume average. The symbol : denotes the contraction of the tensor $\mathbf{P}$ and $\nabla \mathbf{u}$. The first term on the right side of Eq. (5.3) is the energy transferred by diffusion, where $\mathbf{J}_t$ is the total diffusion flux on a number basis. The second term corresponds to energy transfer by conduction, the third term to viscous dissipation, the fourth term to the rate of work done by gravity forces due to a net diffusion flux. γ is the rate of dissipation of energy due to collisions. Use of these equations requires constitutive relations for the stress, energy flux, energy dissipation due to inelastic collisions and diffusion velocities. Expressions for these for the general case are given in Jenkins and Mancini [10]. They assume that diffusion may occur due to three independent causes [62]: ordinary diffusion caused by number fraction gradients, temperature diffusion due to gradients in the granular temperature, and pressure diffusion caused by pressure gradients. Ordinary diffusion always results in mixing, whereas pressure and temperature diffusion may produce segregation if there exist density and/or size differences. Khakhar et al. [61]apply the results of [10] and derive expressions for the different diffusion fluxes from the kinetic theory for binary mixtures. They present results for two particular cases, elastic particles in a gravitational field and inelastic particles in a chute flow. Furthermore, they consider both no friction and frictional particles for the inelastic particles in a chute flow. They find that for the case of different sized particles the segregation depends on both the temperature and pressure fluxes.

However, the kinetic theory breaks down for deviations from the assumption of nearly elastic collisions and for dense flows, with the computed granular temperature being much lower than that necessary to fit to particle dynamic (PD) simulation data. In PD simulations friction and collisions result in a highly dissipative system. When the granular temperature is used as a fitting parameter, results from PD and the theory are similar. The theory predicts that in the low density limit small particles will migrate to the top of the layer, whereas for dense flow the smaller particles will migrate to the lower level of the flow. This theory is, therefore, the first that is able to account for the experimental results of Nityanand et al. [63] who observed a reversal in the typical radial segregation pattern at high rotation speeds, with the larger particles forming the inner core. This can now be explained by kinetic theory as an example of what happens in a binary system of mixed sized particles in the low volume fraction limit.

The "BCRE" theory of segregation was first developed for sandpiles by Bouchard et al. [64] and more fully developed in [65–67]. Chakraborty et al. [68] have expanded and modified the theory to describe the radial segregation of multiparticulate systems seen in the rotating cylinder geometry with particles of different sizes. They assume a sharp interface between the active and passive regions in the rotating cylinder, where collisions between rolling and immobile grains occur at the interface, which lead to the exchange of grains between the two regions. Four things are identified by Boutreux and deGenne [65] as possible outcomes of a collision between two particles: *amplification, capture, exchange,* and *recoil*. Amplification of species α refers to the event of an α-type immobile grain being dislodged into the flowing layer by a rolling grain. This could happen by auto-amplification, when the colliding grain is also of type α, or by cross-amplification, when it is of type β. Capture of a grain of species α occurs when it is absorbed by the passive layer. They proceed to define the simplest form of the rate of capture of α-type grain then as,

$$\Gamma_\alpha = \gamma^a_{\alpha\alpha}\frac{v}{d_p}R_\alpha\phi_\alpha g^a(\psi) + \gamma^a_{\alpha\beta}\frac{v}{d_p}R_\beta\phi_\alpha g^a(\psi) - \gamma^c_\alpha\frac{v}{d_p}R_\alpha\phi_\alpha g^c(\psi), \tag{5.4}$$

where the average collision frequency f varies as $\frac{v}{d_p}$ and d_p is the average grain diameter. R_i is the number of α or β type rolling grains in the active layer per unit length of the interface. The coefficients $\gamma^a_{\alpha\alpha}$, $\gamma^a_{\alpha\beta}$, γ^c_α are constants of order unity and depend on the properties of the grains, and $g^a(\psi)$ and $g^c(\psi)$ are functions of the slope at the interface. To complete the formulation the functional forms of $g^a(\psi)$ and $g^c(\psi)$ are specified as:

$$g^a(\psi) = \frac{Aexp(B\psi)}{1 + exp(B\psi)} \tag{5.5}$$

$$g^c(\psi) = \frac{A}{1 + exp(B\psi)}. \tag{5.6}$$

With appropriate boundary conditions Chakraborty et al. [68] test their model on three different systems: grains differing only in surface properties, grains differing slightly in size, and grains differing widely in size. The model yields results qualitatively similar to those of experiments for the first two cases, and when a term to mimic the screening that occurs due to the "kinematic sieving" of the small particles through the large ones in the flowing layer, the model also works well for the case of grains differing widely in size. They note that the prediction of symmetric profiles of the species concentrations in the active and passive layers are only for particular cases of grain properties and not universally applicable. They propose that the assumption of a sharp interface between active and passive layers is the reason for this inconsistency in the model. Experiments have more recently verified that there is a "creep" motion between active and passive layers in a pile flow and that there is no sharp boundary [69]. This model, therefore, proposes that the exchange of grains at the interface between the active and passive layers in the rotating cylinder is the cause of radial segregation in a two-dimensional biparticulate system. As presented in Chapter 6, our studies of a radially segregated system show the bottom of the flowing layer to always occur well within the radially segregated core, i.e. there are at least a few layers of small particles, at all rotation rates studied, below the bottom of the flowing layer before a layer of large particles is encountered. Therefore, at the interface between the flowing region and solid body region there are only small particles below and above, hence small particles are only interacting with other small particles at this location. It appears unlikely then that this mechanism is a major contributing factor to radial segregation. It is however possible that this theory could be modified to account for *axial* segregation.

The previously discussed theory of "percolation" or "dynamic sieving" of small particles first presented by Savage and Lun [38] is now generally accepted as the explanation of size segregation in a variety of systems when the stratification is in the radial direction.

A continuum description has been proposed for the axial segregation observed in long rotated cylinders by Zik et al. [39]. Presented is a simple theory of segregation in thin surface flows driven by local slope differences. For a binary mixture the model yields a nonlinear diffusion equation for the relative concentration of particle type along the axis. Axial segregation occurs when the diffusion coefficient turns negative. This model can explain axial segregation and later band coarsening, however it fails to describe the transient traveling wave state which precedes axial segregation in some mixtures [42] and fails to consider bulk effects.

Aranson and Tsimring [12, 43] present another continuum model for axial segregation which can account for both the early traveling wave state as well as the later axial banding and coarsening for the axial segregation of granular materials in a long rotating drum. The model operates with two local variables, the concentration difference and the dynamic angle of repose. The following equation represents conservation of the relative concentration c in the binary mixture,

$$\partial_t c = -\partial_x[-D(c)\partial_x c + g(c)\partial_x \Theta]. \tag{5.7}$$

The first term describes the diffusion flux and the second term describes differential flux of grains due to the gradient of dynamic angle of repose. A and B are defined as two particle types differing by static angle of repose, with A having the larger angle, Θ is the local dynamic repose angle, $c = (c_A - c_B)/ < c >$ is the local concentration of particles with $< c > = < c_A + c_B >$ the average concentration over the whole system. D, g are transport coefficients and in general depend on the relative concentration, c.

Aranson and Tsimring go on to derive the coefficients from the equation for granular transport in the bulk and surface layer. The flux balance calculation [43] yields,

$$D(c) = D_0(1 - \eta c), \tag{5.8}$$

and

$$g(c) = G_0(1 - c^2), \tag{5.9}$$

the latter was first derived in Ref. [39]. The constants η and G_0 depend on the physical properties of the grains. Therefore in this model the particles with the larger static repose angle are driven towards the greater dynamic repose angle. This differential flux gives rise to a segregation instability. It further provides a natural saturation mechanism for the segregation instability.

The second equation of Aranson and Tsimrings model [12, 43] describes the dynamics of Θ,

$$\partial_t \Theta = \alpha[\Omega - \Theta + f(c)] + D_\Theta \partial_{xx}\Theta + \gamma \partial_{xx} c. \tag{5.10}$$

Here Ω is the angular velocity of the rotating drum and $f(c)$ is the static angle of repose which depends on the relative concentration. α establishes the time scale for the axial segregation. The term $D_\Theta \partial_{xx}\Theta$ describes axial diffusion relaxation. The last term represents the lowest-order nonlocal contribution from the inhomogeneous distribution of c. This term appears as a result of the interplay between the bulk flow and Fick diffusion. Furthermore, it is this term which gives rise to the transient oscillatory dynamics of the binary mixture. These results are consistent with the transient wave state seen by Choo et al. [42]. Finally, this model also describes logarithmic coarsening of the quasi-static banded structure. Aranson and Tsimring point out that such coarsening is typical for one-dimensional systems with exponentially weak attractive interaction among defects or interfaces, as in the phase-ordering kinetics described by the Cahn-Hilliard model [70].

Khan et al. [44] point out that the comprehensive model of axial segregation proposed by Aranson and Tsimring, as described above, has the crucial feature of two essentially diffusive fields, the surface concentration and the dynamic angle of repose, coupled such that they oscillate $\pi/2$ out of phase during the initial transient wave state of the segregation process. They are in phase at later times. They go on to point out that similar phase evolution is likely to be generic for models containing oscillatory behavior regardless of how the order parameters are defined. Khan et al. [44] find experimentally, using surface images of the time evolution of a segregating biparticulate system in a long rotating drum, that the surface concentration and the dynamic angle of repose are in phase with each other at all times, in disagreement with the model of Aranson and Tsimring as presented in [12, 43] and summarized above. Khan et al. additionally determined the phase relationship between the projected concentration of the subsurface core, the surface concentration, and the dynamic angle of repose. They find all three quantities to be in phase with each other, eliminating also the particle concentration within the subsurface core as the conjugate parameter to the surface concentration. These experimental results "place severe constraints on the mechanism of axial segregation." [44] Needed is a dimensionless field which oscillates $\pi/2$ out of phase with the surface concentration during the initial traveling wave transient, and in phase at later times, during axial band formation and coarsening.

Puri and Hayakawa [71] developed a theory within which they have attempted to formulate coarse-grained or phenomenological models which capture universal features of granular materials. They provide a dynamical basis for an "effective surface tension" between domains enriched in different components of the mixture. This "effective surface tension" penalizes sharp interfaces between regions enriched in different components of the mixture. Beginning with the steady state slope profile as determined by Zik et al. [39], they then obtain the friction coefficient and fluid viscosity which depend on the order parameter $\Psi(r,t)$ such that $\phi_s = (1+\Psi)/2$ and $\phi_g = (1-\Psi)/2$, where ϕ_s and $\phi_g(= 1-\phi_s)$ are the appropriate number fractions of sand (rough) and glass (smooth) particles. Similar to Aranson and Tsimring above, their model considers the coupled dynamics of the composition field and local slope field. However Puri and Hayakawa [71] additionally assume that the local slope is in instantaneous equilibrium with the local composition. This allows a simplification of the model to a single dynamical equation for the composition. They obtained both analytic and numerical results and found them to be in good agreement with qualitative experimental results, including the radially segregated state, the axially segregated state, and band coarsening. However, at present this model cannot account for the transient traveling wave state [42]. Additionally, the specific quantitative predictions they make, e.g. that the band size is expected to grow logarithmically in the banding regime, await experimental verification.

Alexander et al. [54] also present a theory of axial segregation in the rotating drum geometry. To the author's knowledge this is the only theory of banding segregation that takes into account subsurface effects. First, they experimentally determine the relationship between banding, mean particle diameter, cylinder diameter and rotation rate. The trends they found were most easily described by defining a quantity,

$$\delta = D/d_{avg}, \tag{5.11}$$

where D is the cylinder diameter and d_{avg} is the mean particle diameter. For δ greater than 55 they found banding to always occur, for δ less than 40 they found that banding never occurs, and for δ between these two values they found a reversible axial segregation with the presence of banding depending on the cylinder rotation rate. Alexander et al. point out that these cut-offs are more than likely particle-property dependent and therefore not universal, but that the trend is likely to be consistent. They also investigated the extent to which the instability is dominated by large particle versus small particle dynamics. Banding is observed to be suppressed when the large particle concentration is increased from 50 percent to 70 percent. They also found that banding is enhanced when the density of the large particles is increased by 20 percent over that of the smaller particles.

They conclude that the available evidence supports the proposition that axial banding is the overt expression of an underlying transverse Rayleigh-like instability in the radially segregated core, formed during granular tumbling. They believe their experimental results suggest that the instability is mediated by the inertia of the larger species. First, axial bands only appear when δ is large. As δ grows each particle undergoes more collisions while in the flowing cascade, and thus the number of opportunities for inertia-dominated deformation of the core could be expected to increase with δ. Second, non-banding mixtures tend to band at higher rotation rates which is associated with greater momentum transfer during collisions. Additionally, banding is facilitated by making the large particles denser.

Alexander et al. then theorize that axial banding forms due to small bulges at the core interface becoming stretched by the acceleration imposed by the observation (made in a "double-cone-blender" [72]) that large particles outside a core of small particles flow faster than small particles inside the core, each time they visit the cascading surface. As the bulges are stretched, material comes from nearby regions of the core so that the core volume remains constant and the bulges begin to grow. In this way, accompanying each bulge is a nearby valley, and the cascading flow stretches both bulges and valleys around the circumference of the core to produce the observed bands. Experimentally, the growth of bands is limited by dispersion, so that when the rate of growth of bulges exceeds the rate of dispersion, then the bulges can grow until they emerge at the surface as bands. This theory will be discussed further in reference to our experimental results of axial segregation in Chapter 7.

Chapter 6

Experimental Studies of Radial Segregation

As was mentioned in the Introduction, it is well known that when a monoparticulate granular system is rotated in a horizontal cylinder the depth of the flowing (active) layer of particles depends on the rotation rate of the system [6, 20, 22, 29, 73, 74]. As the rotation rate is increased the flowing layer becomes deeper, although there remains some disagreement about the specifics of this dependence [6,20,22,73]. Also, when a biparticulate granular system composed of particles of two different sizes is rotated in a half-filled horizontal cylinder it has a tendency to segregate, with the smaller particles forming an inner core [34, 39, 60, 75] Furthermore, if the system is 3D and it is allowed to evolve, axial segregation may develop and coarsen along the length of the cylinder [15, 21, 40].

In recent investigations variations were observed between the velocity depth profiles of pure and segregating systems in half-filled rotating cylinders [50]. However, this research was primarily focused on determining differences between axially segregating and non-axially segregating biparticulate systems and mentioned but did not discuss further the qualitative differences that they observed between a pure large particle system and a radially segregating system. We wanted to investigate further differences between radially segregating and pure systems of particles.

Therefore, we here restrict ourselves to the study of a 3D biparticulate system that segregates only radially, with no evidence of axial segregation either at or below the surface even after hours of rotation. We compare the location and shape of the core of smaller particles, as well as the location of the bottom of the flowing layer, at various rotation rates. We also compare the velocity depth profile of the radially segregated system with that of pure bead systems and provide an explanation for the observed differences. Although there is a generally accepted explanation for the radial segregation phenomenon, that of a dynamic sieving process [38], these investigations may still help clarify what is occurring within a radially segregating system of particles, and may also help identify mechanisms which influence the development of axial segregation. This connection will be discussed further in Chapter 7.

A 7.0 cm inner diameter, 6.0 cm long acrylic cylinder was half-filled with an approximately uniform biparticulate mixture of 4mm diameter cellulose acetate beads (not NMR sensitive) and 2mm diameter pharmaceutical beads (containing NMR sensitive liquid). Thus, only the 2mm beads appear in the MRI images. In order to obtain a relatively thick core, the ratio of small to large particles was chosen to be one-to-one by unmixed volume. This biparticulate system is known to radially, but to not axially, segregate [50]. This behavior was verified for our system both at and below the surface, following several hours of cylinder rotation at all rotation rates investigated.

We used MRI as described in Chapter 2, to acquire time-averaged density images of the distributions of the particles at the axial center of the 3D cylinder. Each image was made up of 24 averages and a slice thickness of 5mm. Accordingly, in the intensity images of Fig. 6.1 it is not that there are more particles in the image at the highest rotation rates; rather the core becomes less distinct at these higher rotation rates, with smaller particles spending some time outside of what can be obviously termed the core and larger particles spending some time within the core.

We then used MRI velocimetry, as described in Chapter 2, to obtain velocity profiles at the axial center of the 3D cylinder for this system of particles. Again, a slice thickness of 5mm was used and 24 averages were taken for each image. The two data sets of velocity components, that are orthogonal in the laboratory frame, were then combined to form the component of velocity parallel to the free surface of the flow. The same experiment was repeated at different rotation rates for the same biparticulate system and approximately the same mixed initial conditions.

Velocity profiles were then acquired for a 2mm/4mm biparticulate system, again in a one-to-one ratio, in which all particles were NMR sensitive, as well as for a pure 2mm system and a pure 4mm system.

We also investigated if we could produce the radial "fingering" pattern, observed no discernible difference in the position of the center of the core between 10 and 30 rpm (in the rolling regime). Fig. 6.2.

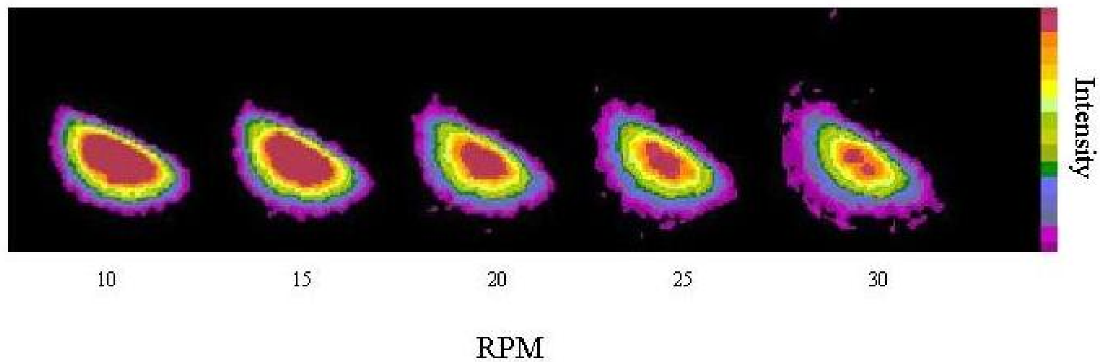

Figure 6.1: Radial core of 2mm particles at various rotation rates. Time averaged MRI density images. All intensities over 7000 (arbitrary units) are colored dark red.

We also see that the top of the core, again measured at the central perpendicular bisector to the free surface, remains in approximately the same position (Fig. 6.2)). At the highest rotation rates, fluctuations prevented consistent identification of the location of the bottom of the core, so no meaningful comparison could be made of the location of the bottom of the core at different rotation rates. This effect will be discussed further in the "Distinctiveness of Core" section below.

II. Shape of the Core

The shape of the core was not found to be circular or oval at the center of the cylinder. Instead the top of the core forms an almost flat surface that is parallel to the free surface. The core may best be described as forming a half-circle, mimicking the way the overall system behaves, with its own flat surface, flowing layer depth, and bottom (Fig. 6.1). This shape has been previously observed in stationary systems, but never away from the endwalls within the bulk of a flowing system. The MRI intensity

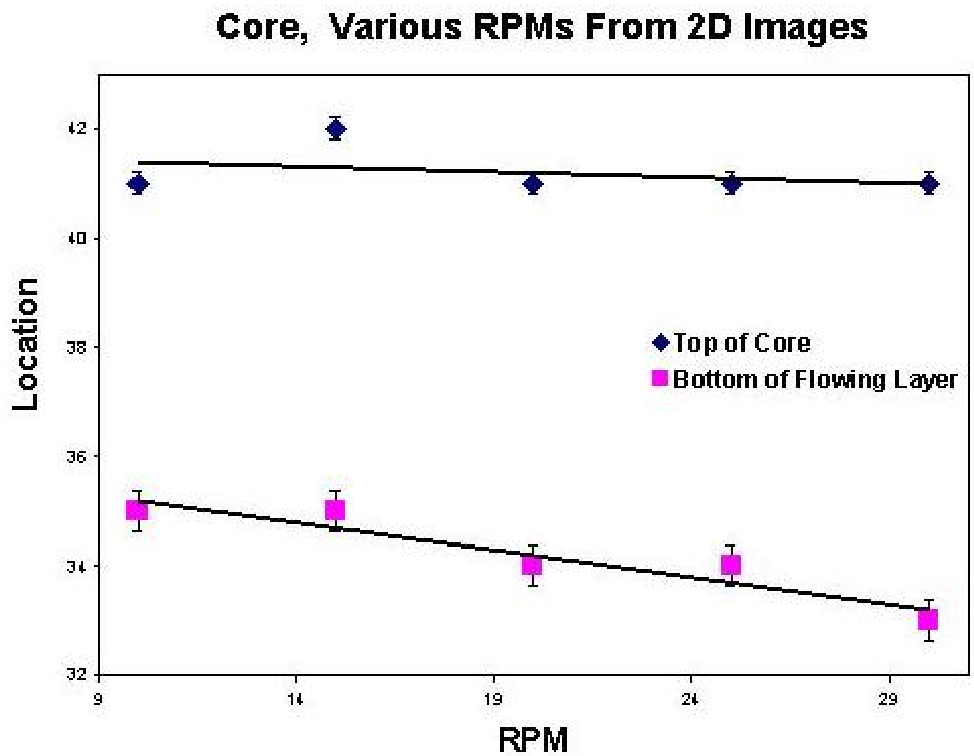

Figure 6.2: Plot of the change in position of the bottom of the flowing layer and the top of the core with increasing rotation rate, in a radially segregated biparticulate system.

images of Fig. 6.1 also show that at low rpm the core is symmetric about the central perpendicular bisector to the free surface, but as the rotation rate is increased the core becomes less smooth and less symmetric.

III. Distinctiveness of Core

As the rotation rate increases, the core becomes less distinct. This can be most clearly seen in the MRI intensity images of Fig. 6.1. Recall that these are time-averaged density images. In Fig. 6.1 the darkest red areas contain the highest pixel intensities seen at 30 rpm. The changes in intensity with rotation rate, then, indicate that the small particles within the core are diluted more by the larger particles at higher rotation rates, and it becomes more difficult to identify the core boundaries. This phenomenon is distinct from undulations of the core, which may develop into axial segregation [40].

Furthermore, there is a 15 percent loss of total intensity observed at the axial center of the cylinder between the images taken at 10rpm and those taken at 30rpm. The core retains the same thickness along the axis at a given rotation rate, therefore the loss of intensity is not due to undulations of the core. This lends support to the idea that rotation at higher rpm results in greater movement of the smaller particles, with the result that they are more likely to be averaged out of the images. It is possible that this greater mobility may encourage axial transport.

IV. Location of Bottom of Flowing Layer

Consistent with results for monoparticulate systems, the depth of the flowing layer in our system increases with rotation rate (Fig. 6.2). As expected, but not confirmed until now, the bottom of the flowing layer lies within the radial core at all rotation rates. This can be clearly seen in Fig. 6.3, which shows MRI velocity images of the core at various rotation rates. The bottom of the flowing layer is the dark red lens shaped line in each image. In addition, we found that small particle mass was conserved across the perpendicular bisector within the core, i.e. the same amount of small particle mass moved across the perpendicular bisector of the free surface to the left as to the right in time t. Finally, our results demonstrate that, except where the core becomes indistinct at high rotation rates, the velocity depth profile in the core is linear in the solid body region and quadratic in the lens shaped flowing region, in agreement with results obtained for monoparticulate systems [35, 77].

The small variations of the core between the MRI intensity images 6.1 and MRI velocity images 6.3 are due to thresholding differences. In particular, much of the "dispersion" of the radial core at high rotation rates is lost in the processing of the

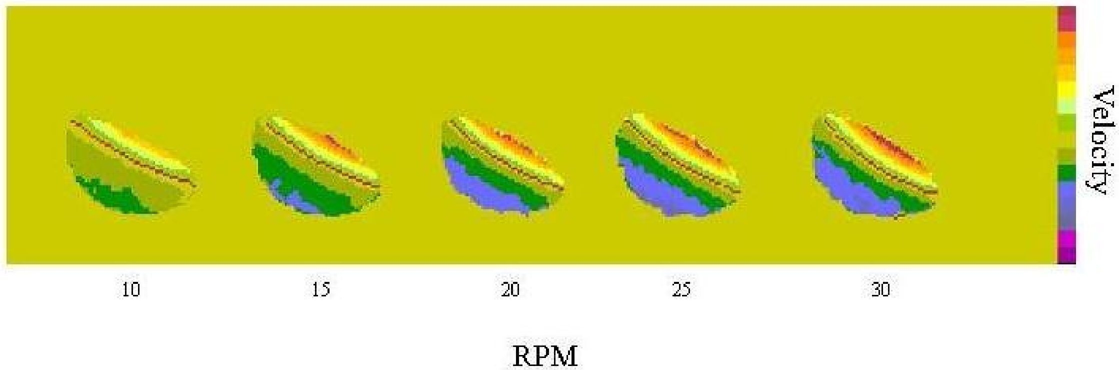

Figure 6.3: MRI velocity images of bottom of flowing layer at various rotation rates. Bottom of flowing layer is located within the core region at all rotation rates studies.

velocity images.

V. 55 Percent Full Cylinder, "Finger" Pattern in 3D Drum

Recent experiments [76] used 2D cylinders to study various filling fractions with a 50/50 by volume mixture of large and small particles. These experiments found that the pattern of the radial core differed from what has traditionally been reported with 50 percent or less full cylinders. These patterns occur only in a small range of fill levels (∼55-60 percent full). Under certain conditions, defects in the radial core of smaller particles grow into radial stripes that extend toward the outer walls of the drum in a manner somewhat reminiscent of viscous fingering (see example, Fig. 6.4). The patterns are strongly dependent on both the fill level and rotation speed of the drum. The authors in [76] argue that these observations can be explained by two spatially disjoint mechanisms: (1) a wave-breaking mechanism that promotes the growth of the stripes and (2) a filtering mechanism that limits the growth of stripes. We wanted to see if these patterns would also be observed in 3D.

For this study, A 7.0 cm inner diameter 6.0 cm long cylinder was filled to a 55

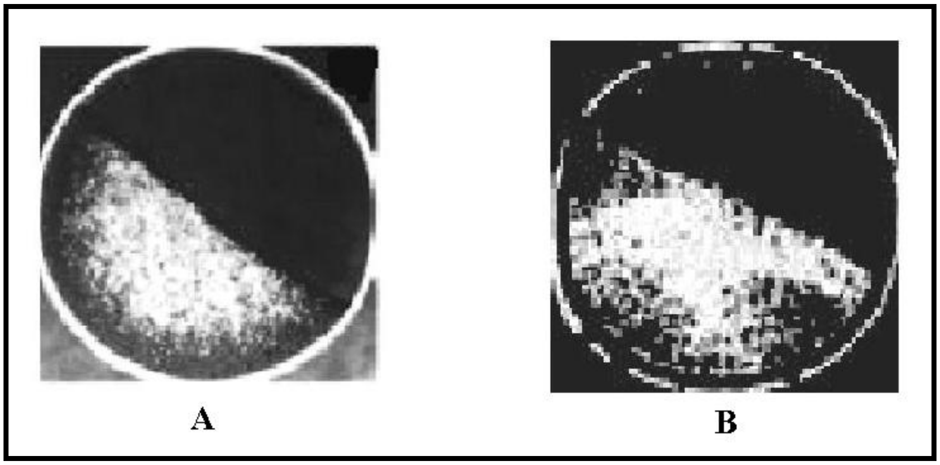

Figure 6.4: Examples of typical radial segregation pattern at A) 50 percent fill level and B) radial fingering of same combination of particle types at a 55 percent fill level.

percent fill level with a well-mixed 50/50 by volume mixture of 1mm NMR sensitive pharmaceutical beads and 2mm non-NMR sensitive cellulose acetate beads. The cylinder was then rotated at 15 RPM. After the desired period of rotation was complete the rotation was stopped and a 3D MRI image of the cylinder was taken. We had not expected this system of particles to axially segregate and were only concerned with reproducing the radial core "fingering" pattern in 3D. Therefore, we have included this study in our experiments on radial segregation Chapter even though it was observed to axially as well as radially segregate.

Radial fingers extending from the core of small particles in a biparticulate system were observed in our 3D cylinder. Details of these features can be seen in Figure 6.5. Images show the time evolution of the 3D system. The top horizontal line of images tracks the changes at the axial center of the cylinder. It can be seen that as the radial core develops, "fingers" are present. In this system an initial axial band forms at the center of the cylinder and the pattern can no longer be seen at this location since it quickly becomes approximately 100 percent small particles. However, as the axial band migrates to an endwall, the radial finger pattern can again be observed

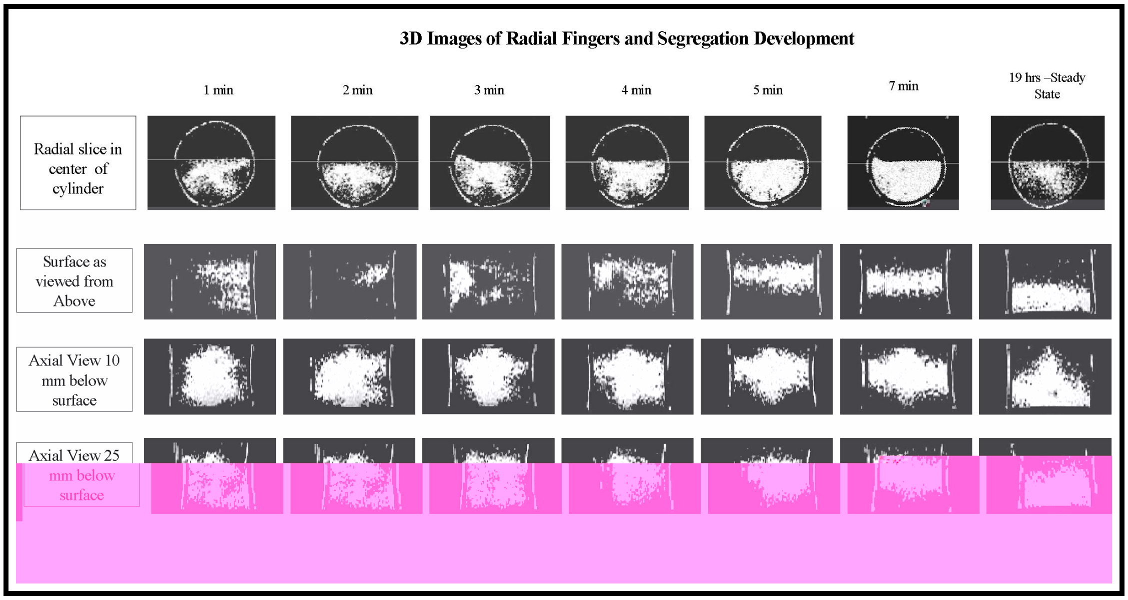

Figure 6.5: 3D radial finger pattern with axial banding segregation.

in the center of the cylinder. We also find that regardless of where the axial band is located, "fingers" are seen wherever a large and small particle band meet. The lower three sets of images in Fig. 6.5 show the time evolution at three different depths of the flow: at the surface of the flow, at 10mm below the top of the flow, and close to the bottom of the cylinder at 25mm below the surface of the flow. We find that even when axially segregated the radial finger pattern remains wherever the radial core is contained within a large particle band. These features of segregating granular mixtures would be difficult if not impossible to observe using methods other then MRI, again reinforcing the usefulness of MRI as a tool to study granular flows.

VI. Comparison of Pure and Radially Segregated System 15rpm

When a comparison was made between the velocity depth profiles of a 2mm/ 4mm radially segregated biparticulate system (all particles NMR sensitive) and pure 2mm and pure 4mm systems rotated at the same rotation rate of 15 rpm, we found interesting differences (Fig. 6.6). Note that the plots have been truncated to focus attention on the flowing layer, and that the bottom of the cylinder would be located at position 0.0 cm if it were included. The velocity depth profiles, along the central perpendicular bisector of the free surface, of the radially segregated system and the pure small particle system are the same in the solid body layer and within the core (where there are only or mostly small particles). The pure 4mm system deviates from this, as expected. It has a deeper flowing layer, as well as following a different course from either the 2mm pure system or the radially segregated system at all depths above the bottom of the flowing layer. It additionally has the slowest free surface velocity as it must for mass flux conservation.

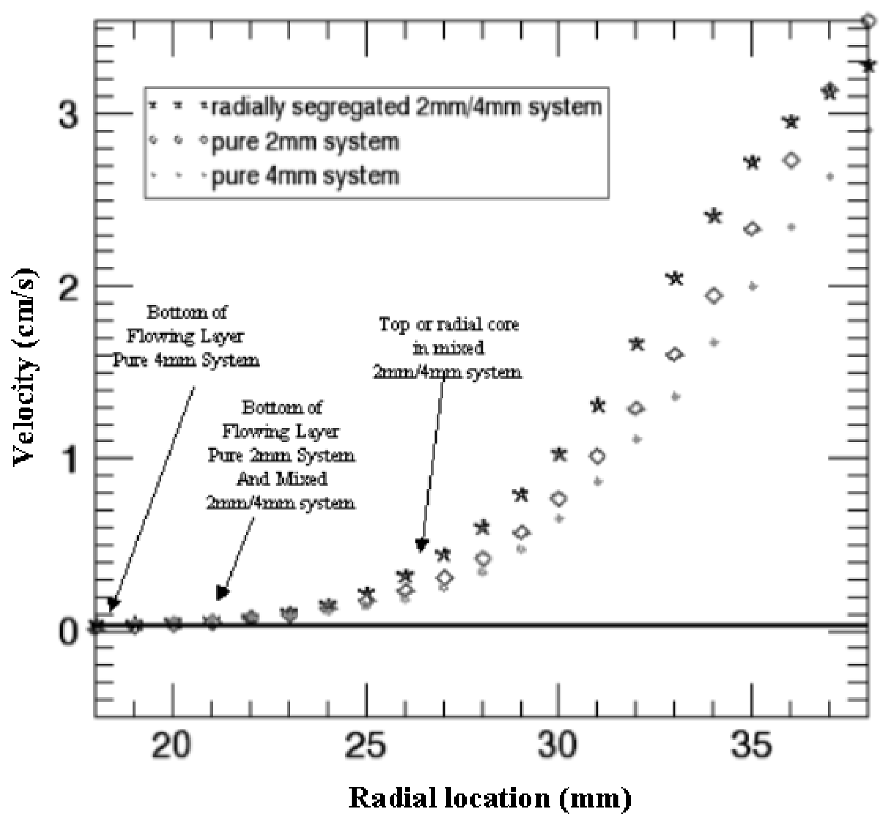

Figure 6.6: Velocity depth profiles radially segregated system and pure particle systems.

Above the core in the segregated system the velocity increases more quickly than the velocity of the pure 2mm system and, therefore, the segregated system has a higher shear rate than either of the pure particle systems at these radial locations. The radially segregated systems continues to have a higher shear rate than the pure 2mm system for 2 to 3 large particle diameters above the small particle core and then the shear rate falls off rapidly as it approaches the free surface, crossing the velocity profile of the pure 2mm system and at the free surface having a velocity lower than that of the pure small particle system.

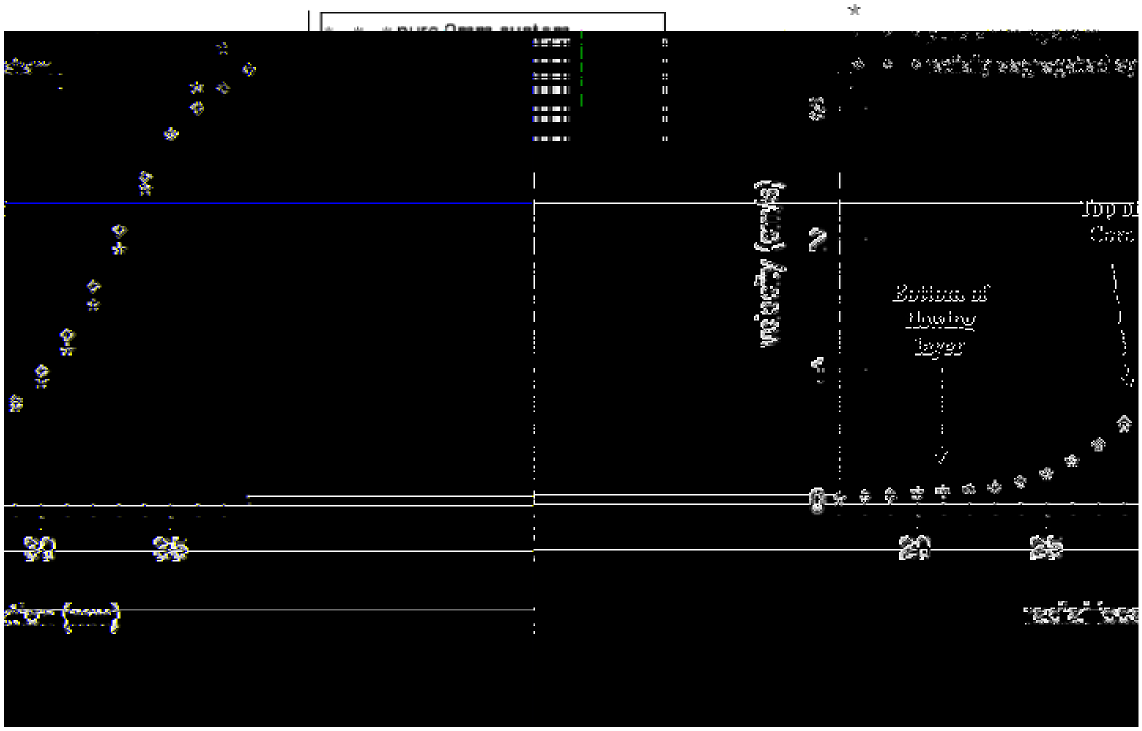

Figure 6.7: Velocity depth profiles of radially segregated system and pure small particle system.

The increase in velocity above the radial core may be expected, since larger particles can move faster over a layer of small particles than it will over a layer of large particles and also faster than small particles will move over other small particles. This was observed in a "double-cone-blender" [54] but never before in the rotating cylinder geometry. Somewhat above this first layer it is reasonable to assume that the large particles continue to move faster than if it were in a pure system. As the layers get further away from the radial core, the small particle core no longer affects the large particles and the shear decreases until the velocity falls below that of the pure 2mm system. This is consistent with mass conservation of the particles across the perpendicular bisector.

Discussion

Our results show that increasing rotation rate influences the shape and distinctiveness of the core of radially segregated smaller particles, although the center remains in approximately the same location. This may be important for understanding the evolution of axially segregating systems, i.e. it may help explain why increasing the rotation rate of some biparticulate systems encourages axial segregation, since doing so makes the core less distinct and may facilitate axial movement of the smaller particles.

Another variable of interest is the ratio of small to large particles in the system. It is possible that with fewer small particles the core will move radially, i.e. change its depth, with changes in rotation rate. It would be useful to experimentally verify this in the future.

We also found that the location of the bottom of the flowing layer of this system behaves in a qualitatively similar manner to that of monoparticulate systems. In both cases the depth of the flowing layer increases with increasing rotation rate. At 15 rpm the small particle system has the same flowing layer depth as the radially segregated biparticulate system, but the present work did not investigate pure systems at other rotation rates for comparison. However, doing so may prove useful in determining if there are quantitative differences between the responses of segregated and monoparticulate systems to increasing rotation rate.

Finally, differences in the velocity depth profiles, along the perpendicular bisector to the free surface, were observed between radially segregated and pure systems of particles. These differences depended on the location of the top of the radial core. Therefore, in a system where the radial core varies in diameter it may be the differences in the shear rate, caused by the differences in velocity at identical radial locations along the axis of the cylinder, that drive a fluctuation to become a band in an axially segregating system. This idea will be discussed further in the next Chapter.

Chapter 7

Experimental Studies of Axial Segregation

7.1 3D Measures of Velocity Field Along Axis

Axial segregation of granular material in the rotating cylinder geometry has yet to be satisfactorily explained. While significant experimental results have been obtained that help clarify some aspects of axial segregation, there is much that remains unresolved, both in regard to what occurs in the system as well as the mechanisms underlying the phenomenon. Furthermore, "it has yet to be established whether there is just a single kind of axial segregation phenomenon, or whether different kinds of granular materials undergo segregation by invoking alternative mechanisms; it is indeed possible that a number of processes operate concurrently, with the dominant one being determined by the prevailing experimental conditions." [78]

The kinetic-theory segregation models of Jenkins and Mancini [10], and Chakraborty et al. [68], discussed in Chapter 5, were developed to explain types of segregation analogous to radial segregation. Although there is no *a priori* reason that a kinetic-theory based model of axial segregation in the rotating drum cannot be developed, to our knowledge this has not yet been attempted. Furthermore, due to these flows having a high density of particles in the rolling regime it is questionable whether or not a kinetic-theory based model would be appropriate.

The phenomenological models presented by Zik et al. [39], Hill and Kakalios [79], and Aranson and Tsimring [12,43], also discussed in Chapter 5, are based on surface variations mediating banding segregation. Zik et al. presented a simplified theory that dealt with the onset of instability produced by local concentration fluctuations, and the response to resulting changes in the angle of repose. They also argued that band formation begins at the endwalls. However, in extensive PD simulations carried out by Rapaport [78], apart from stabilizing the band pattern, they found no evidence to suggest that the end caps alter the axial banding behavior in any way, and since band formation begins almost simultaneously at several distinct locations, the ends do not function as nucleation sites. Further, homogeneity of the cross sectional composition within each band was assumed in the Zik et al. studies, something subsequent MRI results failed to support [40].

Hill and Kakalios [79] also proposed a dynamic angle of repose difference as necessary for the formation of axially segregated bands. They based their conclusion on the observation that at low rotation rates, where there is no difference in the dynamic angle of repose between the constituents of a biparticulate system, axial segregation fails to develop. When the rotation rate is increased however, to a point where there is an observable difference between the angles of repose between the two sizes of particles, axial banding develops. Furthermore, if the rotation rate is decreased in a system which has formed axial bands, to a rate at which the angles of repose are indistinguishable the banding segregation may disappear [79,80].

The continuum model presented by Aranson and Tsimring [12,43] was developed based on one dimensional systems in which the dynamical variables are the local concentration difference and the slope of the free surface. Their model is able to describe the early traveling wave state and subsequent band formation and coarsening.

The cellular automata simulations of Yanagita [14] and Newey [15], and those presented in Chapter 4, are also a simple phenomenological description of axial segregation aimed at mimicking surface effects of multiparticulate granular flow. The results qualitatively reproduce axial segregation and coarsening. However, we have raised the possibility that this is not a true representation of the surface dynamics of a granular flow (in Chapter 4),and it may be more accurately understood as simulating the area directly above the core.

Having introduced these theories, which depend exclusively on surface effects, we must now dispute such theories as being incomplete. None can account for the experimental observation that the radial core may develop stable undulations which never reach the surface of the system [40]. Nor do they explain the recent experimental results of Pohlman et al. [41], which show that even large differences in the dynamic angle of repose between the constituents of a biparticulate system is insufficient to induce segregation. Furthermore, most of these theories are first order in time which is contrary to the experimental results of Choo et al., who show that in some systems there exists a traveling wave state preceding the stable banded pattern, which indicates dynamics which are not merely first order in time. The only theory of this type which adequately addresses the traveling wave state is that of Aranson and Tsimring [12], but important three-dimensional aspects of the problem are absent and, contrary to experiment, the free surface profile is assumed linear. Additionally, the coupled fields in the model were shown to have an inappropriate phase relationship at short times [44].

One reason theories have focused on surface effects is that there is a wealth of information, which is relatively easy to quantify, available from surface experiments. In contrast there are far less experimental data available from the bulk of flowing granular material. This is another reason that MRI experiments are so valuable to granular flow research.

To the author's knowledge, the only theory to have been proposed to explain the axial banding segregation observed in the rotating cylinder geometry that does not rely on surface effects is that by Alexander et al. [54], and which was also introduced in Chapter 5. They used experimental results from the rotating drum, as well as the "double-cone-blender", to formulate a theory of how perturbations in the radially segregated core can be further deformed due to a "stretching" mechanism, whereby larger particles above a core perturbation will accelerate the core boundary and deform it further, bringing in small particles from nearby core areas as the band grows. We will discuss this theory in reference to the experimental results presented below.

In recent experimental work using MRI it was found that the ratio of small to large particles within a slice, for a biparticulate system that axially segregates, influences qualitative features of the velocity depth profile [50]. This difference was not seen for a biparticulate system that does not axially segregate. This indicates that a gradient in the velocity depth profile could be a source of axial transport.

These findings prompted us to investigate if other differences in the velocity depth profile could be observed along the axial length of a 3D cylinder whose biparticulate system has segregated and is now in a steady state and whether a theory for these differences could be simply formulated. Results of experiments carried out over the entire length of a 3D cylinder will be presented and the implications these results have for differences in the velocity depth profile as a mechanism to drive axial segregation will be discussed.

We used MRI velocimetry as presented in Chapter 2 to obtain the velocity field over the entire length of a 7.0 cm inner diameter 7.0 cm long cylinder that has axially

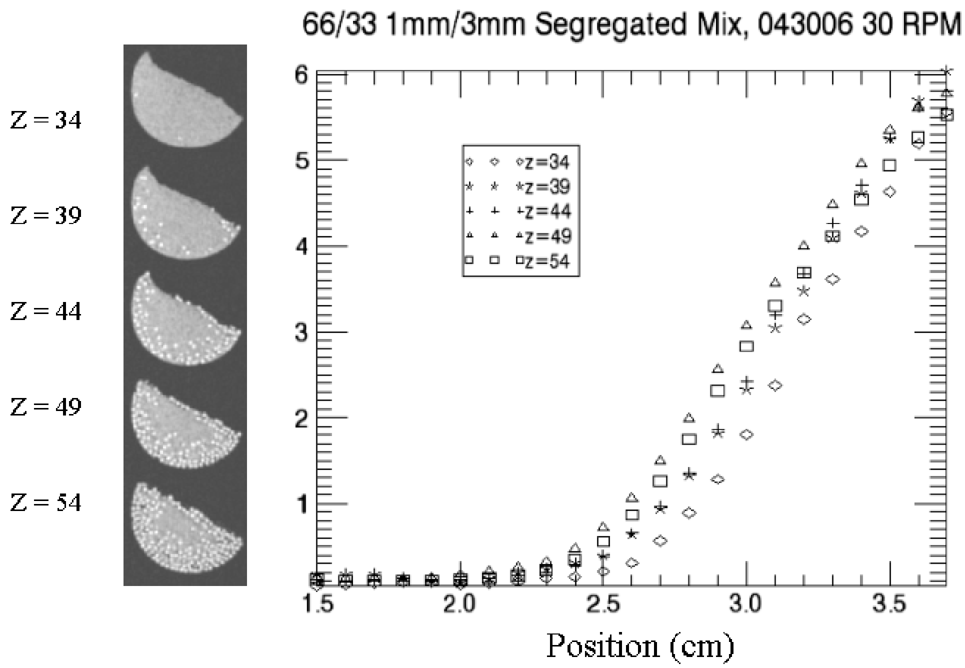

Figure 7.1: Velocity depth profiles along the axis for a system composed of 66 percent small particles.

segregated and is now in a steady state. Typically, one transverse slice at a time is imaged and the cylinder is moved along the axis in order to image additional slices (this was the method used in [50]). We here use the capabilities of MRI velocimetry over the entire 3D cylinder, which allows a continuous view of the velocity depth profile along the cylinder axis. The particles were all NMR sensitive and various ratios of 1 mm to 3 mm diameter particles were used. These imaging experiments were run for approximately 30 min to 1 hour and no difference was observed in the location of the bands before and after the imaging. Therefore the flow was in a steady state, at least over this time scale and with this cylinder length. Plots throughout this Chapter are truncated to focus attention on the flowing layer. For reference note

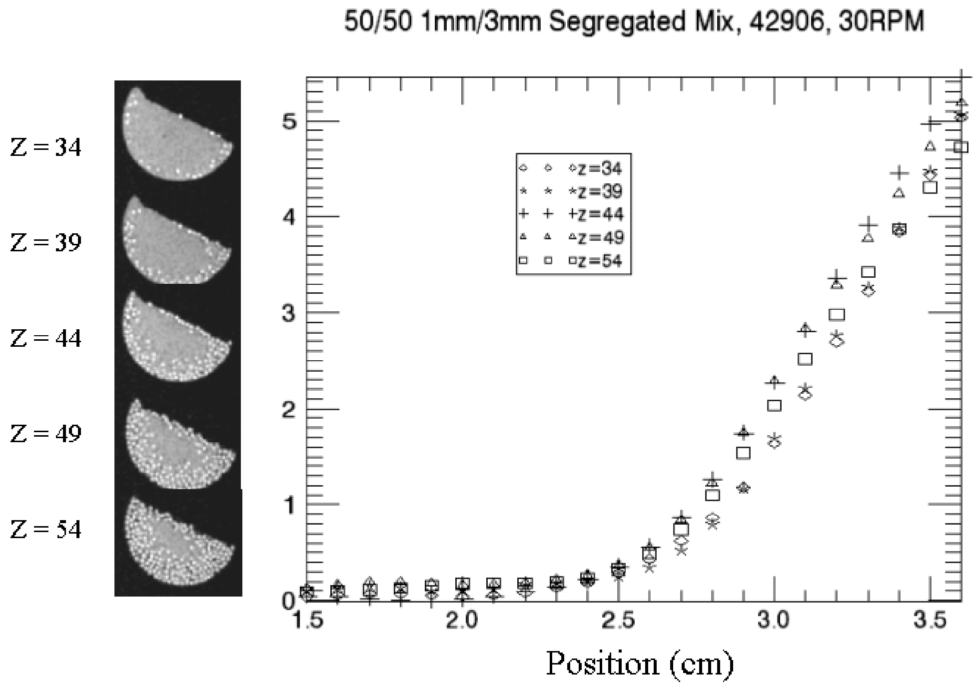

Figure 7.2: Velocity depth profiles along the axis for a system composed of 50 percent small particles.

that the bottom of the cylinder would be located at position 0.0 cm in these plots.

We found that along the length of an axially segregated system differences in the velocity profile measured along the perpendicular bisector of the free surface could be observed (Fig. 7.4). The differences depended on the ratio of large to small particles within a slice. This is consistent with what Maneval et al. [50] observed. No difference was seen in the velocity depth profile along the axis for the pure 1 mm, nor the pure 3 mm systems away from the endwalls. Note that the profile at the axial position z = 54 is close enough to the endwall to be affected by it, but the effect is minimal and confined to the upper portion of the profile [23]. z = 34 is the

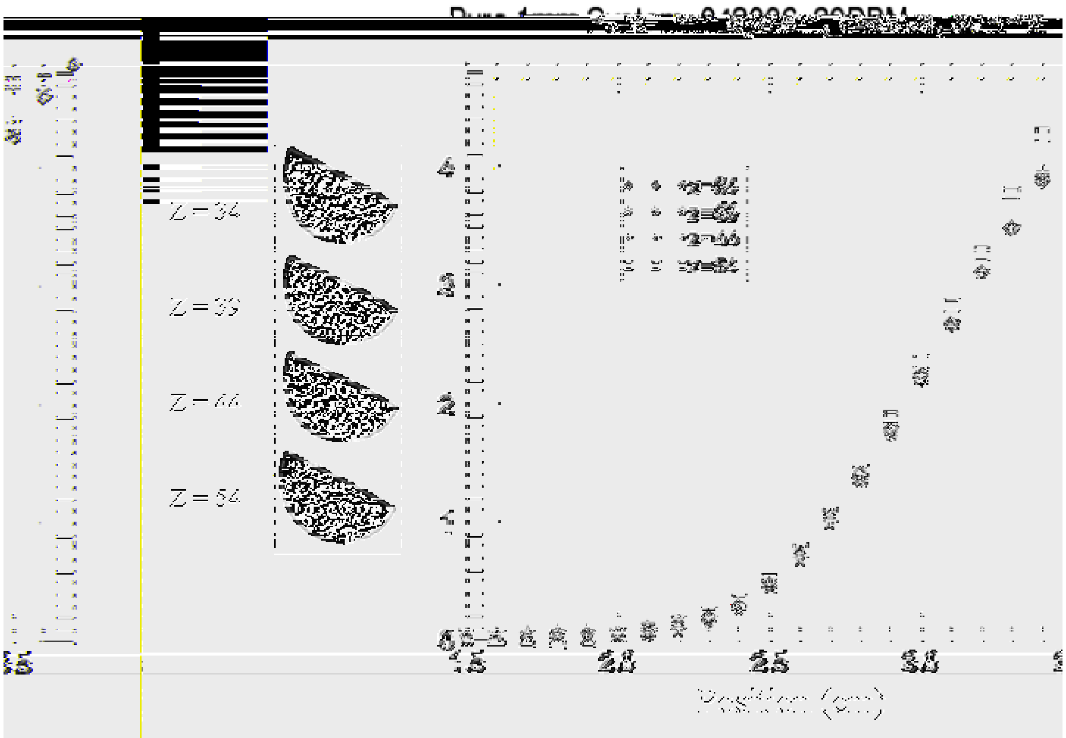

Figure 7.3: Velocity depth profiles along the axis of a pure small particle system.

axial center of the cylinder. We also took 2D data, of the 3D cylinder, with an axial slice thickness of 5mm in the manner of Maneval et al. (they used a slice thickness of 1 cm). We found that these results are consistent with the 3D results, but some of the difference is washed out due to the 5mm spatial averaging in the axial direction. The radial core remained throughout the cylinder in these experiments. It could be seen in the MRI images as well as through the endcaps of the cylinder during and after rotation.

We further found that the velocity depth profile depends not only on the composition within a slice but also on the overall system composition, which affects the composition gradient at the slice of interest. Fig. 7.6 shows how slices with the same

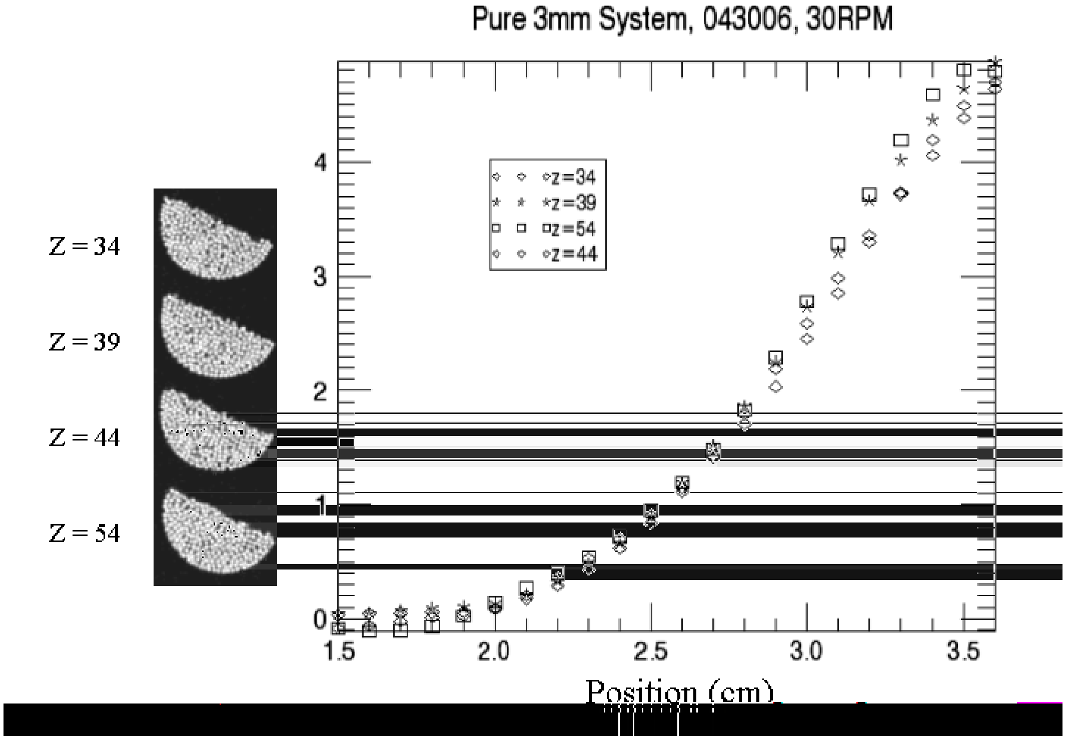

Figure 7.4: Velocity depth profiles along the axis of a pure large particle system.

or similar compositions vary between different overall mixtures. These images were taken at the center of the cylinder where there is a band of small (1mm) particles in both the 50/50 mixture and the 66/33 mixture. In the 66/33 mixture the band covers 3-4cm and is usually entirely pure at the center (occasionally a large particle is seen within this small particle band). This 3 - 4cm wide pure band of 1mm particles, therefore "sees" only other 1mm particles on each side for approximately 1.0 - 1.5cm. Yet there is a substantial difference in the velocity depth profiles at the axial center of a pure 1mm system and the center of a pure 1mm band in a 66/33 1mm/3mm system. This indicates that what is occurring in other areas of the cylinder is having an affect on the velocity depth profile, and therefore the shear, within the pure 1mm

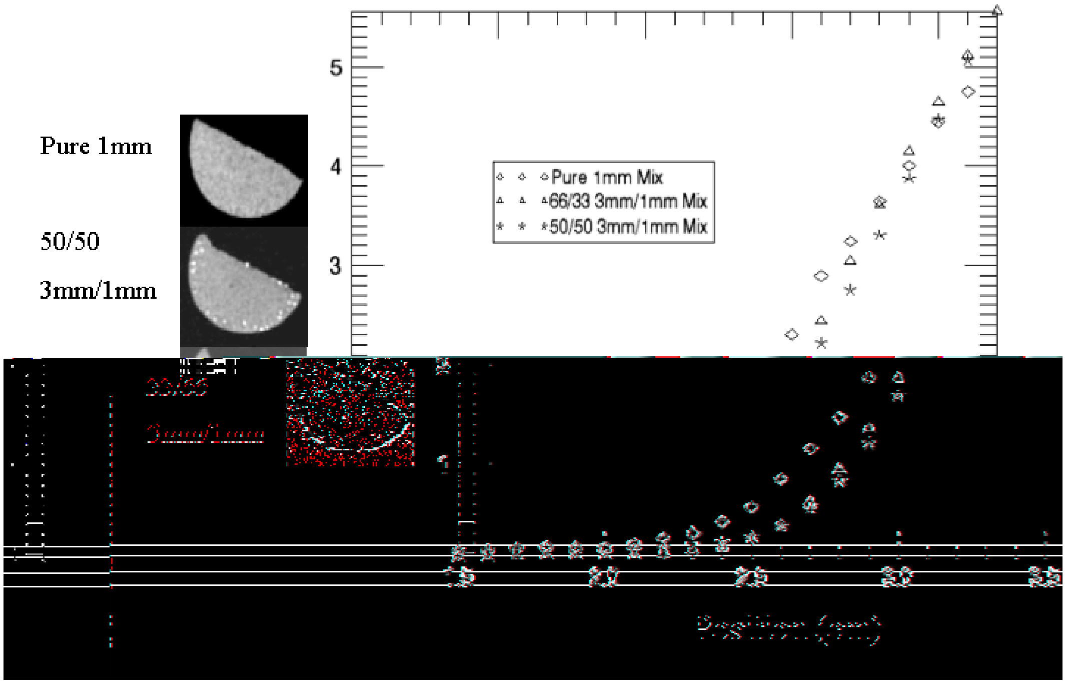

Figure 7.5: Comparison of velocity depth profiles of slices which contain all or almost all small particles. Shown is the velocity depth profile at the center of a pure small particle system, at the center of a small particle band in a 66 percent small particle mixture, and at the center of a small particle band in a 50 percent small particle mixture.

band.

Looking more closely at the differences between the velocity depth profiles along the axis, and comparing these differences to the ones seen in a non-banding system (the 2mm/4mm biparticulate mix discussed in the previous Chapter) an important difference is observed. Note, that we compare profiles between axially segregating and pure *small* particle systems, unlike the Maneval et al. [23] experiments where the comparisons were made between biparticulate systems and pure *large* particle systems. We believe that this is an important distinction, since it is reasonable to

Figure 7.6: Comparison of velocity depth profiles of slices which contain all or almost all small particles. Shown is the velocity depth profile at the center of a pure large particle system, at a location with an majority of large particles in a 66 percent small particle mixture, and at a location with an majority of large particles in a 50 percent small particle mixture.

assume that the velocity depth profile of a segregated system will follow the same profile as a pure small particle system both in a radially segregated core as well as in a band of all small particles, since only small particles are located there. There is no *a priori* reason however, for anticipating the velocity depth profile of the segregated system to follow that of a pure large particle system. For the non-banding mix the we find the velocity depth profile follows that of the pure small particle system from the bottom of the cylinder all the way to approximately the top of the radially segregated core (Fig. 6.7). Therefore we find that our assumption is validated in the case of biparticulate systems which radially but not axially segregate. However, important deviations are seen between the pure small particle profile and the areas where small particles are present in steady state axially segregating systems, contrary to our naive expectation. Even when an axial slice is composed of all small particles in the segregating system there is no correspondence with the velocity depth profile of the pure small particle system in the flowing layer (Fig. 7.7). It is also noted that in the axially banding system the velocity depth profiles away from the pure 1mm particle band *do* coincide in the flowing layer, until the top of the local core is reached, although they also never match the pure 1mm profile.

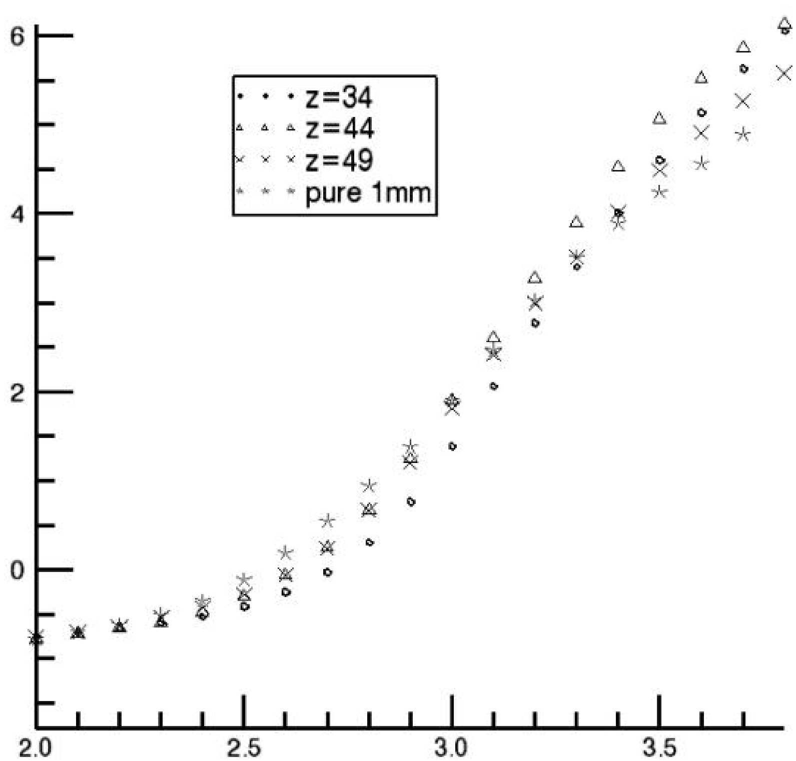

Figure 7.7: Differences in velocity depth profiles between a pure small particle system and along the axis of an axially segregating system, where at z=34 is an all small particle band, at z=44 there is approximately 70 percent small particles, and at z=49 there is approximately 50 percent small particles. Rotated at 15 rpm.

Having identified a subsurface feature that is different between segregating and non-segregating systems, it is now important to gain an understanding of how this difference could drive axial transport and sustain axial banding. First, we argue that if there is a velocity gradient along the axis of the cylinder at a particular radial position it is likely that smaller particles would be driven into the area of lower shear more easily than larger particles and accumulate there. Then the question is, why would such areas develop? We propose that directly above the small particle core (defined here as any part of the radial small particle core, whether or not it has formed undulations) larger particles are moving faster than small particles over small particles at the same radial location (Fig. 7.8). This type of behavior was observed in the "double-cone-blender" by Alexander et al [72]. We also observed this behavior when comparing a radially segregated system with a pure small particle system in Chapter 6 (see Fig. 6.6). Therefore, when there is a fluctuation in the core, the large particles moving *adjacent* to it will be moving faster than the small particles in the core fluctuation. This could then cause the smaller particles below the faster moving large particles to migrate towards the area of lower shear. However, the differences between adjacent velocity profiles must be above some threshold for the nucleation to be initiated and reinforced against the random diffusive motion that works against segregation.

We next propose that this can only happen for particle ratios which are larger than a critical value, dependent on the difference in velocities between the smaller particles sliding over a layer of other smaller particles and a layer of larger particles sliding over a layer of smaller particles. In this way the "effective" friction of the larger particles sliding over a layer of smaller particles must reach a minimum value (Fig. 7.8) for the initial fluctuation to be confined and reinforced rather than dispersed. The higher velocity of the larger particles over the smaller particles also puts greater stress on the core and some smaller particles are forced toward the original fluctuation, reinforcing the fluctuation and causing the band to grow radially. We also speculate that if there are different stresses on opposite sides of a fluctuation or band, band merging and coarsening may then occur.

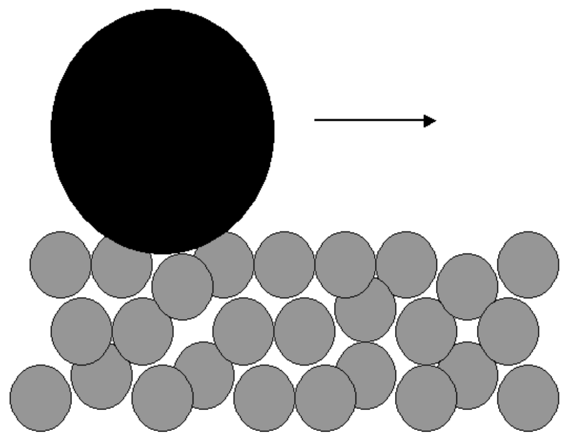

Figure 7.8: Schematic of different sized particles flowing over each other. Flow is to the right. The large particles flow over a layer of small particles faster than a layer of small particles flows over a layer of small particles.

Finally, we have observed a gradient in the velocity depth profile along the cylinder length when an axially segregating system is in a steady state, Fig. 7.7, and propose that it is the differences between adjacent velocity depth profiles *within the core region* (again defined as any part of the radial small particle core, whether or not it has formed undulations or bands), which sustain axial segregation. The observation that the profiles away from a pure band of small particles are the same from the bottom of the flowing layer until the top of the local core area is not surprising. This is the same result as was found for the radially segregating system in Chapter 6. What is perplexing is that within a band of all small particles no correspondence is observed between its velocity depth profile and any other profile along the axis, nor is there any overlap between the velocity depth profile here with that of a system of all small particles (Fig. 7.7). What is clear however is that this type of change in profile is exclusive to the axially banding system, and may only occur after a steady state is reached. Unfortunately, we do not yet have velocity depth profiles of coarsening systems to test this theory, but future experimental work should address this issue.

The theory presented above not only explains our's and Maneval et al's [50] results, but can also explain the experimental results of Alexander et al. [54] who found that both increasing the diameter of the cylinder as well as increasing the rotation rate facilitate band formation. They proposed that it is the inertia of the larger particles *radially above* an area of the core that has a fluctuation which causes the deformation to grow. However, we believe that it is important to take into account the particles *adjacent* to the fluctuation as well. Without some mechanism to confine the small particles axially it seems that they would disperse too fast to grow into a band. Furthermore, we argue that the difference in shear rate of these adjacent layers is what causes the smaller particles in the core to move towards an initial fluctuation, not a "stretching" mechanism at the top of the core.

7.2 1D Time Evolution of Bulk Granular Axial Segregation

Another way of determining what is occurring in a biparticulate granular system is to acquire 1D MRI projection images. Therefore, in these images, the intensity at an axial coordinate is summed over the transverse coordinates. The advantage of using a 1D projection technique is that behavior on over short time scales can be observed. We were able to acquire the results discussed below at a rate of 1 Hz, whereas a full 3D image of the cylinder takes minutes to obtain. The gain in speed is at the expense of information in the radial direction. The particles used were 3mm non-NMR sensitive cellulose acetate beads and 1mm NMR sensitive beads of similar density. Therefore, only the 1mm beads appear in the following MRI images.

A condensed summary of the behavior over an entire run may be conveniently presented using a "space-time" plot showing local relative concentrations of the small particle species, in which the horizontal scale measures elapsed time and the vertical scale shows the position along the cylinder axis, as shown in Fig. 7.9. Here the redder the image the higher the concentration of small particles at that axial location of the cylinder.

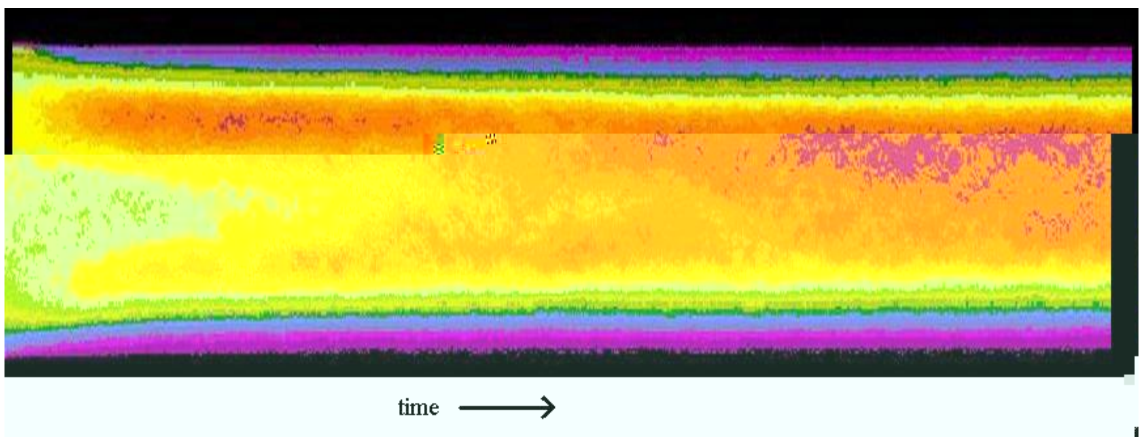

Figure 7.9: Example of 1D MRI projection images, "space-time" plot. Time runs along the horizontal axis and axial position runs along vertical axis. One pixel is the radial sum of intensities at that axial location at a time-point.

The same image is displayed as a space-time plot, a surface image of the system at the end of the run, and a plot of the concentration at different times, in Fig. 7.10. A combination of the plots and the space-time images will be used to display the results of our experimental runs.

An example of a typical run is presented in Fig. 7.11. This was for a 7cm long cylinder with a 50/50 mix of 1mm to 3mm particles which were initially well mixed. For this combination the system quickly segregates to its final one-small-band state.

Within 100 time steps (ts), which is approximately 50 sec, one band has emerged at the surface of the flow and moves very little over the remainder of the run to a position axially centered in the cylinder. This shows how the projection imaging is able to capture the details of the banding development.

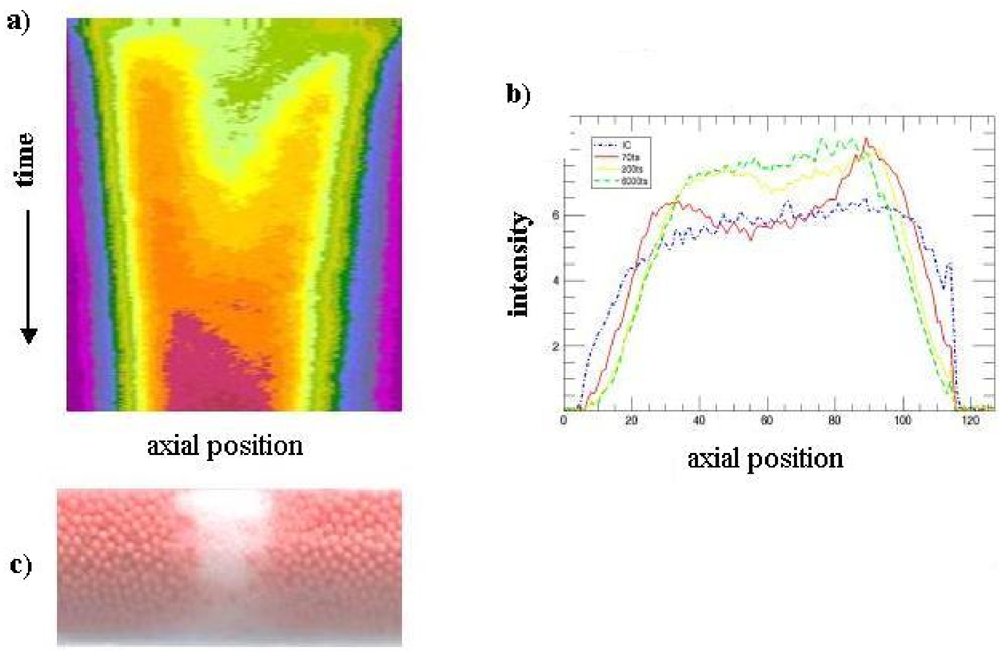

Figure 7.10: a) and b) are 1D projection images of the time evolution of a long cylinder. Images were acquired at a rate of 1 Hz and the system was a 50/50 1mm/3mm particle mix rotated at 10 rpm for 2 hrs. c) is a surface picture of the system after 2 hrs of rotation.

Since we have the 1D MRI projection imaging as a tool, which is able to image more quickly than the formation of the axial bands, we can investigate how varying system properties influences the development of the banding segregation. We chose to investigate the effect of large to small particle ratio, initial conditions, and cylinder length. The cylinder length over which 1D images were obtained was restricted by the MRI magnet to less than 10cm. Therefore, the cylinder lengths used were 2cm, 3cm, 5cm, 7cm, and 10cm long. All cylinders were rotated at 15 rpm for 30 mins.

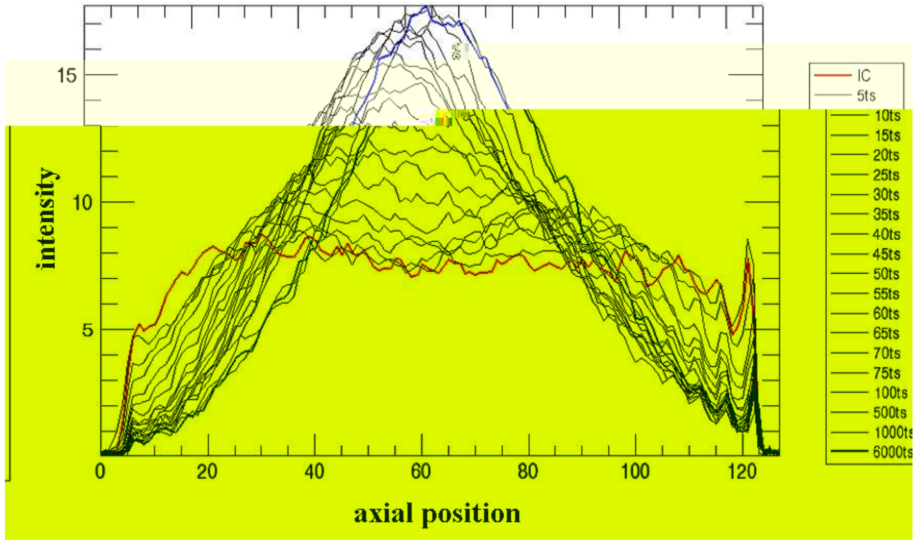

Figure 7.11: Typical 1D time evolution of 50/50 mix of 1mm/3mm particles in 7 cm long cylinder.

The mixtures were 50/50 by volume of 1mm NMR sensitive beads and 3mm non-NMR sensitive beads. Fig. 7.12 shows the results of varying the cylinder length on the development of axial banding segregation. We find that, as with surface observations, the number of bands increases with cylinder length. However, at these cylinder lengths, when two bands are formed they merge before reaching the surface, and only one band is ever observed at the surface. This is consistent with the MRI results of Hill et al. [40]. Although the shortest cylinder did not acquire an observable surface band, it is clear from the MRI images that there is an excess of small particles in the center of the cylinder. Therefore, sub-surface axial banding is not eliminated by short cylinder length ($\sim$ 6.5 large particle diameters), although the band cannot be seen from the surface. This again reinforces the importance of being able to determine subsurface structure in granular flows.

We next investigated the influence of large to small particle ratio and initial conditions on the resulting band formation. We used 3 different initial conditions,

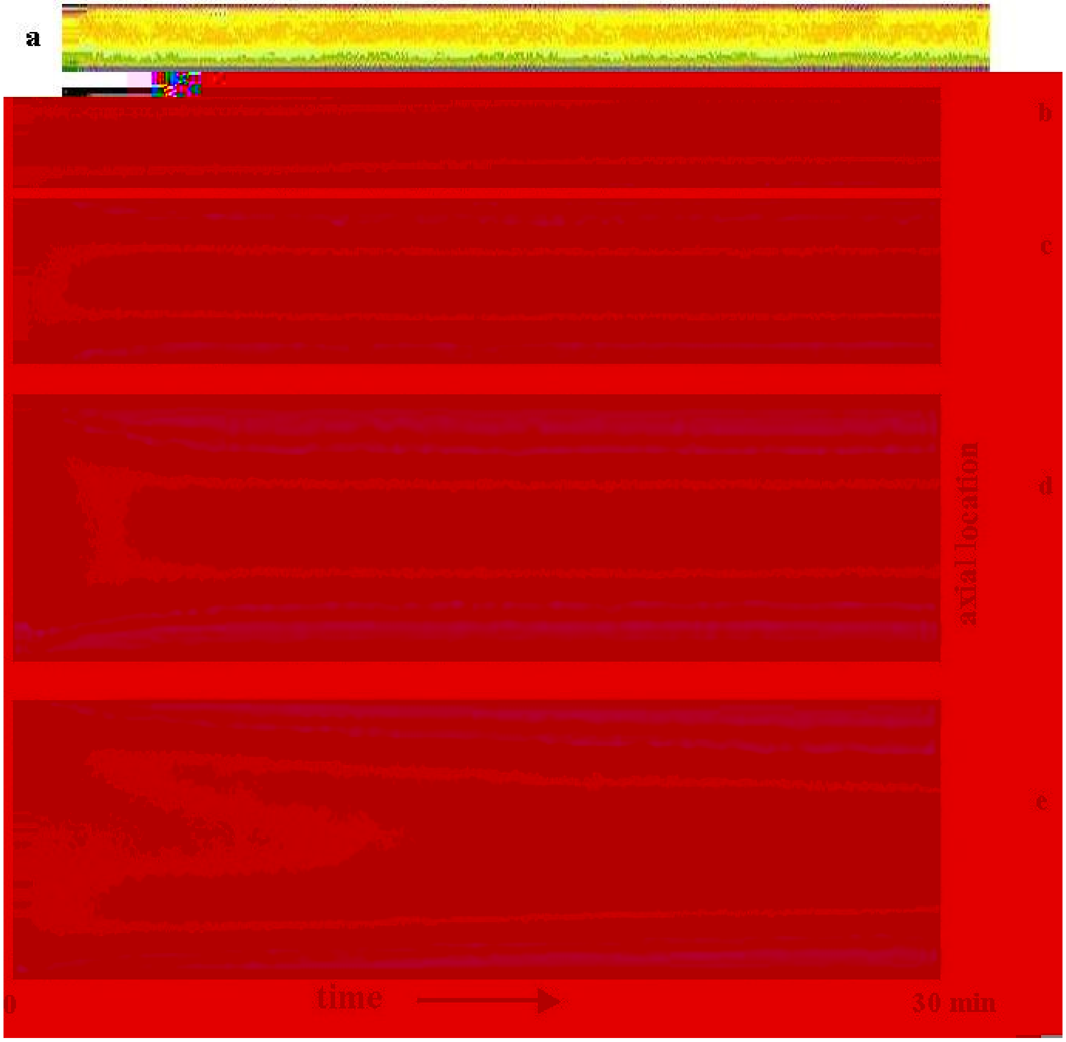

Figure 7.12: 1D time evolution of cylinders of different lengths. For a) 2cm, b) 3cm, c) 5cm, d) 7cm, e) 10cm long cylinders.

mixed, a pre-segregated central band of small particles, and a presegregated band of small particles placed against one endcap, and 3 different particle ratios, 2:1, 1:1, and 1:2 of small to large particles within the mixture, for a total of 9 experimental runs, see Fig. 7.13. It is clear from these images that initial conditions play a role in the final configuration when there is a large amount of smaller particles. The smaller particles are inhibited from moving away from the endwall.

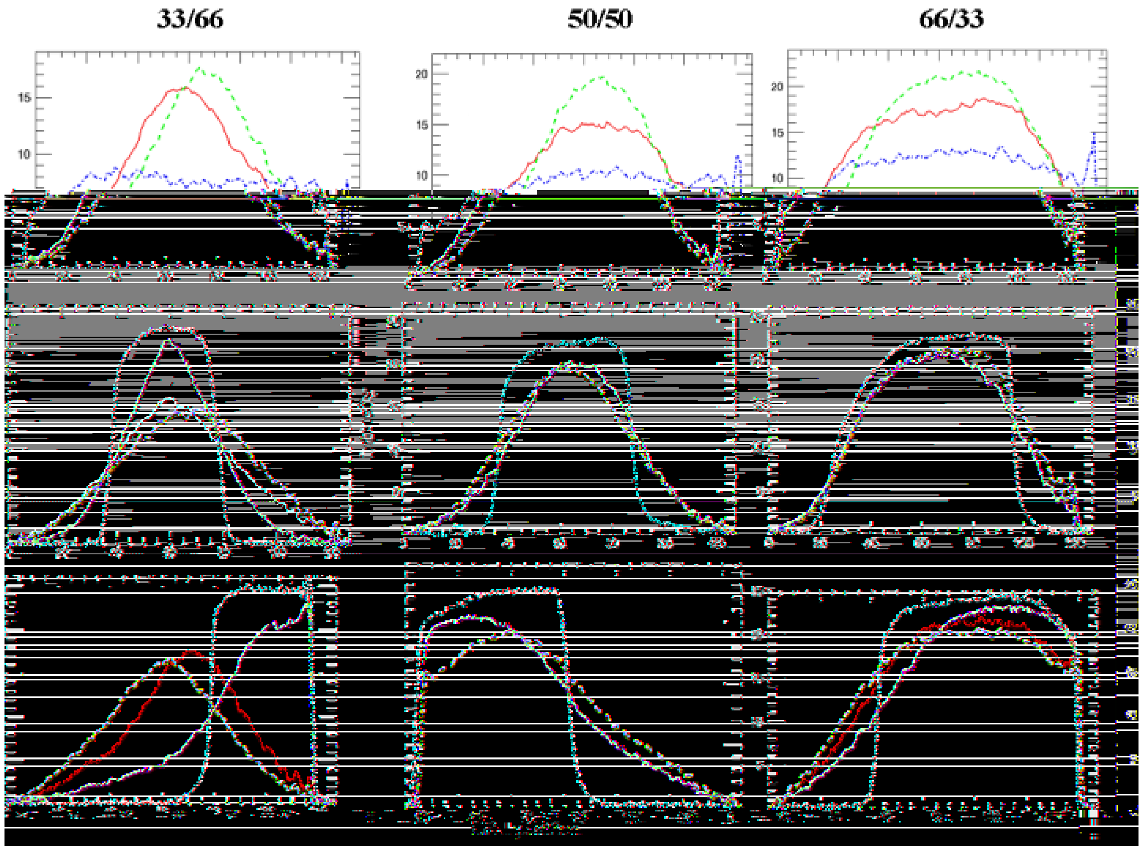

Figure 7.13: Effects of initial conditions and small/large particle ratio on band development ad evolution. All experiments were run at 15 rpm. Blue dotted plot is the initial condition of each run, red solid line is the system after 70 time steps, and the dashed green plot is the system at its final steady state configuration at 6000 time steps. Where a plot has a solid yellow line this is the system after 1500 time steps.

Furthermore, comparing the final configurations of the systems in Fig. 7.14 we find that when the small particles are not inhibited from moving freely, due to a combination of initial placement and mixture percentage, the concentration of small particles form a Gaussian distribution along the cylinder axis. This becomes less well approximated when there is a large amount of small particles, irrespective of the initial conditions, since the central band becomes spread out axially as more small particles are added.

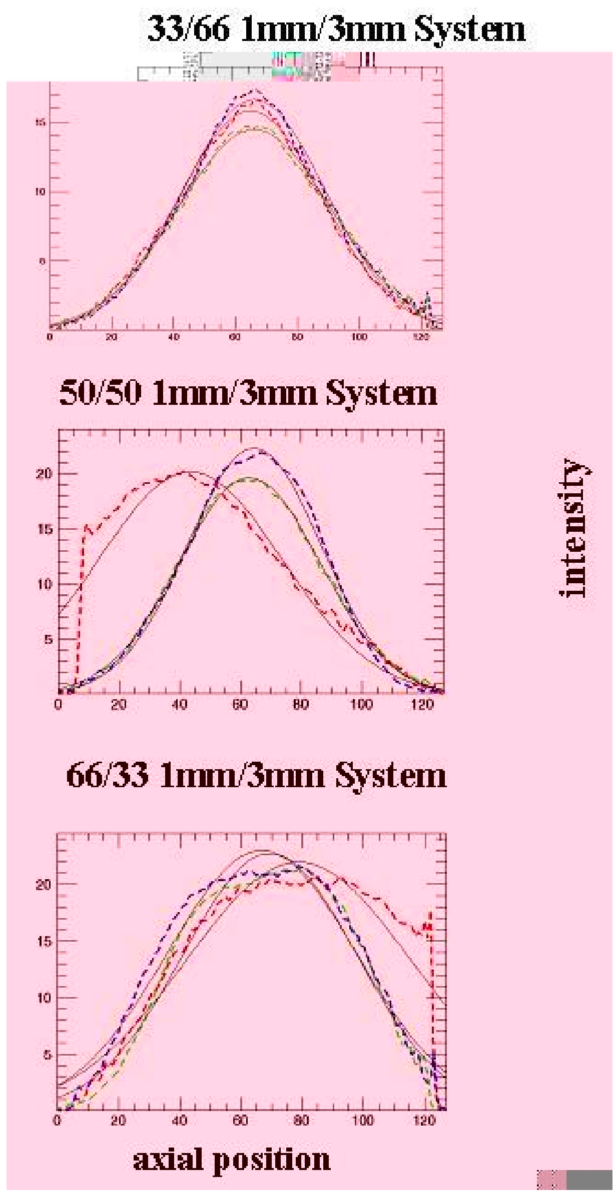

Figure 7.14: Comparison of final banding states for particles with different initial conditions and small to large particle ratio. Fits are Gaussian.

Since only 3 ratios of particles were used in the previous set of experiments we lastly wanted to determine the results for a larger range of small to large particle ratios. We therefore ran the 7cm long cylinder at 15 rpm for 30 mins for 20/80, 30/70, 40/60, 50/50, 60/40, 70/30, and 80/20 small/large particle ratios. The initial conditions were well mixed for every run. Results are shown in Figs. 7.15 and 7.16. We find that, generally, a central band of the smaller particles forms from the initially mixed conditions, with a radial core tapering from the center out to the endcaps.

With a mixture of 30 percent small particles, however, the band forms off to one side. This behavior was also seen with a mixture of 40 percent small particles rotated at 10rpm. We do not have an explanation for this anomaly. Tilting the container does not seem to have an effect of on the banding. We tested a 50/50 mixture of small to large particles rotated at 15 rpm and found that a central band consistently forms even with a large tilt angle (greater than 5 degrees). Therefore it is doubtful that a simple misalignment of the cylinder during those particular runs is responsible for the observed behavior. It has been previously observed that the initial banding configuration as seen from the surface can vary significantly from run to run, but that the systems tend to slowly converge to a steady state []. It is possible that we did not run the system long enough for it to achieve a final steady-state condition, although no discernable movement of the band was seen between approximately 5 min and 30 min of rotation. A larger number of systems should be run to quantify this behavior.

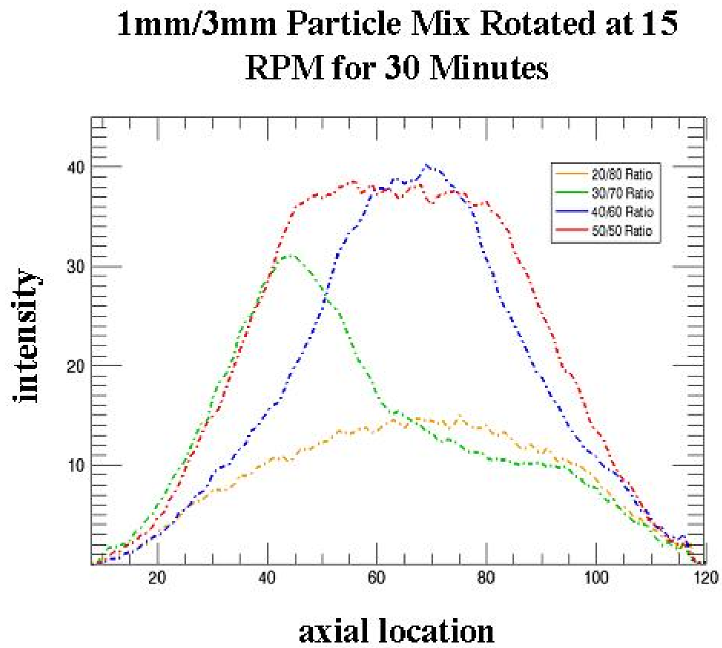

Figure 7.15: Comparison of banding with varying amounts of small/large particle ratios.

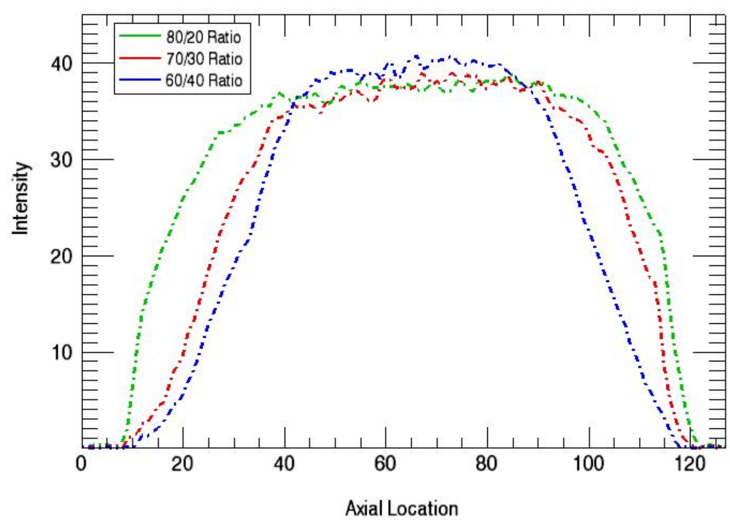

Figure 7.16: Comparison of banding with varying amounts of small/large particle ratios.

Chapter 8

Summary and Conclusions

An overall conclusion that can be drawn from the work presented throughout this dissertation is that subsurface phenomena cannot be ignored in the discussion of granular flows. Perhaps this is obvious. Yet, there has been little experimental work previously undertaken to observe subsurface bulk behavior of granular materials, in particular in the rotating drum geometry. Having such results available, both static and dynamic, is necessary for the formulation of comprehensive granular flow and segregation theories. Observations within 2D or from an endwall in 3D have been shown to be fundamentally different from that of flow away from the endwalls of a 3D flow [23]. And surface observations of axial segregation do not capture the rich subsurface evolution of the banding pattern prior to emerging at the free surface [40].

8.1 Velocity Depth Profile

One important feature of granular flow that we investigated is the form of the velocity depth profile along the central perpendicular bisector to the free surface. We present new evidence that the quadratic fit first proposed by Nakagawa et al. [35], and derived from an energy dissipation minimization criterion, is a fundamental characteristic of monoparticulate granular flows in the lens-shaped flowing region of the rotating drum. This relationship has important implications for granular flow theories. Most have assumed a linear velocity depth profile within the flowing layer, which is incompatible not only with these experimental results but also with any local and one-to-one stress/strain constitutive relations.

8.2 CA Simulation

We developed a simple 3D phenomenological cellular automaton (CA) simulation so as to be able to easily change the parameters of a flowing biparticulate granular system. The time-evolution was based on Yanagita's CA [14], with the difference that ours was developed for two different particle sizes whereas Yanagita used particles of the same size with two different particle frictions. We find that our simulation is able to reproduce some aspects of the radial and axial segregation phenomena, and the later band coarsening observed in experiments. When the larger particles are also given the larger frictional coefficient the system becomes well mixed, a result also experimentally observed [57, 58]. Allowing particles of the same size but different frictional properties to transfer between layers of the flow appears to facilitate segregation and band coarsening, at least at low numbers of transferred particles. This can be seen as a way of modeling a higher rotation rate, where particles are more mobile. Other than the instance of allowing particles to be exchanged between layers, this simulation takes into account only surface effects.

However, the simulation results exhibit an important difference from experiment. The radial core in the simulation always extends to the free surface. Experimentally, when radial segregation occurs the core is always *below* the free surface and not observable in surface observations, with at least a few layers of large particles above it. It is not until axial banding develops that small particles can be seen at the surface. This raises the question, are we really simulating a surface effect, or are these simulations representative of subsurface flow? Future work will address this question by attempting to adapt the simulation in such a way as to more accurately reflect experimental results.

8.3 Behavior of the Radially Segregated Core

Multiparticulate systems of flowing granular materials present interesting pattern formation. The radial segregation observed in both 2D and 3D biparticulate systems, in which the particle types vary by size, is explained by the generally accepted idea of a "dynamic sieving" process [38]. The smaller particles are postulated as more likely to fall through spaces formed within the flowing layer, thereby forming a radial core of the smaller particles along the axis of the drum. Almost all radial segregation studies have used a 2D geometry. Observing radial segregation at the center of a long 3D drum we found that the core has flow characteristics similar to those of the overall flow. It has a top surface that is nearly flat which is parallel to the free surface at the dynamic angle of repose. This top does not change location with increasing rotation rate, at least not in the rolling regime with an equal volume of small and large particles. The bottom of the lens-shaped flowing region becomes deeper with increased rotation rate, and we find that it is always located within the radial core, a result which has not before been reported. This observation is important since it is only within the flowing layer that particles can move axially, thereby having implications for the behavior of axially segregating systems. Additionally, the core becomes less distinct with increased rotation rate, as the smaller particles spend more time outside of what can obviously be termed the core and larger particles spend more time within it.

The "radial fingering" pattern observed in biparticulate systems with fill rates of 55-60 percent in 2D by [81], is reproducible in 3D and occurs in axially segregating systems as well.

8.4 1D Imaging of Axial Segregation

Using 1D MRI projection imaging we find that small to large particle ratio, cylinder length and initial conditions can affect axial banding behavior in the rolling regime. Furthermore, we find that when the small particles are not inhibited from moving due to initial conditions, the steady state band generally formed a Gaussian distribution of small particles along the length of the cylinder. An important open question which will be investigated is the rate of axial diffusion of small particles within a biparticulate system. Having this method of rapidly imaging in 1D using MRI will allow accurate measurements of this diffusive process.

8.5 Velocity Depth Profiles and What They Tell Us About Radially and Axially Segregating Systems

Finally, we find that the way the velocity depth profile changes between radially segregating and pure particle systems has important implications for why axial banding segregation may occur. Larger particles above a layer of smaller particles travel faster than smaller particles over other small particles at the same depth. This implies that whenever there is a difference in particle type along the axis, at the same radial location, there is going to be a difference in the shear rate of adjacent slices. We propose that this can drive a core fluctuation to become a band if the velocity difference is large enough, as reflected by a large enough particle size ratio. It is known that particles which are close in size will not axially segregate and we have now presented evidence that the reason is the lack of a large enough difference between adjacent velocity depth profiles at the boundaries of a core fluctuation. We speculate that fluctuations can then grow, undulations merge, and surface bands coarsen, until the stress on each side of a band becomes equal. More experimental work needs to be done to see if there is a difference in velocity depth profile on opposite sides of a band which merges and if it is only when the velocity profiles become the same (indicating identical shear rates surrounding a band) that the system is in a steady state.

When an axially segregating system has banded and it is in a steady state there is no correspondence between the velocity depth profile within a band of small particles and any other velocity depth profile along the cylinder axis. Furthermore, the velocity depth profile of a pure small particle system does not coincide with any of the profiles along the axis of such an axially segregated system, including areas which contain only small particles. This is in contrast to a system which only segregates radially, within which the velocity depth profiles follow that of the pure small particle system until the top of the core region, at which location they deviate. This is one way that the axially segregating system has a fundamentally different flow profile from that of a system which solely segregates radially.

One further speculation is the possibility that temporary force chains formed within the flowing layer mediate the wavelength of the axial banding. As of this writing even stationary force chains have yet to be seen in 3D, although there are plans to carry out this experiment using MRI in the near future. It may, however, take some time before there exists the technology to see transient force chains.

8.6 Main Conclusions

Our experimental results have provided new information about both mono- and biparticulate granular systems which we believe should be useful in the formation of theoretical models of granular flow and segregation.

Our main conclusions are:

1. The velocity depth profile in the flowing layer is well fit by a quadratic polynomial derived from an energy dissipation minimization and is likely to be a fundamental property of granular flow in the rotating drum geometry.

2. Subsurface dynamics are crucial to the understanding of the axial segregation phenomenon. The differences observed between velocity depth profiles in pure systems, radially segregating systems, and axially segregating systems can be used to formulate a theory as to why axial banding occurs in biparticulate systems of differently sized particles.

Appendix A

Example MRI Pulse Sequence

Below is an example of an MRI velocity encoding pulse sequence that was regularly used for the acquisition of the velocity images contained within this dissertation. Some of the important aspects are as follows. The time duration of each part of the sequence, labeled delay. Note that when there is a table this time must be multiplied by the number of elements in the table for the actual duration of that part of the sequence. The $\pi/2$ rf pulse RF, and its envelope shape, RFenv (a sinc pulse). Gradients along the X, Y, and Z directions, along with their envelopes, Xenv, Yenv, and Zenv which represent how the gradients are ramped up, how long they are kept on for, and how they are ramped down. The first set of gradients are for slice selection, the second set for velocity encoding and the third set for readout. 'Hard' contains the π pulses for rephasing. 'Phase' contain tables which hold instructions for how to step through the phase encode direction. Other items, such as OBS_BLK and TxG, are gating mechanisms specific to the hardware.

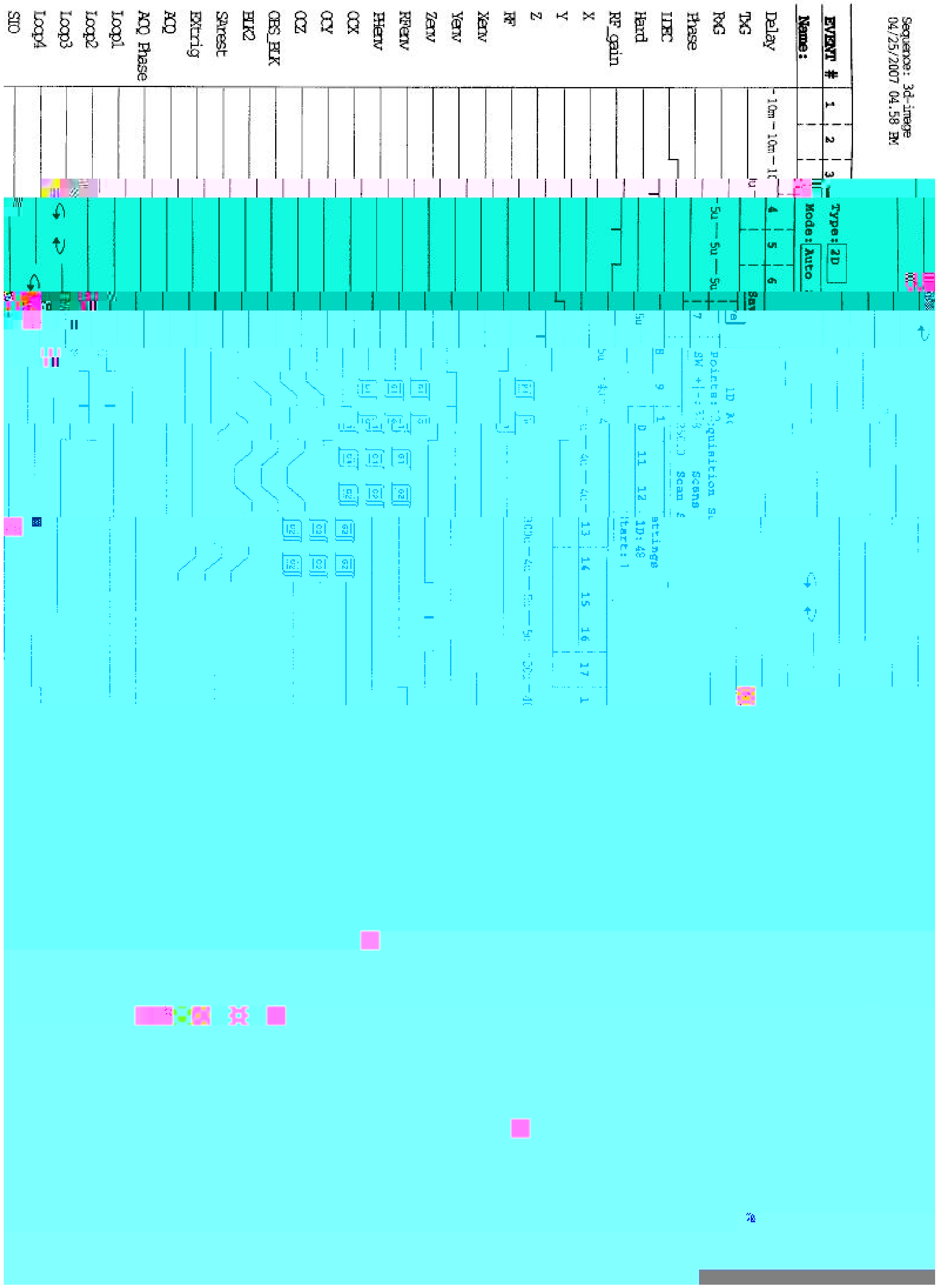
Sequence: 3d-image
04/25/2007 04:58 PM
EVENT #
Name:
Type: 2D
Mode: Auto
Delay
TXG
RXG
Phase
IDEC
Hard
RF_gain
X
Y
Z
RF
Xenv
Yenv
Zenv
RFenv
PHenv
OCX
OCY
OCZ
OBS_BLK
BLK2
EXtrig
ACQ
ACQ Phase
Loop1
Loop2
Loop3
Loop4
STO

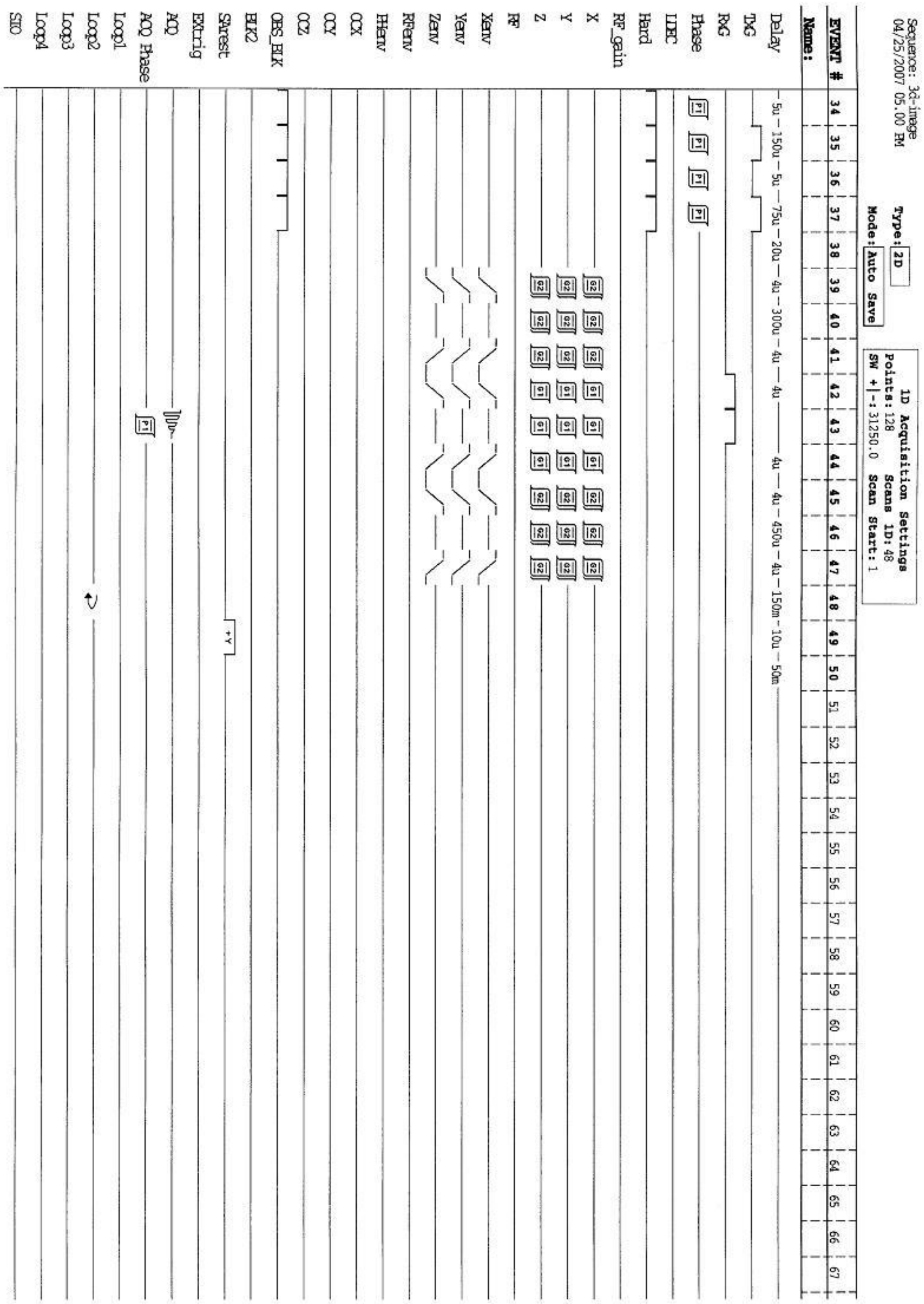
Sequence: 3d-image
04/25/2007 05.00 PM
Type: 2D
Mode: Auto Save
1D Acquisition Settings
Points: 128
Scans 1D: 48
SW +|-: 31250.0
Scan Start: 1
EVENT #
Name:
Delay
TxG
RxG
Phase
LDEC
Hard
RF_gain
X
Y
Z
RF
Xenv
Yenv
Zenv
RFenv
HHenv
CCX
CCY
CCZ
OBS_BLK
BLK2
SAreset
EXtrig
ACQ
ACQ Phase
Loop1
Loop2
Loop3
Loop4
SEO

Appendix B

Cellular Automaton Simulation Code

```
pro ca_2d_size_diff_042507

nx = 32 ny = 70 nz = 80 imx = make_array(nx,ny,nz, /float)
labeling_array = make_array(nx,ny,nz, /float) other_new =
make_array(nx,ny,nz, /float) seed = 0.5

;MAKE ARRAY OF TWO PARTICLE TYPES i = 2 for zi = 1,nz-2 do begin for
yi = 0,31,4 do begin for xi = nx/4,(nx-nx/4)-1,2 do begin
  imx[xi:xi+1,yi:yi+1,zi] = i
  i = i+1
endfor endfor endfor

for zi = 1,nz-2 do begin for yi = 2,31,4 do begin
  imx[nx/4:(nx-nx/4)-1,yi:yi+1,zi] = 1
endfor endfor
```

```
imx[nx/4-1,0:ny-10,*] = i imx[nx-nx/4,0:ny-10,*] = i
imx[nx/4-1:nx-nx/4,0:ny-10,0] = i imx[nx/4-1:nx-nx/4,0:ny-10,nz-1] =
i

time_evolution = fltarr(5005,nz) next_position =
MAKE_ARRAY(nx,ny,nz, VALUE=0, /float) height = MAKE_ARRAY(nx,nz,
VALUE=0, /float)

f_aa = .6 f_ab = .6 f_bb = .6

rotated_array=imx

for more_rots = 0,1 do begin for num_of_rotations = 0,9 do begin
newest_rot = fltarr(nx,ny,nz) rot_down = fltarr(nx,ny,nz)

;ROTATE CYLNDER shift_up_array
=shift(rotated_array[nx/4:nx/2-1,*,1:nz-2],0,1,0) new_rotated_array
= [rotated_array[0:(nx/4)-1,*,1:nz-2],$
shift_up_array,rotated_array[nx/2:nx-1,*,1:nz-2]] newest_rot[*,*,0]
= rotated_array[*,*,0] newest_rot[*,*,1:nz-2] = new_rotated_array
newest_rot[*,*,nz-1] = rotated_array[*,*,nz-1]

;see = newest_rot ;maria, imx=see

rotated_array = newest_rot

for x=nx/2,nx-nx/4-1 do begin
```

```
 for z = 1,nz-2 do begin
 if rotated_array[x,0,z] ne 0 then begin
   rotated_array[(nx-x-1),0,z] = rotated_array[x,0,z]
   rotated_array[x,0,z] =0
endif endfor endfor

shift_down_array=shift(rotated_array[nx/2:nx-(nx/4)-1,*,1:nz-2]
,0,-1,0) new_rotated_array =[rotated_array[0:nx/2-1,*,1:nz-2],$
shift_down_array, rotated_array[nx-(nx/4):nx-1,*,1:nz-2]]
rot_down[*,*,0] = rotated_array[*,*,0] rot_down[*,*,1:nz-2] =
new_rotated_array rot_down[*,*,nz-1] = rotated_array[*,*,nz-1]

rotated_array = rot_down

;FIND BEGIN HEIGHTS for x = nx/4,nx-(nx/4)-1 do begin for z = 1,nz-2
do begin for y = 0,ny-2 do begin if rotated_array[x,y+1,z] eq 0 AND
rotated_array[x,y,z] ne 0 then begin height[x,z] = y endif endfor
endfor endfor

;MOVE num PARTICLES

for r1 = 0,0 do begin for r = 0,20000 do begin

;CHOOSE RANDOM PARTICLE FROM SURFACE
  rand_x = fix((nx/2-1)*randomu(seed,1)+((nx/4)))
  rand_z = fix((nz-2)*randomu(seed,1)+1)

  ;FIND TOTAL FRICTION
```

```
  total_friction = 0

;for particle rand_z-1
   if  rotated_array[rand_x,height[rand_x,rand_z],rand_z] eq 1 $
   AND rotated_array[rand_x,height[rand_x,rand_z], rand_z-1] eq 1
   then begin
    total_friction = total_friction+f_aa
   endif
   if  rotated_array[rand_x,height[rand_x,rand_z],rand_z] ge 2 $
   AND rotated_array[rand_x,height[rand_x,rand_z], rand_z-1] ge 2
   then begin
    total_friction = total_friction+f_bb
   endif
   if  rotated_array[rand_x,height[rand_x,rand_z],rand_z] ge 2 $
   AND rotated_array[rand_x,height[rand_x,rand_z], rand_z-1] eq 1
   then begin
    total_friction = total_friction+f_ab
   endif
   if  rotated_array[rand_x,height[rand_x,rand_z],rand_z] eq 1 $
   AND rotated_array[rand_x,height[rand_x,rand_z], rand_z-1] ge 2
   then begin
    total_friction = total_friction+f_ab
   endif

  ;for particle rand_z+1
   if  rotated_array[rand_x,height[rand_x,rand_z],rand_z] eq 1 $
   AND rotated_array[rand_x,height[rand_x,rand_z], rand_z+1] eq 1
   then begin
```

```
    total_friction = total_friction+f_aa
   endif
   if  rotated_array[rand_x,height[rand_x,rand_z],rand_z] ge 2 $
   AND rotated_array[rand_x,height[rand_x,rand_z], rand_z+1] ge 2
   then begin
    total_friction = total_friction+f_bb
   endif
   if  rotated_array[rand_x,height[rand_x,rand_z],rand_z] ge 2 $
   AND rotated_array[rand_x,height[rand_x,rand_z], rand_z+1] eq 1
   then begin
    total_friction = total_friction+f_ab
   endif
   if  rotated_array[rand_x,height[rand_x,rand_z],rand_z] eq 1 $
   AND rotated_array[rand_x,height[rand_x,rand_z], rand_z+1] ge 2
   then begin
    total_friction = total_friction+f_ab
   endif

;for particle height-1 or height-2
   if  rotated_array[rand_x,height[rand_x,rand_z],rand_z] eq 1 $
   AND rotated_array[rand_x,height[rand_x,rand_z]-1, rand_z] eq 1
   then begin
    total_friction = total_friction+f_aa
   endif
   if  rotated_array[rand_x,height[rand_x,rand_z],rand_z] ge 2 $
   AND rotated_array[rand_x,height[rand_x,rand_z]-2, rand_z] ge 2
   then begin
    total_friction = total_friction+f_bb
```

```
   endif
   if  rotated_array[rand_x,height[rand_x,rand_z],rand_z] ge 2 $
   AND rotated_array[rand_x,height[rand_x,rand_z]-2, rand_z] eq 1
   then begin
    total_friction = total_friction+f_ab
   endif
   if  rotated_array[rand_x,height[rand_x,rand_z],rand_z] eq 1 $
   AND rotated_array[rand_x,height[rand_x,rand_z]-1, rand_z] ge 2
   then begin
    total_friction = total_friction+f_ab
   endif

;FIND NEW POSITION OF PARTICLE

  delt_z = randomu(seed,1)
  if delt_z ge 0 AND delt_z lt .33 then begin
    delt_z = -1
  endif
  if delt_z ge .33 AND delt_z lt .66 then begin
    delt_z = 0
  endif
  if delt_z ge .66  AND delt_z lt 1.0 then begin
    delt_z = 1
  endif

 delt_x = 1

;FIND IF PARTICLE MOVES TO NEW POSITION
```

```
if rotated_array[rand_x,height[rand_x,rand_z], rand_z] eq 1 then
begin delt_height = height[rand_x,rand_z] - height[rand_x+delt_x,
rand_z+delt_z] endif

if rotated_array[rand_x,height[rand_x,rand_z], rand_z] ge 2 then
begin delt_height = (height[rand_x,rand_z] - 1) -
height[rand_x+delt_x, rand_z+delt_z] endif

if delt_height gt total_friction AND rotated_array[rand_x+delt_x,
height[rand_x+delt_x,rand_z+delt_z]+1,rand_z+delt_z] ne i then begin

   if rotated_array[rand_x,height[rand_x,rand_z], rand_z] eq 1
   then begin
   rotated_array[rand_x+delt_x,height[rand_x+delt_x,rand_z+delt_z]+1,
   rand_z+delt_z]$
   =rotated_array[rand_x,height[rand_x,rand_z],rand_z]
   rotated_array[rand_x,height[rand_x,rand_z],rand_z]=0
   endif

   if rotated_array[rand_x,height[rand_x,rand_z], rand_z] ge 2
   then begin
   j=0
   IF rotated_array[rand_x,height[rand_x,rand_z], rand_z] ne
   rotated_array[rand_x+1,height[rand_x,rand_z], rand_z] then begin
   IF rotated_array[rand_x+delt_x+1,height[rand_x+delt_x,rand_z+
   delt_z]
   +1,rand_z+delt_z] eq 0 then begin
```

```
  IF rotated_array[rand_x+delt_x+1,height[rand_x+delt_x,rand_z+
  delt_z]
  +2,rand_z+delt_z] eq 0 then begin
  IF rotated_array[rand_x+delt_x,height[rand_x+delt_x,rand_z+delt_z]
  +1,rand_z+delt_z] eq 0 then begin
  IF rotated_array[rand_x+delt_x,height[rand_x+delt_x,rand_z+delt_z]
  +2,rand_z+delt_z] eq 0 then begin
  j=1
;position 1
   rotated_array[rand_x+delt_x+1,height[rand_x+delt_x,rand_z+delt_z]
   +2,rand_z+delt_z]$
   =rotated_array[rand_x,height[rand_x,rand_z],rand_z]
   rotated_array[rand_x,height[rand_x,rand_z],rand_z]=0
 ;position 2
    rotated_array[rand_x+delt_x,height[rand_x+delt_x,rand_z+delt_z]
    +2,rand_z+delt_z]$
   =rotated_array[rand_x-1,height[rand_x,rand_z],rand_z]
   rotated_array[rand_x-1,height[rand_x,rand_z],rand_z]=0
;position 3
   rotated_array[rand_x+delt_x,height[rand_x+delt_x,rand_z+delt_z]
   +1,rand_z+delt_z]$
   =rotated_array[rand_x-1,height[rand_x,rand_z]-1,rand_z]
   rotated_array[rand_x-1,height[rand_x,rand_z]-1,rand_z]=0
;position 4
    rotated_array[rand_x+delt_x+1,height[rand_x+delt_x,rand_z+
    delt_z]
    +1,rand_z+delt_z]$
   =rotated_array[rand_x,height[rand_x,rand_z]-1,rand_z]
```

```
    rotated_array[rand_x,height[rand_x,rand_z]-1,rand_z]=0

;see_new=rotated_array ;maria, imx=see_new

  ENDIF
  ENDIF
  ENDIF
  ENDIF
  ENDIF

if j eq 0  then begin delt_height2 = (height[rand_x,rand_z] - 1) -
height[rand_x+delt_x+1,
 rand_z+delt_z]
if delt_height2 gt total_friction then begin IF
rotated_array[rand_x,height[rand_x,rand_z], rand_z] ne
rotated_array[rand_x+1,height[rand_x,rand_z], rand_z] then begin
   IF rotated_array[rand_x+delt_x+1,height[rand_x+delt_x,rand_z+
   delt_z]+1,rand_z+delt_z] eq 1 then begin
   IF rotated_array[rand_x+delt_x+1,height[rand_x+delt_x,rand_z+
   delt_z]+2,rand_z+delt_z] eq 0 then begin
   IF rotated_array[rand_x+delt_x,height[rand_x+delt_x,rand_z+delt_z]
   +1,rand_z+delt_z] eq 0 then begin
   IF rotated_array[rand_x+delt_x,height[rand_x+delt_x,rand_z+delt_z]
   +2,rand_z+delt_z] eq 0 then begin
;position 1
    rotated_array[rand_x+delt_x+1,height[rand_x+delt_x,rand_z+delt_z]
    +3,rand_z+delt_z]$
    =rotated_array[rand_x,height[rand_x,rand_z],rand_z]
```

```
    rotated_array[rand_x,height[rand_x,rand_z],rand_z]=0
 ;position 2
     rotated_array[rand_x+delt_x,height[rand_x+delt_x,rand_z+delt_z]
     +3,rand_z+delt_z]$
    =rotated_array[rand_x-1,height[rand_x,rand_z],rand_z]
    rotated_array[rand_x-1,height[rand_x,rand_z],rand_z]=0
;position 3
    rotated_array[rand_x+delt_x,height[rand_x+delt_x,rand_z+delt_z]
    +2,rand_z+delt_z]$
    =rotated_array[rand_x-1,height[rand_x,rand_z]-1,rand_z]
    rotated_array[rand_x-1,height[rand_x,rand_z]-1,rand_z]=0
;position 4
     rotated_array[rand_x+delt_x+1,height[rand_x+delt_x,rand_z+
     delt_z]+2,rand_z+delt_z]$
    =rotated_array[rand_x,height[rand_x,rand_z]-1,rand_z]
    rotated_array[rand_x,height[rand_x,rand_z]-1,rand_z]=0

;see_new=rotated_array ;maria, imx=see_new

  ENDIF
  ENDIF
  ENDIF
  ENDIF
  ENDIF
endif endif
  endif

     ;LET SMALL PARTICLES FALL
```

```
    for yi = 0,ny-4 do begin
       if rotated_array[rand_x-1,yi,rand_z] eq 0 AND
       rotated_array[rand_x-1,yi+2,rand_z] eq 1 then begin
         rotated_array[rand_x-1,yi,rand_z] = 1
         rotated_array[rand_x-1,yi+2,rand_z] = 0
       endif
        if rotated_array[rand_x-1,yi,rand_z] eq 0 AND
        rotated_array[rand_x-1,yi+1,rand_z] eq 1 then begin
         rotated_array[rand_x-1,yi,rand_z] = 1
         rotated_array[rand_x-1,yi+1,rand_z] = 0
       endif
    endfor

;FIND NEW HEIGHT

for xi = rand_x[0]-3, rand_x[0]+delt_x[0]+3 do begin
for zi = rand_z[0]-1, rand_z[0]+delt_z[0]+1 do begin
if zi ge 1 AND zi le (nz-1) then begin
for y = 0,ny-2 do begin
  if rotated_array[xi,y+1,zi] eq 0 AND rotated_array[xi,y,zi]
  ne 0 then begin
  height[xi,zi] = y
  endif
endfor
endif
endfor
endfor
```

```
endif ;delt_height gt friction

endfor ;r endfor ;r1

print, "rotation number = ", (num_of_rotations+1)+(more_rots*10)

endfor; num_of_rots

time_evolution[more_rots,*] = reform(rotated_array[12,14,*]) p =
where(time_evolution[more_rots,*] ge 2) time_evolution[more_rots,p]
= 2

endfor ;more_rots

see_new=rotated_array maria, imx=see_new

see_time = time_evolution maria, imx =see_time

;SAVE, rotated_array, FILENAME='imagefile.sav'

p = where(rotated_array ge 2) rotated_array[p]  = 2
see_new=rotated_array maria, imx=see_new

end
```

References

[1] J. Kakalios. Granular physics or nonlinear dynamics in a sandbox. *Resource Letter GP-1, American Journal of Physics*, 73:8, 2005.

[2] S. P. Hoogendoorn, S. Luding, P. H. L. Bovy, M. Schreckenberg, and D. E. Wolf, editors. *Traffic and Granular Flow '03*. Springer, 2005.

[3] C. Wavrin. Going with the flow. *Inventing Tommorrow*, page www.it.umn.edu/news/inventing/2000$_S$pring/flow.html, 2000.

[4] H.M. Jaeger, T. Shinbrot, and P.B. Umbanhowar. Does the granular matter? *PNAS*, 97(24):12959, 2000.

[5] A. Rosato, K.J. Strandburg, F. Prinz, and R.H. Swendsen. Why the brazil nuts are on top: Size segregation of particulate matter by shaking. *Phys. Rev. Lett.*, 58:1038, 1987.

[6] GDR-MiDi. On dense granular flows. *Eur. Phys. J. E*, 14:341, 2004.

[7] D. V. Khakhar, J. J. McCarthy, T. Shinbrot, and J. M. Ottino. Transverse flow and mixing of granular materials in a rotating cylinder. *Physics of Fluids*, 9(1):31, 1997.

[8] P. Bak, C. Tang, and K. Wiesenfeld. Self-organized criticality: an explanation of $\frac{1}{f}$ noise. *Phys. Rev. Lett.*, 59:381, 1987.

[9] M. L. deHaro, E.G.D. Cohen, and J.M. Kincaid. The enskog theory for multicomponent mixtures. i. linear transport theory. *J. Chem. Phys.*, 78:2746, 1983.

[10] J.T. Jenkins and F. Mancini. Kinetic theory for binary mixtures of smooth, nearly elastic spheres. *Phys. Fluids A*, 1:2050, 1989.

[11] S.S. Hsiau and M.L. Hunt. Granular thermal diffusion in flows of binary-sized mixtures. *Acta Mech.*, 114:121, 1996.

[12] I.S. Aranson and L.S. Tsimring. Dynamics of axial separation in long rotating drums. *Phys. Rev. Lett.*, 82(23):4643, 1999.

[13] J.M. Ottino and D. V. Khakhar. Mixing and segregation of granular materials. *Annu. Rev. Fluid Mech.*, 55, 2000.

[14] T. Yanagita. Three-dimensional cellular automaton model of segregation of granular materials in a rotating cylinder. *Phys. Rev. Lett.*, 82(17):3488, 1999.

[15] M. Newey, J. Ozik, S. M. van der Meer, E. Ott, and W. Losert. Band-in-band segregation of multidisperse granular mixtures. *Europhys. Lett.*, 66(2):205, 2004.

[16] H. Henein, J.K. Brimacombe, and A.P. Watkinson. Experimental study of transverse bed motion in rotary kilns. *Metall. Trans. B*, 14B:191, 1983.

[17] A. Caprihan and E. Fukushima. Flow measurements by nmr. *Physics Reports*, 198:195, 1990.

[18] E. Fukushima. Nuclear magnetic resonance as a tool to study flow. *Ann. Rev. Fluid Mech.*, 31:95, 1999.

[19] A.A. Boateng and B.V. Barr. Granular flow behavior in the transverse plane of a partially filled rotating cylinder. *J. Fluid Mech.*, 330:233, 1997.

[20] N. Jain, J.M. Ottino, and R.M. Lueptow. An experimental study of the flowing granular layer in a rotating tumbler. *Phys. Fluids*, 14(2):572, 2002.

[21] N. Taberlet, M. Newey, P. Richard, and W. Losert. On axial segregation in a tumbler: an experimental and numerical study. *J. Stat. Mech*, page P07013, 2006.

[22] G. Félix, V. Falk, and U. D'Ortona. Granular flows in a rotating drum: the scaling law between velocity and thickness of the flow. *ArXiv Condensed Matter e-prints*, April 2006.

[23] J.E. Maneval, K.M. Hill, B.E. Smith, and A. Caprihan. Effects of end wall friction in rotating cylinder granular flow experiments. *Granular Matter*, 7(4):199, 2005.

[24] H. Ahn, C. E. Brennen, and R. H. Sabersky. Measurements of velocities, velocity fluctuations, density, and stresses for chute flows of granular materials. *Journal of Applied Mechanics*, 58(3):792, 1991.

[25] Y.L. Ding, J.P.K. Seville, R. Forster, and D.J. Parker. Solids motion in rolling mode rotating drums operated at low to medium rotation speeds. *Chem. Eng. Science*, 56:1769, 2001.

[26] A. Ingram, J.P.K. Seville, D.J. Parker, X. Fan, and G.R. Forster. Axial and radial dispersion in rolling mode rotating drums. *Powder Tech.*, 158:76, 2005.

[27] K. Yamane, M. Nakagawa, S.A. Altobelli, T. Tanaka, and Y. Tsuji. Steady particluate flows in a horizontal rotating cylinder. *Physics of Fluids*, 10(6):1419, 1998.

[28] P.G. de Gennes. Reflections on the mechanics of granular matter. *Physica A*, 261:267, 1998.

[29] D. Bonamy, F. Daviaud, and L. Laurent. Experimental study of granular surface flows via a fast camera: A continuous description. *Phys. Fluids*, 14(5):1666, 2002.

[30] A. Alexander, T. Shinbrot, and F. Muzzio. Scaling surface velocities in rotating cylinders as a function of vessel radius, rotation rate, and particle size. *Powder Technology*, 126:174, 2002.

[31] C. M. Dury, G. H. Ristow, J. L. Moss, and M. Nakagawa. Boundary effects on the angle of repose in rotating cylinders. *Phys. Rev. E*, 57(4):4491, 1998.

[32] J. Rajchenbach. Flow in powders: from discrete avalanches to continuous regime. *Phys. Rev. Letters*, 65(18):2221, 1990.

[33] S. P. Klein and B. R. White. Dynamic shear of granular material under variable gravity conditions. *AIAA Journal*, 28(10):1701, 1990.

[34] D. V. Khakhar, J. J. McCarthy, and J. M. Ottino. Radial segregation of granular materials in a rotating cylinder. *Physics of Fluids*, 9(12):1, 1997.

[35] M. Nakagawa, S.A. Altobelli, and E. Fukushima. Nmr measurement and approximate derivation of the velocity depth-profile of granular flow in a rotating, partially filled, horizontal cylinder. In R.P. Behringer and J.T. Jenkins, editors, *Powders and Grains 97*, page 447. A.A.Balkema, Rotterdam, 1997.

[36] J. Rajchenbach. Granular flows. *Advances in Physics*, 49(2):229, 2000.

[37] Y. Oyama. Studies on mixing of solids. mixing of binary system of two sizes by ball mill motion. *179th Report from Okochi Research Laboratory I.P.C.R.*, 37(951):17, 1939.

[38] S.B. Savage and C.K.K. Lun. Particle size-segregation in inclined chute flow of cohesionless granular solids. *J. Fluid Mech.*, 189:311, 1988.

[39] O. Zik, D. Levine, S.G. Lipson, S. Shtrikman, and J. Stavans. Rotationally induced segregation of granular materials. *Phys. Rev. Lett.*, 73:644, 1994.

[40] K.M. Hill, A. Caprihan, and J. Kakalios. Bulk segregation in rotated granular material measured by magnetic resonance imaging. *Phys. Rev. Lett.*, 78(1):50, 1997.

[41] N.A. Pohlman, B.L. Severson, J.M. Ottino, and R.M. Lueptow. Suface roughness effects in granular matter: influence on angle of repose and the absence of segregation. *Phys. Rev. E*, 73:031304, 2006.

[42] K. Choo, T.C.A. Molteno, and S.W. Morris. Traveling granular segregation patterns in a long drum mixer. *Phys. Rev. Lett.*, 79(16):2975, 1997.

[43] I.S. Aranson, L.S. Tsimring, and V.M. Vinokur. Continuum theory of axial segregation in a long rotating drum. *Phys. Rev. E*, 60(2):1975, 1999.

[44] Z.S. Khan, W.A. Tokaruk, and S.W. Morris. Oscillatory granular segregation in a long drum mixer. *Europhys. Letters*, 66(2):212, 2004.

[45] Z.S. Khan and S.W. Morris. Subdiffusive axial transport of granular materials in a long drum mixer. *Phys. Rev. Lett.*, 94:048002, 2004.

[46] N. Taberlet and P. Richard. Diffusion of a granular pulse in a rotating drum. *Phys. Rev. E*, 73:041301, 2006.

[47] E.M. Haacke, R.W. Bown, M.R. Thompson, and R. Venkatesan. *Magnetic resonance imaging: Physical principals and sequence design.* Wiley, New York, 1999.

[48] B. Blumich. *NMR imaging of materials.* Oxford Science Publications, 2000.

[49] E. Fukushima. Granular flow studies by nmr: A chronology. *Adv. Complex Systems*, 4:1, 2001.

[50] J.E. Maneval, B.E. Smith, A. Caprihan, and E. Fukushima. Flow measurement in rotational flow of mixed-size granular systems. In R. Garca-Rojo, H.J. Herrmann, and S. McNamara, editors, *Powders and Grains 2005*, page 841. A.A.Balkema, Rotterdam, 2005.

[51] D.V. Khakhar, A.V. Orpe, and J.M. Ottino. Surface granular flows: two related examples. *Adv. Complex Systems*, 4(4):407, 2001.

[52] M. Renouf, D. Bonamy, F. Dubois, and P. Alart. Numerical simulation of two-dimensional steady granular flows in a rotating drum: On surface flow rheology. *Phys. Fluids*, 17:103303, 2005.

[53] C. Heine, S. Han, S. Stapf, B. Bluemich, S. A. Altobelli, A. Caprihan, E. Fukushima, M. Hufschmidt, J. Koke, M. Modigell, and J. Petera. Nmr measurements of dynamic phenomena in cylindrical geometries: Experiments on narrow gap couette flow and granular flow. In *30th Congress AMPERE on Magnetic Resonance and Related Phenomena.* Lisbon, Portugal, 2000.

[54] A. Alexander, F.J. Muzzio, and T. Shinbrot. Effects of scale and inertia on granular banding segregation. *Granular Matter*, 5:171, 2004.

[55] P.W. Cleary, G. Metcalf, and K. Liffman. How well do discree element granular flow models capture the essentials of mixing processes? *Appl. Math. Modeling*, 22:995, 1998.

[56] J.M. Ottino and D.V. Khakhar. Fundamental research in heaping, mixing, and segregation of granular materials: challenges and perspectives. *Powder Tech.*, 121:117, 2001.

[57] G. Metcalfe and M. Shattuck. Pattern formation during mixing and segregation of flowing granular materials. *Physica A*, 233:709, 1996.

[58] N. Jain, J.M. Ottino, and R.M. Lueptow. Regimes of segregation and mixing in combined size and density granular systems: an experimental study. *Granular Matter*, 7:69, 2005.

[59] R. Chicharro, R. Peralta-Fabi, and R.M. Velasco. Segregation in dry granular systems. In R.P. Behringer and J.T. Jenkins, editors, *Powders and Grains 97*, page 479. A.A.Balkema, Rotterdam, 1997.

[60] D. Bideau F. Cantelaube. Radial segregation in a 2d drum: an experimental analysis. *Europhys. Lett.*, 30:133, 1995.

[61] D.V. Khakhar, J.J. McCarthy, and J.M. Ottino. Mixing and segregation of granular materials in chute flows. *Chaos*, 9(3):594, 1999.

[62] R.B. Bird, W.E. Stewart, and E.N. Lightfoot. *Transport phenomena*. John Wiley and Sons, New York, 1960.

[63] N. Nityanand, B. Manley, and H. Henein. An analysis of radial segregation for different sized spherical solids in rotary cylinders. *Metall. Trans. B*, 17B:247, 1986.

[64] J.P. Bouchard, M.E Cates, R. Prakash, and S.F. Edwards. A model for the dynamics of sandpile surfaces. *J. Phys. I France*, 4:1383, 1994.

[65] T. Boutreux and P.G. de Gennes. Surface flows of granular mixtures: I. general principles and minimal model. *J. Phys. I France*, 6:1295, 1996.

[66] H.A. Makse. Stratification instability in granular flows. *Phys. Rev. E*, 56:7008, 1997.

[67] T. Boutreux, H. Makse, and P.G. de Gennes. Surface flows of granular mixtures: Iii. canonical model. *Eur. Phys. J. B*, 9:105, 1999.

[68] S. Chakraborty, P.R. Nott, and J.R. Prakash. Analysis of radial segregation of granular mixtures in a rotating drum. *Eur. Phys. J. E*, 1:265, 2000.

[69] T.S. Komatsu, S. Inagaki, N. Nakagawa, and S. Nasuno. Creep motion in a granular pile exhibiting steady surface flow. *Condensed Matter*, 2000.

[70] J.W. Cahn and J.E. Hilliard. Free energy of a nonuniform system i. interfacial free energy. *J. Chem. Phys.*, 28:258, 1958.

[71] S. Puri and H. Hayakawa. Radial and axial segregation of granular mixtures in the rotating-drum geometry. *Advances in Complex Systems*, 4(4):469, 2001.

[72] A. Alexander, T. Shinbrot, and F. Muzzio. Granular segregation in the double-cone blender: Transitions and mechanisms. *Phys. Fluids A*, 13(3):578, 2001.

[73] T. Elperin and A. Vikhansky. Granular flow in a rotating cylindrical drum. *Europhys. Letters*, 42(6):619, 1998.

[74] M. Nakagawa, S.A. Altobelli, A. Caprihan, E. Fukushima, and E.-K. Jeong. Non-invasive measurements of granular flows by magnetic resonance imaging. *Experiments in Fluids*, 16:54, 1993.

[75] E. Clement, J. Rajchenbach, and J. Duran. Mixing of a granular material in a bidimensional rotating drum. *Europhys. Lett.*, 30:7, 1995.

[76] K. M. Hill, G. Gioia, D. Amaravadi, and C. Winter. Moon patterns, sun patterns, and wave breaking in rotating granular mixtures. *Complexity*, 10(4):79, 2005.

[77] L. Sanfratello, A. Caprihan, and E. Fukushima. Velocity depth profile of granular matter in a horizontal rotating drum. *Granular Matter*.

[78] D. C. Rapaport. Simulational studies of axial granular segregation in a rotating cylinder. *Phys. Rev. E*, 65:061306, 2002.

[79] K.M. Hill, J. Kakalios, K. Yamane, Y. Tsuji, and A. Caprihan. Dynamic angle of repose as a function of mixture concentration: results from mri experiments and dem simulations. In R.P. Behringer and J.T. Jenkins, editors, *Powders and Grains 97*, page 463. A.A.Balkema, Rotterdam, 1997.

[80] K. M. Hill and J. Kakalios. Reversible axial segregation of rotating granular media. *Phys. Rev. E*, 52:4393, 1995.

[81] K.M. Hill, G. Gioia, and D. Amaravadi. Radial segregation patterns in rotating granular mixtures: waviness selection. *Phys. Rev. Lett.*, 93:224301, 2004.